A Search for Electron and Neutrino Compositeness in ep Collisions at HERA

by

Ali Sabetfakhri

A thesis submitted in conformity with the requirements

for the degree of Doctor of Philosophy

Graduate Department of Physics

University of Toronto

© Copyright by Ali Sabetfakhri 2000

Abstract

The observation of excited states of the fundamental fermions would be a clear signal that these particles are composite rather than elementary. Heavy excited states of electrons have been searched for in e^+p collisions at a center-of-mass energy of 300 GeV with the ZEUS detector at HERA using a data set corresponding to an integrated luminosity of 38.4 pb^{-1}. A signal for an excited electron was sought via the decay modes $e^* \to e\gamma$, $e^* \to eZ$ and $e^* \to \nu W$. A search for excited neutrinos decaying via $\nu^* \to \nu\gamma$ using the recent e^-p collision data at 318 GeV center-of-mass energy corresponding to an integrated luminosity of 16.7 pb^{-1} has also been performed. No evidence was found for such states and limits on the characteristic couplings are derived.

To my Parents

> ... it is important to gain knowledge. Grasp of the intelligibles determines the fate of the rational soul in the hereafter, and therefore is crucial to human activity.
>
> **Avicenna**

Acknowledgement

I would like to thank Professor David C. Bailey and Professor John F. Martin for their encouragement, support and supervision during my study. Their suggestions and supervision during my work in ZEUS experiment had an important role in my success. Thanks to Professor Sampa Bhadra for her encouragement, help, and suggestions.

Very special thanks to Dr. Masahiro Kuze as leader of the ZEUS Exotic and Rare Phenomena Group, for his encouragement, suggestions, and specially supervision of my analysis. Without his warm support and help I could not achieve my goal. I also would like to thank other members of the Exotic and Rare Phenomena Group, especially its coordinators for their help and suggestions. I am very grateful to Dr. Stefano Dusini, and Mr. Ainas Weber, members of the excited fermion group, for checking the final results by performing a second analysis.

Many thanks go to my colleagues at DESY especially the Canadian groups in the ZEUS experiment with whom I spent three years of my life and learned a lot. I am very grateful to Dr. Stefan Schlenstedt the ZEUS physics chairman.

Also thanks go to Professors Mike Luke and Bob Holdom from whom I learned very much. Thanks to Mrs. Marianne Khurana for her advice.

Thanks to my parents who opened the gates of knowledge and wisdom to me. Special thanks to Tannaz Sabetfakhri, my sister, for her warm support and guidance.

Many thanks to my brother, Dr. Kazem Sabetfakhri, for his warm support and guidance and to my family, scattered around the world.

Finally, I thank all my friends especially Mrs. Raija Gronmeyer.

Personal Contributions to the ZEUS Experiment

During my last three and half years of study, I have been working in ZEUS experiment at DESY, Hamburg, Germany. I participated in the Forward Neutron Calorimeter (FNC) group and helped conducting ^{60}Co source scan of the FNC and calibration of the 1996+97 data. I joined the Calorimeter group and was given the responsibility for the maintenance of the Forward and Rear part of the main Uranium-Scintillator calorimeter. In addition, during my 1996-2000 running period, as a calorimeter expert, I participated in Calorimeter Data Quality Monitor shifts in which I monitored the data quality of the calorimeter.

I also worked on testing the NIM (Nuclear Instrument Modules) electronic and install a spare of the whole readout system in the ZEUS Hall.

During the yearly running periods, I did the safety and deputy shifts, where the safety officers were responsible for the safe operation of the ZEUS experiment and the deputies were dealing with data quality monitoring.

I was a member of the ZEUS Exotic Physics Group, working on excited electrons and neutrinos and looking for their signatures, if they exist. I searched for excited electrons and neutrinos via their decays into a standard model fermion and a gauge boson. My analysis is built upon the 1996-97 e^+p data and also the new 1998-99 e^-p data collected by the ZEUS detector. The preliminary results of the analysis were shown in ICHEP98 conference in Vancouver ($e^* \to e\gamma$ channel), EPS99 conference in Tempere (e^* and $\nu^* \to \nu\gamma$ channel). A paper is currently under preparation with the final results from the 94-97 data where I provided the first analysis for the excited electron and excited quark.

"All these things being considered, it seems probable to me that God in the beginning formed matter in solid, massy, hard, impenetrable, movable particles of such sizes and figures, and with such other properties, and in such proportion to space, as most conduced to the end for which he formed them; and that these primitive particles being solids, are incomparably harder than any porous bodies compounded of them; even so very hard, as never to wear or break in pieces; no ordinary power being able to divide what God himself made in the first creation. While the particles continue entire, they may compose bodies of one and the same nature and texture in all ages: but should they wear away, or break in pieces, the nature of things depending on them would be changed. Water and earth, composed of old worn particles and fragments of particles, would not be of the same nature and texture now, with water and earth composed of entire particles in the beginning. And there, that nature may be lasting, the changes of corporal things are placed only in the various separations and new associations and motions of these permanent particles. "

Isaac Newton - Optics

Contents

1 Introduction **1**

2 Theoretical Aspects **5**

2.1 Phenomenological Model 5

2.2 Production Cross-section 7

2.3 Decay modes 10

3 Experimental Procedure **12**

3.1 Deep Inelastic Scattering 14

3.2 QED-Compton Scattering 17

3.3 Photoproduction 19

3.4 Single W-production 20

4 Experiment Setup **23**

4.1 HERA 23

4.2 Luminosity 23

4.3 The Zeus Experiment 26

4.3.1 The Uranium Calorimeter 26

4.3.2 Central Tracking Detector 30

4.3.3 Luminosity Monitor 31

4.4 Trigger and Data Acquisition 32

5 Monte Carlo Simulation **34**

5.1 The e^*/ν^* Event Generator 34

5.2 Background Simulation 36

5.2.1 NC/CC Simulation 36

5.2.2 QED-Compton Simulation 36
5.2.3 Photoproduction Simulation 37
5.2.4 W-production Simulation 37
5.3 Detector Simulation 39
6 Event Reconstruction 40
6.1 Track Reconstruction and Vertex finding 40
6.2 The Calorimeter Reconstruction 41
6.3 Clustering of Energy Deposits 41
6.4 Kinematic Variables 42
6.5 Electromagnetic Cluster Identification 44
6.5.1 Electron Energy Corrections 46
6.5.2 Track Matching Requirements 46
6.5.3 Electron Isolation Requirements 47
7 Data Selection 51
7.1 Online Event Selection 51
7.1.1 DST Selection 52
7.2 Offline Cuts 53
7.2.1 Corrections 54
7.2.2 Cleaning Cuts 55
8 e^* Event Samples 61
8.1 Events with Electromagnetic Cluster 61
8.2 Events without Electromagnetic Cluster 63
8.2 Summary of e^* Event Samples 66
9 e^* Mass Reconstruction 69
9.1 $e\gamma$ Invariant Mass 69
9.2 eZ Invariant Mass 70
9.3 νW Invariant Mass 72

10 Search for Excited Electrons 74
10.1 $e\gamma$ Resonance Search 74
10.1.1 Final $e\gamma$ Sample 75
10.2 $eq\bar{q}$ Resonance Search 88
10.2.1 Final $eq\bar{q}$ Sample 88
10.3 $e\nu\bar{\nu}$ Resonance Search 97
10.3.1 Final $e\nu\bar{\nu}$ Sample 98
10.4 $\nu q\bar{q}'$ Resonance Search 107
10.4.1 Final $\nu q\bar{q}'$ Sample 107
11 Search for Excited Neutrinos 115
11.1 ν^* Mass Reconstruction 117
11.2 Final $\nu\gamma$ Sample 118
12 Systematic Uncertainties 123
12.1 Experimental Uncertainties 123
12.2 Theoretical Uncertainties 128
13 Limit Setting Procedure 129
14 Results 134
14.1 Present Constraints 140
15 Conclusions 144
Appendix A Definition of DST Bits 146
Appendix B Derivation of Mass Formulae 153
B.1 Derivation of Eq. (24) 153
B.2 Derivation of Eq. (25) 154
B.3 Derivation of Eq. (26) 155
B.4 Derivation of Eq. (28) 156
References 158

List of Tables

1: Excited electron and neutrino decays and topologies, and backgrounds to e^* and ν^* production. The abbreviations EM, P_t^{miss}, E_t^{had}, and M^{had} stand for electromagnetic cluster, missing transverse energy, hadronic transverse energy, and hadronic invariant mass, and NC, CC, Compton, PHP, and W for neutral current, charged current deep inelastic scattering, QED-Compton scattering, photoproduction, and W-production, respectively. 13

2: HERA parameters at the end of 1997. 25

3: Signal Monte Carlo samples used in this analysis. 35

4: Background Monte Carlo samples used in this analysis. 38

5: MEPS set of background Monte Carlo samples used in this analysis. 39

6: The efficiency of the signal Monte Carlo due to trigger effects. 53

7: The efficiency of the signal Monte Carlo after cleaning cuts (including the trigger effects). 60

8: The summary of the e^* event samples. 67

9: The efficiency of the signal Monte Carlo after e^* event sample cuts. 66

10: (a) Efficiency for $e^* \to e\gamma$ signal Monte Carlo (fraction of accepted events). The last line in the table shows the overall acceptance. (b) The comparison between

data and background Monte Carlo expectation. The table entries are the number of accepted events after each cut. 86

11: (a) Efficiency for $e^* \to eZ \to eq\bar{q}$ signal Monte Carlo (the fraction of accepted events). The last line in the table shows the overall efficiency. (b) The comparison between data and background Monte Carlo expectation. The table entries are the number of accepted events after each cut. 95

12: (a) Efficiency for $e^* \to eZ \to e\nu\bar{\nu}$ signal Monte Carlo (the fraction of accepted events). The last line in the table shows the overall total events accepted. (b) The comparison between data and background Monte Carlo expectation. The table entries are the number of accepted events after each cut. 103

13: Efficiency for $e^* \to \nu W \to \nu\bar{\nu}e$ signal Monte Carlo (the fraction of accepted events). The last line in the table shows the overall efficiency. 104

14: (a) Efficiency for $e^* \to \nu W \to \nu q\bar{q}'$ signal Monte Carlo (fraction of accepted events). (b) The comparison between data and background Monte Carlo expectation. The table entries are the number of accepted events after each cut. The last line in the table shows the final sample. 112

15: (a) Efficiency for $\nu^* \to \nu\gamma$ signal Monte Carlo (fraction of accepted events). The last line in the table shows the overall total efficiency. (b) The comparison between data and background Monte Carlo expectation. The table entries are the number of accepted events after each cut. 120

16: The sensitivity of event selection to the energy scale of the calorimeter for e^* and ν^* decay channels. 124

17: The sensitivity of event selection to vertex position cuts for excited electron and neutrino decay channels. 126

18: The effects of varying the selection cuts on efficiency ($\Delta\epsilon$) for e^* and ν^* decay channels. 127

19: Contribution to the overall experimental uncertainties. The values in paretheses are the experimental uncertainties for e^*. 127

20: Efficiency (ϵ), number of observed events ($N_{\rm Obs}$), and number of expected background events ($N_{\rm Exp}$) for the channels studied in this analysis. 135

List of Figures

1: Diagrams for the production of excited leptons via (a) elastic and (b) inelastic processes in ep collisions. 3

2: Total e^* production cross-section versus e^* mass in ep collisions at $\sqrt{s} = 314$ GeV with $f/\Lambda = f'/\Lambda$=1 TeV^{-1}. Elastic (dash-dotted line), inelastic low-Q^2 (dotted line), and deep inelastic contributions (dashed line) are shown separately [14]. 9

3: Comparison of the predicted cross-section for excited neutrino production in e^+p collisions versus e^-p collisions for$f/\Lambda = f'/\Lambda = 1$ TeV^{-1}. 10

4: The branching ratio for $e^* \to e\gamma$, eZ, νW as a function of the mass of the excited electron. 11

5: Distribution of transverse energy of the electromagnetic cluster (E_t^{EM}) for (a) 125 GeV (solid line) and 225 GeV (dashed line) $e^* \to e\gamma$, (b) 125 GeV (solid line) and 225 GeV (dashed line) $e^* \to eZ \to eq\bar{q}$ Monte Carlo, 125 GeV (dash-dotted line) and 225 GeV (dotted line) $e^* \to eZ \to e\nu\bar{\nu}$, (c) 125 GeV (solid line) and 225 GeV (dashed line) $e^* \to \nu W \to \nu\bar{\nu}e$, 125 GeV (dotted line) and 225 GeV (dash-dotted line) $\nu^* \to \nu\gamma$ Monte Carlo, and (d) NC DIS (solid line), single W-production (dashed line). and QED-Compton Monte Carlo (dotted line). 15

6: The polar angle distribution of the electromagnetic cluster (θ_{EM}) for (a) 125 GeV (solid line) and 225 GeV (dashed line) $e^* \to e\gamma$, (b) 125 GeV (solid line) and 225 GeV (dashed line) $e^* \to eZ \to eq\bar{q}$ and 125 GeV (dotted line) and 225 GeV (dash-dotted line) $e^* \to eZ \to e\nu\bar{\nu}$, (c) 125 GeV (solid line) and 225 GeV

(dashed line) $e^* \to \nu W \to \nu\bar{\nu}e$, 125 GeV (dotted line) and 225 GeV (dash-dotted line) $\nu^* \to \nu\gamma$, and (c) NC DIS (solid line), single W-production (dashed line). and QED-Compton Monte Carlo (dotted line). 16

7: Distribution of the missing transverse momentum (P_t^{miss}) for (a) 125 GeV (solid line) and 225 GeV (dashed line) $e^* \to \nu W \to \nu q\bar{q}'$, 125 GeV (dash-dotted line) and 225 GeV (dotted line) $e^* \to eZ \to e\nu\bar{\nu}$ Monte Carlo, (b) 125 GeV (solid line) and 225 GeV (dotted line) $e^* \to \nu W \to \nu\bar{\nu}e$, 125 GeV (dashed line) and 225 GeV (dash-dotted line) $\nu^* \to \nu\gamma$, (c) CC DIS (solid line), NC DIS (dashed line), and (d) single W-production (solid line) and photoproduction (dashed line) Monte Carlo. 17

8: Distribution of $E - P_z$ for (a) 125 GeV (solid line) and 225 GeV (dash-dotted line) $e^* \to e\gamma$, 125 GeV (dashed line) and 225 GeV (dotted line) $e^* \to eZ \to e\nu\bar{\nu}$, (b) 125 GeV (solid line) and 225 GeV (dash-dotted line) $e^* \to eZ \to eq\bar{q}$, 125 GeV (dashed line) and 225 GeV (dotted line) $e^* \to \nu W \to \nu q\bar{q}'$, (c) 125 GeV (solid line) and 225 GeV (dotted line) $e^* \to \nu W \to \nu\bar{\nu}e$, single W-production (dashed line), and (d) QED-Compton (solid line), NC DIS (dashed line), CC DIS (dotted line), and photoproduction (dash-dotted line) Monte Carlo. 18

9: Schematic diagram describing deep inelastic ep scattering. The four-vectors of the particles, or particle systems, are given in parentheses. In neutral current deep inelastic scattering l is an electron (with γ/Z exchange) and in charged current process l is a neutrino (with W boson exchange). 19

10: Schematic diagram describing QED-Compton scattering. 19

11: Schematic diagrams represent the lowest order "direct photon" processes (a) QCD Compton Scattering and (b) Photon-Gluon Fusion. 20

12: Diagrams for "resolved photon" processes, where the hadronic structure of the photon is manifested. 21

13: Feynman diagrams of the main processes contributing to the W production in the reaction $ep \to eWX$. 22

14: Layout of the HERA ring. 24

15: ZEUS Luminosities. 25

16: Longitudinal and transverse projection of the ZEUS detector. 27

17: A cut-away view of a ZEUS FCAL module, showing alternating layers of depleted uranium and scintillator strips, wavelength shifters, and photomultipliers. .. 30

18: Cross-section (octant) of the CTD. 31

19: Schematic model of ep interactions. 35

20: Schematic representation of the cell island clustering. The dots denote towers which are island seeds. The trail of pointers to the neighboring tower with the most energy is shown by the thick black arrows. The thick black lines delimit the boundary of an island. 42

21: Distribution of the probability versus the polar angle of the electromagnetic cluster for (a) 225 GeV $e^* \to e\gamma$ (the final electron), (b) 225 GeV $e^* \to e\gamma$ (the final photon), (c) 225 GeV $e^* \to eZ \to eq\bar{q}$, (d) 225 GeV $e^* \to eZ \to e\nu\bar{\nu}$, (e) NC DIS Monte Carlo, and (f) data. 45

22: The efficiency (ϵ^{Found}) of EM and Sinistra (Sira 5) electron finders versus (a) the energy, (b)the polar angle of the electron found, and (c) Q^2. Horizontal lines represent 2% loss (upper line) and 5% loss (lower line), vertical full lines indicate calorimeter limits and vertical dashed lines represent CTD end. [42]. 47

23: The mean difference between the true and reconstruction corrected (solid histogram) and uncorrected (dashed histogram) (a) electron energy, and (b) the polar angle of the electron for NC DIS Monte Carlo. 48

24: The distribution of the track momenta ($P_{t,EM}^{Trk}$) for (a) data (solid black point) and NC DIS (open histogram) Monte Carlo, and for (b) 125 GeV (solid line) and 225 GeV (dotted line) $e^* \to \nu W \to \nu\bar{\nu}e$, 125 GeV (dash-dotted line) and 225 GeV dashed line) $e^* \to eZ \to eq\bar{q}$ Monte Carlo. The $P_{t,EM}^{Trk}$ distributions for $e^* \to eZ \to e\nu\bar{\nu}$ are similar to those for $e^* \to eZ \to eq\bar{q}$. 49

25: The distribution of the energy in an $\eta - \phi$ cone of radius 0.8 that is not assigned to the electromagnetic cluster candidate, $E_e^{iso}(R < 0.8)$, for (a) data (solid black pont) and NC DIS (open histogram) Monte Carlo, and for (b) 125 GeV (solid line) and 225 GeV (dashed line) $e^* \to e\gamma$, (c) 125 GeV (solid line) and 225 GeV (dashed line) $e^* \to eZ \to e\nu\bar{\nu}$, (d) 125 GeV (solid line) and 225 GeV (dashed line) $e^* \to eZ \to eq\bar{q}$. The $E_e^{iso}(R < 0.8)$ distributions for $e^* \to \nu W \to \nu\bar{\nu}e$ are similar to those for $e^* \to eZ \to e\nu\bar{\nu}$. 50

26: (a) The z-vertex distribution along the beam axis, (b) the x- and (c) y-vertex distributions. 56

27: Typical signature of (a) an nominal ep interaction, (b) the beam-gas events, and (c) the cosmic muon. (d) Distribution of the signal time measured in the RCAL (t_r) versus the difference $t_f - t_r$ between the signal times seen in FCAL and RCAL. 59

28: Comparison of data and total background Monte Carlo for the e^* events sample with an electromagnetic cluster in the final state. Distribution of (a) the electromagnetic cluster energy, (b) the transverse energy of the electromagnetic cluster, (c) the polar angle of the electromagnetic shower, (d) the longitudinal energy

$E - P_z$. 63

29: The distribution of the ratio of good tracks to total tracks before applying the cut on good tracks. 65

30: Comparison of data and background Monte Carlo (CC DIS + Photoproduction + NC DIS) for the sample of e^* events without an electromagnetic cluster in their final state. Distribution of (a) the missing transverse momentum, (b) the longitudinal energy $E - P_z$, (c) the hadronic transverse energy, (d) the number of good tracks. 66

31: Comparison of the resolution determined in invariant mass $M_{e\gamma}$ using the double angle method and the standard calorimeter energy (Cal-Energy) method for $e^* \to e\gamma$ as a function of e^* mass. The smooth curves are polynomial fits to the points. 71

32: Distribution of the $e\gamma$ invariant mass for 125, 175, and 250 GeV $e^* \to e\gamma$ using the double angle method (solid histograms) and the standard calorimeter energy (Cal-Energy) method (dashed histograms). 72

33: Comparison of the resolution in invariant mass M_{eZ} using the electron information (energy and polar angle of the electron) and the standard calorimeter energy (Cal-Energy) method for $e^* \to eZ$ as a function of e^* mass. The smooth curves are polynomial fits to the points. 73

34: Distribution of the eZ invariant mass for 125, 175, and 250 GeV $e^* \to eZ \to eq\bar{q}$ using the double angle method (solid histograms) and the standard calorimeter energy (Cal-Energy) method (dashed histograms). 73

35: Diagrams for the production and decay of excited electron $e^* \to e\gamma$ via (a) elastic and (b) inelastic processes in ep collisions. 75

36: The distribution of transverse energy (after cleaning cuts) of (a) the highest E_t electromagnetic cluster (E_t^{EM1}), and (b) those of the the second highest electromagnetic cluster (E_t^{EM2}), for 125 GeV (solid line) and 225 GeV (dashed line) $e^*(\rightarrow e\gamma)$, NC DIS (dash-dotted line), QED-Compton Monte Carlo (dotted line), The accepted region is to the right of the dashed vertical lines. 76

37: The distribution of transverse energy (after cleaning cuts) of the highest E_t electromagnetic cluster versus that of the second highest E_t electromagnetic shower for (a) 125 GeV, (b) 175 GeV, (c) 225 GeV $e^*(\rightarrow e\gamma)$, (d) QED-Compton, and (e) NC DIS Monte Carlo, and (d) data. 78

38: The distribution of the energy in an $\eta - \phi$ cone of radius 0.8 that is not assigned to the electromagnetic cluster candidate (after cut on electromagnetic cluster transverse energies) of the highest E_t (solid line) and that of the second highest E_t (dashed line) electromagnetic cluster for (a) 125 GeV $e^* \rightarrow e\gamma$, (b) QED-Compton, and (c) NC DIS Monte Carlo. The distribution for higher mass $e^* \rightarrow e\gamma$ Monte Carlo events are similar to those shown in (a). 79

39: The polar angle distribution (after a cut on E_t and isolation of the electromagnetic clusters) of (a) the highest E_t electromagnetic cluster (θ_{EM1}), and (b) of the the second highest electromagnetic cluster (θ_{EM2}), for 125 GeV (solid line) and 225 GeV (dashed line) $e^*(\rightarrow e\gamma)$. The rejected events are to the right of the dashed vertical lines. 80

40: The distribution of polar angle (after cut on E_t and isolation of the electromagnetic clusters) of the highest E_t electromagnetic cluster versus that of the second highest E_t electromagnetic shower for (a) 125 GeV, (b) 175 GeV, (c) 225 GeV $e^*(\rightarrow e\gamma)$, and (d) QED-Compton, and (e) NC DIS Monte Carlo events, and (f) data. 82

41: The distribution of the energy asymmetry, $\Delta E_t^{EM}/\sum E_t^{EM}$, (after cut on E_t and θ and isolation of the electromagnetic clusters and $E-P_z$) for (a) 125 GeV (solid line) and 225 GeV (dashed line) $e^*(\rightarrow e\gamma)$, (b) NC DIS (solid line), and QED-Compton Monte Carlo (dashed line). The rejected events are to the right of the dashed vertical lines. 83

42: The distribution of number of good tracks (after cut on E_t and θ and isolation of the electromagnetic clusters and $E-P_z$ and energy asymmetry) for (a) 125 GeV (solid line) and 225 GeV (dashed line) $e^*(\rightarrow e\gamma)$, (b) NC DIS (solid line), and QED-Compton Monte Carlo (dashed line). The rejected events are to the right of the dashed vertical lines. 83

43: Comparison of data and background Monte Carlo after all cuts in the $e\gamma$ search. Distribution for (a) the transverse energy of the highest E_t electromagnetic cluster, (b) and that of the second highest E_t electromagnetic cluster, (c) the polar angle of highest E_t electromagnetic cluster, (d) and that of the second highest E_t electromagnetic cluster; (e) the longitudinal transverse momentum $E-P_z$, (f) the asymmetry between the transverse energy of the two electromagnetic clusters, and (g) the number of good tracks. The solid points show the 96+97 ZEUS data and the open histograms represent the expected total background from NC DIS and QED-Compton Monte Carlo events. The contribution from the QED-Compton process is shown by the shaded histograms. 84

44: (a) Efficiency and (b) width of the reconstructed mass (mass resolution) for Monte Carlo e^* events decaying into $e\gamma$ as a function of the mass of the excited electron. The smooth curves are polynomial fits to the points. 87

45: Invariant mass distribution of the $e\gamma$ system for $e^* \rightarrow e\gamma$ after all cuts. The solid points show the 96+97 ZEUS data and the open histogram represents the

expected total background from NC DIS and QED-Compton Monte Carlo events. The contribution from the QED-Compton process is shown by the shaded histogram. An example of a signal from e^* with a mass of 200 GeV is also shown as the dashed histogram. 87

46: The highest mass candidate event for the $e\gamma$ search. The $e\gamma$ invariant mass for this event is 158 GeV. The left part of the event display shows a vertical cut through the ZEUS detector. The protons enter from right, the electron from left. The collisions occur in the center of the detector which is surrounded by CTD and the calorimeter. The final state electron (with a track) is in the FCAL and the photon in the BCAL. The right lego plot shows the distribution of transverse energy as a function of azimuth and polar angle. 88

47: Diagrams for the production and decay of excited electron $e^* \to eZ \to eq\bar{q}$ via (a) elastic and (b) inelastic processes in ep collisions. 89

48: The distribution of (a) the hadronic transverse energy (E_t^{had}) for 125 GeV (solid line) and 225 GeV (dotted line) $e^*(\to eZ \to eq\bar{q})$, NC DIS (dashed line) after cuts on E_t and θ of the electron and $E - P_z$, and (b) the distribution of the hadronic mass (M^{had}) for 125 GeV (solid line) and 225 GeV (dotted line) $e^*(\to eZ \to eq\bar{q})$, and NC DIS (dashed line) Monte Carlo, after cuts on E_t and θ of the electron and $E - P_z$, and also requiring $E_t^{had} > 60$ GeV. 90

49: a) The difference between the reconstructed Z mass and the nominal Z mass, (b) the reconstructed Z mass resolution as a function of e^* mass. The smooth curves are polynomial fits to the points. 91

50: The distribution of the hadronic mass (M^{had}) versus the transverse hadronic energy (E_t^{had}) for (a) 125 GeV, (b) 175 GeV, (c) 225 GeV, and (d) 250 GeV $e^*(\to eZ \to eq\bar{q})$, (e) NC DIS Monte Carlo, and (f) data. The solid lines show

the cut; the accepted region is to the upper right. 92

51: The distribution of the ratio M^{Total}/M_{eZ} for 125 GeV (solid histogram) and 225 GeV (dotted histogram) $e^*(\rightarrow e\,Z \rightarrow e\,q\,\bar{q}\,)$, and NC DIS Monte Carlo (dashed histogram). The accepted region is between the two dashed lines. 93

52: Comparison of data and NC DIS background Monte Carlo after all cuts in $eq\bar{q}$ search. Distribution of (a) the electron transverse energy, (b) the polar angle of the electron, (c) the hadronic transverse energy, (d) the hadronic mass, (e) the longitudinal energy $E - P_z$, and (f) the ratio M_{Total}/M_{eZ}, where M_{Total} is the total effective mass measured with the calorimeter. 94

53: (a) Efficiency and (b) width of the reconstructed mass (mass resolution) for Monte Carlo $e^* \rightarrow eZ \rightarrow eq\bar{q}$ as a function of the mass of the excited electron. The smooth curves are polynomial fits to the points. 96

54: Invariant mass distribution of the eZ system for $e^* \rightarrow eZ \rightarrow eq\bar{q}$ after all cuts. The solid points show the 96+97 ZEUS data and the open histogram represents the expected total background from NC DIS Monte Carlo simulation. An example of a signal from e^* with a mass of 250 GeV is also shown as the dashed histogram. 96

55: The highest mass candidate event for the $eq\bar{q}$ search. The $eq\bar{q}$ invariant mass is 235 GeV. The left part of the event display shows a vertical cut through the ZEUS detector. The final state electron (with a track) is in the BCAL and the jet in the forward direction. The right lego plot shows the distribution of transverse energy as a function of azimuth and polar angle. 97

56: Diagrams for the production and decay of excited electron $e^* \rightarrow eZ \rightarrow e\nu\bar{\nu}$ or $e^* \rightarrow \nu W \rightarrow \nu e\bar{\nu}$ via (a) elastic and (b) inelastic processes in ep collisions. .. 98

57: The distribution of $\cos(\phi_{\rm e}-\phi_{\rm had})$ after cuts on E_t, θ of the the electron and P_t^{miss}, for (a) 125 GeV (solid line) and 225 GeV (dashed line) $e^* \to eZ \to e\nu\bar{\nu}$. and for (b) single W-production (solid line), NC DIS (dotted line). and CC DIS (dashed histogram) Monte Carlo. The $\cos(\phi_{\rm e} - \phi_{\rm had})$ distribution for $e^* \to \nu W \to \nu e\bar{\nu}$ are similar to those in (a). 100

58: The distribution of P_t^{miss}/E_t after cuts on E_t, θ of the the electron and P_t^{miss}, for (a) 125 GeV (solid line) and 225 GeV (dashed line) $e^* \to eZ \to e\nu\bar{\nu}$. and for (b) single W-production (solid line), NC DIS (dotted line). and CC DIS (dashed histogram) Monte Carlo. The $\cos(\phi_{\rm e}-\phi_{\rm had})$ distribution for $e^* \to \nu W \to \nu e\bar{\nu}$ are similar to those in (a). The accepted events are to right of the vertical dashed lines. 101

59: Comparison between data and background Monte Carlo before applying the acoplanarity cut in $e\nu\bar{\nu}$ search. Distribution of (a) $\cos(\phi_{\rm e}-\phi_{\rm had})$ and (b) P_t^{miss}/E_t. The solid points show the 96+97 ZEUS data and the open histogram represents the expected total background Monte Carlo simulation. The contribution from the NC DIS process is shown by the shaded histogram. 102

60: (a) Efficiency and (b) width of the reconstructed mass (mass resolution) for Monte Carlo $e^* \to eZ \to e\nu\bar{\nu}$ as a function of the mass of the excited electron. The smooth curves are polynomial fits to the points. 105

61: (a) Efficiency and (b) width of the reconstructed mass (mass resolution) for Monte Carlo $e^* \to \nu W \to \nu e\bar{\nu}$ as a function of the mass of the excited electron. .. 105

62: Invariant mass distribution of the eZ system for $e^* \to eZ \to e\nu\bar{\nu}$ after all cuts. The solid point show the 96+97 ZEUS data and the open histogram represents the expected total background and the darker histogram denotes the W-Production Monte Carlo simulation. An example of a signal from e^* with a mass of 250 GeV

is also shown as the dashed histogram. 106

63: The single candidate event for the e $\nu\bar{\nu}$ search. The eZ invariant mass is 136 GeV. The left part of the event display shows a vertical cut through the ZEUS detector. The final state electron (with a track) is in the BCAL. The right lego plot shows the distribution of transverse energy as a function of azimuth and polar angle. 106

64: Diagrams for the production and decay of excited electron $e^* \to \nu W \to \nu q\bar{q}'$ via (a) elastic and (b) inelastic processes in ep collisions. 107

65: The distribution of (a) the hadronic transverse energy (E_t^{had}) after cuts on P_t^{miss} and $E - P_z$, for 125 GeV (solid line), 225 GeV (dotted line) e_z^*, for 125 GeV (solid line), 225 GeV (dotted line) $e^* \to \nu W \to \nu q\bar{q}'$, and CC DIS (dashed line) and (b) the hadronic mass (M^{had}) after cuts on P_t^{miss} and $E - P_z$, and requiring $E_t^{had} >$ 50 GeV, for 125 GeV (solid line) and 225 GeV (dotted line) $e^* \to \nu W \to \nu q\bar{q}'$, and CC DIS (dashed line) Monte Carlo. 108

66: The reconstructed W mass resolution and the mass shift from the nominal W mass as a function of e^* mass. The smooth curves are polynomial fits to the points. 109

67: The distribution of the hadronic mass (M^{had}) versus the transverse hadronic energy (E_t^{had}) for (a) 125 GeV, (b) 175 GeV, (c) 225 GeV $e^* \to \nu W \to \nu q\bar{q}'$ signal Monte Carlo, (d) CC DIS, (e) Photoproduction, and (f) data. The dashed lines show the cut; the accepted region is to the upper right. 110

68: Comparison of data and background Monte Carlo (CC DIS + Photoproduction + NC DIS) after the all cuts in $\nu q\bar{q}'$. Distribution of (a) the missing transverse momentum, (b) the longitudinal energy $E-P_z$, (c) the hadronic transverse energy, (d) the hadronic mass. 111

69: (a) Efficiency and (b) width of the reconstructed mass (mass resolution) for Monte Carlo $e^* \to \nu W \to \nu q\bar{q}$ as a function of the mass of the excited electron. .. 113

70: Invariant mass distribution of the νW system for $e^* \to \nu W \to \nu q\bar{q}'$ after all cuts. The solid points show the 96+97 ZEUS data and the open histogram represents the expected total background and the shaded histogram denotes the CC DIS Monte Carlo simulation. An example of a signal from e^* with a mass of 250 GeV is also shown as the dashed histogram. 113

71: The highest mass candidate event for the $\nu q\bar{q}'$ search. The νW invariant mass is 211 GeV. The left part of the event display shows a vertical cut through the ZEUS detector. The jets are boosted in the forward direction. The right lego plot shows the distribution of transverse energy as a function of azimuth and polar angle. 114

72: Diagram for the production and decay of excited neutrino $\nu^* \to \nu\gamma$ in ep collisions. 116

73: The distribution of the energy in an $\eta - \phi$ cone of radius 0.8 that is not assigned to the electromagnetic cluster candidate, $E_{EM}^{iso}(R < 0.8)$, for (a) data (solid black points) and total background (open histogram) Monte Carlo, and for (b) 125 GeV (solid line) and 225 GeV (dashed line) $\nu^* \to \nu\gamma$. The rejected events are to the right of the dashed vertical lines. 117

74: Comparison of data and total background Monte Carlo with an electromagnetic cluster in the final state after the ν^* event sample cuts. Distribution of (a) the transverse energy of the electromagnetic cluster (E_t^{EM}), (b) the polar angle of the electromagnetic shower (θ_{EM}), (c) the transverse missing momentum P_t^{miss}, and (d) the total transverse energy in the calorimeter (E_t). The solid points show the 98+99 ZEUS data and the open histogram represents the expected total

background from NC DIS and CC DIS Monte Carlo events. 119

75: (a) Efficiency and (b) width of the reconstructed mass (mass resolution) for Monte Carlo ν^* events decaying into $\nu\gamma$ as a function of the mass of the excited electron. 121

76: Invariant mass distribution of the $\nu\gamma$ system for $\nu^* \to \nu\gamma$ after all cuts. The solid points show the 98+99 ZEUS data and the open histogram represents the expected total background from CC DIS and NC DIS Monte Carlo events. An example of a signal from ν^* with a mass of 225 GeV is also shown as the dashed histogram. 121

77: The highest mass candidate event for the $\nu\gamma$ search. The $\nu\gamma$ invariant mass for this event is 118 GeV. The left part of the event display shows a vertical cut through the ZEUS detector. The jets are boosted in the forward direction. The right lego plot shows the distribution of transverse energy as a function of azimuth and polar angle. 122

78: (a) The upper limit on the number of signal events, $N_{\text{U.L.}}$, and (b) variation of the upper limit for the signal, $\Delta N_{\text{U.L.}}$, as a function of systematic uncertainty with no observed events and no background. 131

79: Upper limits on the production cross-section times the branching ratio at 95% confidence level as a function of e^* mass for: (a) $\sigma(ep \to e^*X) \times BR(e^* \to e\gamma)$, (b) $\sigma(ep \to e^*X) \times BR(e^* \to \nu W \to \nu q\bar{q}')$, (c) $\sigma(ep \to e^*X) \times BR(e^* \to eZ \to eq\bar{q})$, (d) $\sigma(ep \to e^*X) \times BR(e^* \to eZ \to e\nu\bar{\nu})$. The thick lines show the limits from the 96-97 ZEUS results. The thin lines and the dashed line represent the limits from previous ZEUS publication [12]. 137

80: Upper limits on the combined production cross-section times the branching ratio at 95% confidence level as a function of e^* for $\sigma(e^+p \to e^*X) \times BR(e^* \to eZ \to$

$eq\bar{q}$) and $\sigma(e^+p \to e^*X) \times BR(e^* \to eZ \to e\nu\bar{\nu})$. 138

81: Upper limits on the production cross-section times the branching ratio at 95% confidence level as a function of ν^* mass for $\sigma(ep \to \nu^*X) \times BR(\nu^* \to \nu\gamma)$. The solid line shows the limits from the 98-99 ZEUS results. The dashed and dotted lines represent the limits from previous ZEUS publications [12, 13]. 138

82: The upper limit at 95% confidence level on the coupling f/Λ as a function of the e^* mass assuming $f = f'$. Four solid lines are limits for $e^* \to e\,\gamma$, $e^* \to \nu\,W \to \nu\,q\,\bar{q}'$, $e^* \to e\,Z \to e\,q\,\bar{q}$, and $e^* \to e\,Z \to e\,\nu\,\bar{\nu}$ respectively, and the dashed curve represents the combined limit from four channels. The shaded line is the limit from the DELPHI experiment [53], where the limit variations are approximated by the line width. In all cases the areas above the lines are excluded. 142

83: Upper limit at 95% confidence level on the coupling f/Λ as a function of the ν^* mass assuming $f = -f'$. Also limits from previous ZEUS results from e^-p data (thin curve) [13], and e^+p data (dashed curve) [12] are shown. The shaded line is the limit from the DELPHI experiment [53], where the limit variations are approximated by the line width. In all cases the areas above the lines are excluded. 143

List of Appendices

1: Definition of DST Bits. 146

2: Derivation of Mass Formulae. 153

Chapter 1

Introduction

For many decades, physicists have attempted to explain the interactions among subatomic particles as well as their properties. The result of these extensive observations is the now widely accepted Standard Model [1], which is a reliable, testable, and highly predictive theory.

According to the Standard Model, all matter is composed of spin-$\frac{1}{2}$ fermion constituents which come in three distinct generations. Each generation contains a charged lepton (the electron -e, muon -μ, and tau -τ) and its corresponding neutrino, and a pair of quarks (q) with charges $+\frac{2}{3}$ (the up -u, charm -c, and top -t quarks) and -$\frac{1}{3}$ (the down -d, strange -s, and bottom -b quarks). These constituents interact through the electromagnetic, weak, and strong nuclear forces by the exchange of integral spin particles called gauge bosons (photon -γ, $-Z$, $-W$, and gluon -g). Only the quarks feel the effects of the strong nuclear force. The quarks and the leptons are subject to the weak nuclear force. All particles that have electric charge, including the W, feel the electromagnetic force. The electromagnetic, weak and strong interactions are unified in a theory based on the $U(1)$, $SU(2)$, and $SU(3)$ groups.

In this model, quarks and leptons, together with gauge bosons, are all assumed to be elementary, that is to say, they are treated as point particles, without internal

structure.

However, one of the main criticisms about this model is that it does not predict the fermion masses or the number of families of fermions. These and other parameters have to be determined by experiment.

In 1965, as a test of quantum electrodynamics at small distances, measurement of electron-pair production in the energy range from 1 to 6 GeV indicated a deviation from quantum electrodynamics [2]. This led to consideration of the possible existence of an excited electron as suggested by F. E. Low [3]. The heavy excited electron (e^*) could be produced by the the reaction $e + p \rightarrow e^* + p$ with the subsequent decay $e^* \rightarrow e\,\gamma$.

It had been noticed that measurements of the electrons' and muons' anomalous magnetic moment would give strong limitations on a possible substructure of leptons [4]. Later with the advent of the e^+e^- colliding beam facilities PETRA at DESY [5] and PEP at SLAC [6], tests of the validity of quantum electrodynamics at larger momentum transfers became possible and interest in the search for excited leptons was renewed.

Over the course of time, the proliferation of quarks and leptons suggested that they might be composite structures, bound states of the more fundamental constituents. Although many scientists have proposed models of such composite structure, no obviously correct or compelling model has yet emerged [7, 8, 9]. For this reason, it is important to devise experiments which probe these potential substructures deeply, as well as testing the widest possible variety of models.

In fact, if quarks and leptons are made of constituents, then at the scale of constituent binding energies, Λ ($\sim$ TeV), there should appear new interactions among quarks and leptons [10]. A typical consequence of compositeness is the appearance of excited leptons and quarks. Phenomenologically, an excited fermion is defined to be a heavy fermion which shares fermionic quantum numbers with

an existing fermion [11].

For many years, electron-proton (ep) scattering has played an important role in unraveling the structure of the nucleon. Physicists have probed the structure of the nucleons and the interaction among nucleons and leptons by scattering electrons off nuclei. Moreover, as the lepton's energy has increased, physicists have been able to obtain highly detailed information about the structure of the proton or neutron. In addition to probing the proton's structure at the HERA ep collider, excited fermions (F^*) with masses up to the kinematic limit would be directly produced via the $t-$channel boson exchange (photon/Z exchange for e^* and W exchange for ν^*) processes $ep \to F^*p$ or $ep \to F^*X$ where X is the proton remnant, as shown in Figure 1.

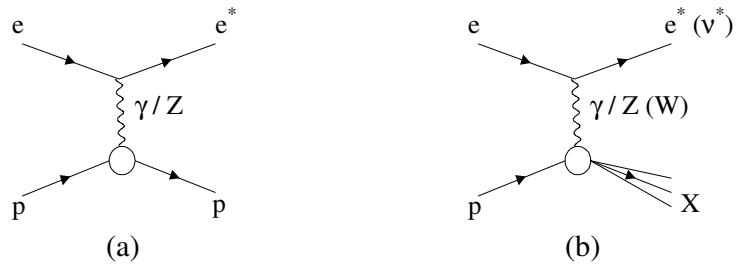

Figure 1: Diagrams for the production of excited leptons via (a) elastic and (b) inelastic processes in ep collisions.

In this analysis, heavy excited states of electrons[1] have been searched for in e^+p collisions[2] with the ZEUS detector at HERA. The data used in this analysis

[1]Throughout this work, the terms "electron" (e), "neutrino" (ν), and "antineutrino" ($\bar{\nu}$) are used to refer to electron or positron, electron-neutrino, and electron-antineutrino, respectively, unless otherwise stated.

[2]Before the 1997/1998 break, HERA was operated with 820 GeV proton and 27.5 GeV electron beam energies corresponding to a center-of-mass energy of 300 GeV. After the break, HERA was operated with 920 GeV proton and 27.5 GeV electron beam energies corresponding to a center-of-mass energy of 318 GeV.

were collected during 1996-97, corresponding to an integrated luminosity of 38.4 pb^{-1}, which is approximately four times more than in the first e^+p ZEUS analysis of this physics [12]. Excited neutrinos have been searched for in e^-p collisions using a data set corresponding to an integrated luminosity of 16.7 pb^{-1} collected during 1998-99 running period, which is approximately 30 times more than in the first e^-p excited fermion search by the ZEUS experiment [13].

Excited electrons (e^*) were sought decaying via

$$e^* \to e\gamma\,,$$

$$e^* \to eZ \to eq\bar{q}\,, e\nu\bar{\nu}\,,$$

$$e^* \to \nu W \to \nu q\bar{q}'\,, \nu\bar{\nu}e\,.$$

Excited neutrinos (ν^*) were sought decaying via

$$\nu^* \to \nu\gamma\,.$$

No evidence was found for excited electrons or neutrinos, so the data were used to set limits on cross-section and coupling.

Chapter 2

Theoretical Aspects

The basic assumption that underlies almost all composite model building is that the fundamental constituents interact by means of a new superstrong gauge interaction [7, 8, 9]. According to current theoretical ideas, below the composite scale Λ, the superstrong interaction binds the constituents into singlet states including the observed quarks and leptons. The most convincing evidence for a substructure of fermions would be the discovery of heavy excited states of fermions, which are a common prediction of all composite models.

Generally speaking, lack of a fundamental theory for the dynamics of excited fermions leads physicists to resort to a specific phenomenological model in calculating efficiencies, as well as in setting limits on the couplings and compositeness scales.

2.1 Phenomenological Model

To maintain generality in describing the excited fermion, F^*, production and decay, without specifying the dynamics of the compositeness, it has been conventional to use the phenomenological Lagrangian of Hagiwara, Komamiya, and Zeppenfeld [14] in order to describe the transitions between ordinary fermions (F)

and spin $\frac{1}{2}$ excited states. The Lagrangian is given by [14]

$$\mathcal{L}_{FF^*} = \sum_{V=\gamma,Z,W} \frac{e}{\Lambda}\, \bar{F}^*\, \sigma^{\mu\nu}\, c_{VF^*F}\, (1-\gamma_5)\, F\, \partial_\mu V_\nu + h.c.\,, \tag{1}$$

where c_{VF^*F} is the vector coupling constant at the $F \leftrightarrow F^*$ transition vertex, V is the boson to which the F and F^* couple, e is the proton electric charge, and Λ is the compositeness scale.

It is customary to choose a model in which the excited state fermions have spin and isospin $\frac{1}{2}$ so that both left-handed (F_L^*) and right-handed (F_R^*) components form weak isodoublets. In the case of the first generation leptons [14, 15, 16]

$$F_L = \begin{bmatrix} \nu_e \\ e \end{bmatrix}_L ; \quad e_R\,; \quad F_L^* = \begin{bmatrix} \nu_e^* \\ e^* \end{bmatrix}_L ; \quad F_R^* = \begin{bmatrix} \nu_e^* \\ e^* \end{bmatrix}_R$$

In describing the transition between excited fermions and ordinary fermions, the Lagrangian should respect chiral symmetry in order to protect the light leptons from acquiring a large mass [16, 17]. This means that only the right-handed part of the excited fermions couple to the left-handed ordinary fermions. This transition is described in a form by the following Lagrangian [14, 15, 16]

$$\mathcal{L}_{F^*F} = \frac{1}{\Lambda}\, \bar{F}_R^*\, \sigma^{\mu\nu} \left[g\, f\, \frac{\tau}{2}\, \partial_\mu W_\nu + g'\, f'\, \frac{Y}{2}\, \partial_\mu B_\nu \right] F_L + h.c.,\tag{2}$$

where B_ν and W_ν are the $U(1)$ and $SU(2)$ fields; τ and Y are the corresponding gauge group generators; and g, g' are the corresponding gauge group coupling constants. The free parameters f and f' are weight factors associated with the two gauge groups and depend on the specific dynamics describing the compositeness. The coupling constants of Eq. (1) may be expressed:

$$c_{\gamma e^* e} = -\frac{1}{2}\,(f + f') \tag{3}$$

$$c_{Ze^*e} = -\frac{1}{2}(f \cot\theta_W - f' \tan\theta_W) \tag{4}$$

$$c_{We^*\nu} = \frac{1}{\sqrt{2}}\,\frac{f}{\sin\theta_W}, \tag{5}$$

$$c_{\gamma\nu^*\nu} = -\frac{1}{2}(f - f'), \tag{6}$$

$$c_{Z\nu^*\nu} = \frac{1}{2}(f\cot\theta_W + f'\tan\theta_W), \tag{7}$$

$$c_{W\nu^*e} = \frac{1}{\sqrt{2}}\frac{f}{\sin\theta_W}. \tag{8}$$

where θ_W is the weak mixing angle.

2.2 Production Cross-section

Based on the effective Lagrangian (1), the cross-section for F^* production can be written as [14, 15]

$$\sigma(ep \to F^*X) = \int_{\frac{M_{F^*}^2+Q_o^2}{s}}^1 dx \int_{Q_o^2}^{sx-M_{F^*}^2} dQ^2 \sum_q q(x,Q^2)\,\frac{d\hat{\sigma}}{dQ^2}(eq \to F^*q')\,. \tag{9}$$

$q(x,Q^2)$ is the effective quark distribution in the proton where Q^2 is the square of the four-momentum transfer carried by the exchanged boson, x is the fraction of proton momentum carried by the struck quark, and the parton cross-section is

$$\frac{d\hat{\sigma}(eq \to F^*q')}{dQ^2} = \frac{2\pi\alpha^2}{\hat{s}^2\Lambda^2}Q^2\Big(\Phi\,A \pm \Psi\,B\Big)\,, \tag{10}$$

where

$$\Phi = 2\hat{s}^2 - (Q^2 + M_{F^*}^2)(2\hat{s} - M_{F^*}^2), \qquad \Psi = M_{F^*}^2(2\hat{s} - Q^2 - M_{F^*}^2),$$

and

$$A = \frac{2c_{\gamma e^*e}^2}{Q^4} + \frac{4c_V^e\,c_{\gamma e^*e}\,c_{Ze^*e}}{Q^2\,(Q^2+M_Z^2)} + \frac{2({c_V^e}^2 + {c_A^e}^2)\,c_{Ze^*e}^2}{(Q^2+M_Z^2)^2},$$

$$B = \frac{4c_A^e\,c_{\gamma e^*e}\,c_{Ze^*e}}{Q^2\,(Q^2+M_Z^2)} + \frac{4c_V^e\,c_A^e\,c_{Ze^*e}^2}{(Q^2+M_Z^2)^2},$$

for e^* and

$$A = \frac{2\,({c_V^\nu}^2 + {c_A^\nu}^2)\,c_{W\nu^*e}^2}{(Q^2+M_W^2)^2} \qquad \text{and} \qquad B = \frac{4\,c_V^\nu\,c_A^\nu\,c_{W\nu^*e}^2}{(Q^2+M_W^2)^2}.$$

for ν^*. M_{F^*} and M_Z are the masses of the excited lepton and Z boson respectively, $\hat{s} = xs$, and $Q_o^2 \sim 5$ GeV^2 is a low-Q^2 cut which represents the limit of validity of the parton model, α is the fine structure constant and c_V^e, c_V^ν, c_A^e, and c_A^ν are the vector and axial-vector couplings in the Standard Model. The plus sign in Eq. (10) has to be taken for electron scattering of quarks or positron scattering of antiquarks, and the minus sign is taken for positron scattering of quarks or electron scattering of anti-quarks.

Regarding e^* production, a sizable contribution at low-Q^2 is to be expected due to t-channel γ/Z exchange. For $f \approx f'$, a significant fraction of excited electrons would be produced elastically because of the $\frac{1}{Q^2}$ dependence of the photon propagator and would comprise roughly 50% of the total e^* production [14]. Since the parton model is unreliable in the low-Q^2 region, we should use the experimental information on the structure functions F_1 and F_2 of the proton directly. In terms of structure functions the differential cross-section due to photon exchange[3] reads [14, 15]

$$\begin{aligned}
\frac{d^2\sigma}{d\tilde{W}^2\, dQ^2} &= \frac{2\,\pi\alpha^2}{\Lambda^2}\frac{|c_{\gamma e^* e}|^2}{(s-m_p^2)^2\,Q^2}\Bigg\{2F_1(x,Q^2)(2\,M_{e^*}^2 - Q^2)(M_{e^*}^2 + Q^2) \\
&\quad + F_2(x,Q^2)\Bigg[\frac{4(s-m_p^2)^2\,Q^2}{\tilde{W}^2 + Q^2 - m_p^2} - (M_{e^*}^2 + Q^2) \\
&\quad .\Big(4s - \tilde{W}^2 - Q^2 - 3m_p^2 + \frac{4m_p^2\,M_{e^*}^2}{\tilde{W}^2 + Q^2 - m_p^2}\Big)\Bigg]\Bigg\}, \qquad (11)
\end{aligned}$$

where $\tilde{W}$ is the invariant mass of the final hadron system, and m_p and $M_{e^*}^2$ are the proton and e^* masses. The elastic contribution is obtained by inserting the form factors

$$F_1(x,Q^2) = \delta(\tilde{W}^2 - m_p^2)\,\frac{Q^2}{2}\,G_M^2(Q^2)\,,$$

[3]Monte Carlo studies showed that the inclusion of t-channel Z-exchange mechanism represented only a 3.5% increase in overall production cross-section [13].

$$F_2(x,Q^2) \;=\; \delta(\tilde{W}^2 - m_p^2)\,Q^2.\left[G_E^2(Q^2) + \frac{Q^2.G_M^2(Q^2)}{4m_p^2}\right].\left(1+\frac{Q^2}{4m_p^2}\right)^{-1}$$

into Eq. (11). We use the dipole fit for the electric and magnetic form factors G_E and G_M of the proton

$$G_E^2(Q^2) \approx \frac{G_M^2(Q^2)}{2.79} \approx \left(\frac{1}{1+Q^2/0.71GeV^2}\right)^{-2}.$$

Figure 2 shows the total e^* production cross-section versus e^* mass in ep collisions at $\sqrt{s} = 314$ GeV with transition couplings $f/\Lambda = f'/\Lambda = 1$ TeV^{-1}.

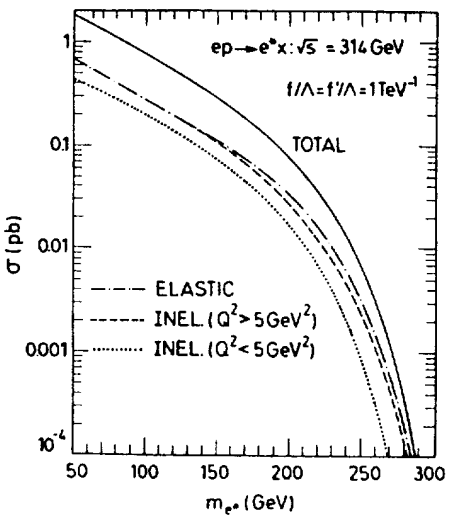

Figure 2: Total e^* production cross-section versus e^* mass in ep collisions at $\sqrt{s} = 314$ GeV with $f/\Lambda = f'/\Lambda$=1 TeV^{-1}. Elastic (dash-dotted line), inelastic low-Q^2 (dotted line), and deep inelastic contributions (dashed line) are shown separately [14].

Excited neutrino production proceeds via W exchange (Figure 1) and leads to a cross-section for e^-p collisions which is, in the high mass range $M_{\nu^*} > 200$ GeV, two orders of magnitude higher than that for e^+p. Figure 3 compares the predicted cross-section for excited neutrino production in e^+p collisions with that in e^-p collisions assuming $f/\Lambda = f'/\Lambda = 1$ TeV^{-1}. The suppression of the e^+p cross-section with respect to that of the e^-p cross-section is partly due the approximate

factor of two difference between the u and d valence quark distributions in the proton, but is mainly due to the chiral nature of W exchange.[4] Cutting away the low-Q^2 region is a good approximation for ν^* production and the cross-section is given by Eq. (9).

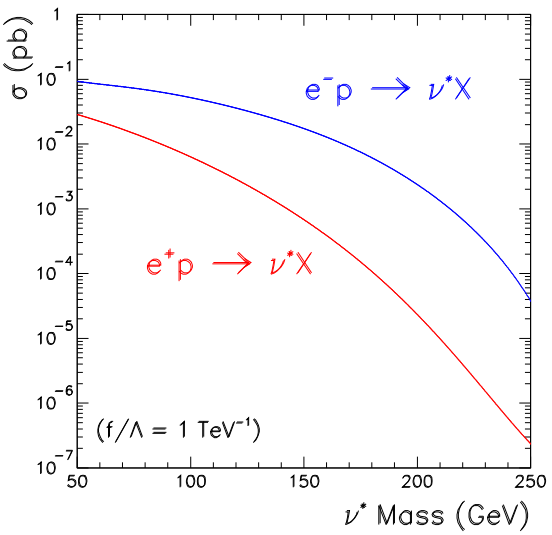

Figure 3: Comparison of the predicted cross-section for excited neutrino production in e^+p collisions versus e^-p collisions for $f/\Lambda = f'/\Lambda = 1$ TeV^{-1}.

2.3 Decay Modes

Once produced, the excited leptons can decay into light standard fermions and gauge bosons. Within this model, the partial electroweak decay width for $F^* \to VF$ follows from [14, 15, 16] and is given by

$$\Gamma(F^* \to VF) = \alpha \, \frac{m_{F^*}^3}{\Lambda^2} \, |c_{VF^*F}|^2 \left(1 - \frac{M_V^2}{M_{F^*}^2}\right)^2 \left(1 + \frac{M_V^2}{2\,M_{F^*}^2}\right), \qquad (12)$$

[4] This is manifested in the "$\pm$" sign in Eq. (10) which significantly alters the production cross-section for e^+p collisions versus e^-p collisions.

where V might be γ, Z or W, with the constraint that $M_{F^*} > M_V$, where M_V is the mass of the boson V. For the excited electron search, the conventional relation $f = f'$ is assumed. Figure 4 presents the branching ratio for $e^* \to e\gamma$, eZ, νW as a function of the mass of the e^* for $f/\Lambda = f'/\Lambda = 1$ TeV^{-1}. Under this condition the e^* total decay width varies from 2.7×10^{-3} to 9.9×10^{-2} GeV in the mass range 100 to 250 GeV.

For the excited neutrino search the process $\nu^* \to \nu\gamma$ is forbidden if $f = f'$, see Eq. (6). The convention $f = -f'$ is used for ν^* search in this channel. According to Eqs. (3-8) and (12) the decay width and branching ratio for decay processes $\nu^* \to \nu\gamma\,, \nu Z$ and eW assuming $f = -f'$ would be the same as those for $e^* \to e\gamma\,, eZ$, and νW respectively under condition $f = f'$.

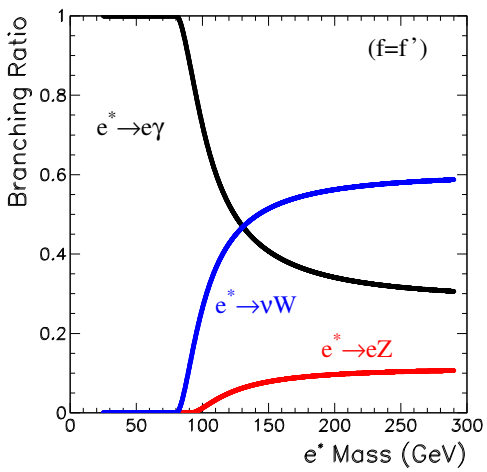

Figure 4: The branching ratio for $e^* \to e\gamma$, eZ, νW as a function of the mass of the excited electron.

Chapter 3

Experimental Procedure

Excited electrons and neutrinos, in this analysis, were studied through their decays into a Standard Model fermion and a gauge boson. There is considerable variation in the signatures of various decay modes of e^*. Excited electrons and neutrinos always decay into an electron and a gauge boson,

$$e^* \to e\gamma\,,$$

$$e^* \to eZ \to eq\bar{q}\,, e\nu\bar{\nu}\,,$$

or a neutrino and a boson,

$$e^* \to \nu W \to \nu\bar{\nu}e\,,$$

$$e^* \to \nu W \to \nu q\bar{q}'\,,$$

$$\nu^* \to \nu\gamma\,.$$

Some of these decays have an electron and no missing transverse momentum, which is similar to the signature of a neutral current deep inelastic scattering (NC DIS) event. In NC DIS the jet from the struck parton in the proton is detected and balanced by the electron.

The other decays contain neutrinos (with or without an electron) and thus have missing transverse momentum. The main characteristic of a charged current deep

inelastic scattering (CC DIS) or single W-production events in the final state is also missing transverse momentum. Almost the same topology as NC DIS occurs for the process of e^* decaying into an electron and a dijet. Similarly the same topology as CC DIS occurs for the process of a neutrino and a dijet. For all these reasons, the NC DIS and CC DIS processes in ep scattering are background to F^* production and must be considered carefully.

The final states considered are listed in Table 1. The table also presents the decay signature and the main background sources for the excited electron and neutrino decay topologies investigated.

Table 1: Excited electron and neutrino decays and topologies, and backgrounds to e^* and ν^* production. The abbreviations EM, P_t^{miss}, E_t^{had}, and M^{had} stand for electromagnetic cluster, missing transverse energy, hadronic transverse energy, and hadronic invariant mass, and NC, CC, Compton, PHP, and W for neutral current, charged current deep inelastic scattering, QED-Compton scattering, photoproduction, and W-production, respectively.

Excited Fermion	Final State	Topology	Background
$e^* \to e\gamma$	$e\gamma$	2 EM + high E_t	NC+Compton
$e^* \to eZ$	$eq\bar{q}$	1 EM + high E_t^{had} + M^{had}	NC
$e^* \to eZ$	$e\nu\bar{\nu}$	1 EM + high P_t^{miss}	NC+W+CC
$e^* \to \nu W$	$\nu e\bar{\nu}$	1 EM + high P_t^{miss}	NC+W+CC
$e^* \to \nu W$	$\nu q\bar{q}'$	high E_t^{had} + M^{had} + P_t^{miss}	CC+PHP+NC
$\nu^* \to \nu\gamma$	$\nu\gamma$	1 EM (No track) + high P_t^{miss}	CC

Some decays of excited electrons or neutrino have characteristic event topologies that help make them distinguishable from backgrounds. For instance the $e\gamma$, $eq\bar{q}$, or $e\nu\bar{\nu}$ decay modes of e^* always contain a high transverse energy electron as

shown in Figure 5. Requiring the electromagnetic shower energy to exceed a minimum value suppresses the background and reduces the number of fake candidates from $\pi^0 \to \gamma\gamma$ decays. Contrary to the processes in low-Q^2 NC DIS and QED-Compton scattering, the electron or photon from high mass F^* decays tend to be in the forward hemisphere[5] as shown in Figure 6. In order to distinguish between such e^* or ν^* decays from backgrounds, the polar angle of the electromagnetic shower should exceed a minimum.

The $\nu q\bar{q}'$ and $\nu\bar{\nu}e$ final states and $\nu\gamma$ decay of ν^* contain a neutrino. The neutrino will cause an imbalance in transverse momentum (Figure 7).

In final state events where energy is not lost down the rear beam pipe, the value of longitudinal energy variable, $E - P_z$, should be approximately twice the incident electron beam energy (55 GeV), where E and P_z are the total energy and longitudinal momentum in the calorimeter. This is the case for NC DIS events, but the neutrino in CC events and the loss of the electron through the beam pipe in photoproduction events causes the variable $E - P_z$ to be less than value of twice incident electron beam energy in these type of events as shown in Figure 8.

In the following, we study the main background sources relevant to this analysis in more detail.

3.1 Deep Inelastic Scattering

In deep inelastic scattering the incoming electron couples to the electroweak current which probes the structure of the proton. The neutral current (NC) and charged current (CC) components of the current can be distinguished by the final state electron or neutrino. In the most general case the lepton-nucleon interaction

[5] In the ZEUS coordinate system, the $+Z$ direction is defined as the proton beam direction, and referred to as forward direction.

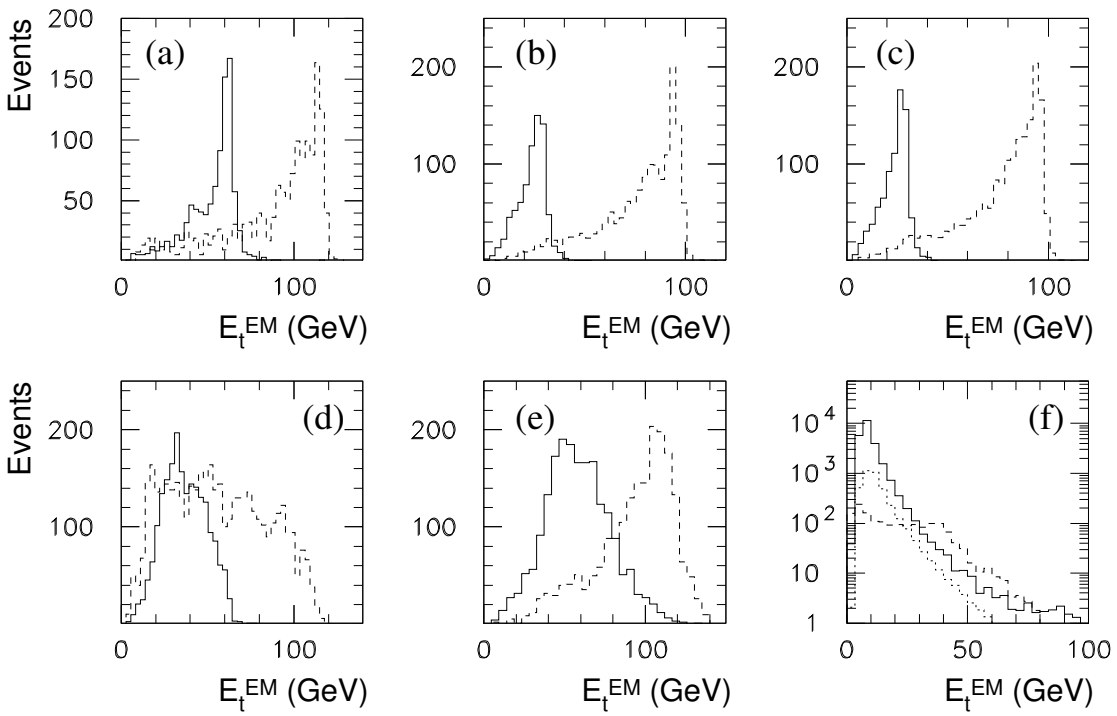

Figure 5: Distribution of transverse energy of the electromagnetic cluster (E_t^{EM}) for (a) 125 GeV (solid line) and 225 GeV (dashed line) $e^* \to e\gamma$, (b) 125 GeV (solid line) and 225 GeV (dashed line) $e^* \to eZ \to eq\bar{q}$ Monte Carlo, (c) 125 GeV (solid line) and 225 GeV (dashed line) $e^* \to eZ \to e\nu\bar{\nu}$, (d) 125 GeV (solid line) and 225 GeV (dashed line) $e^* \to \nu W \to \nu\bar{\nu}e$, (e) 125 GeV (solid line) and 225 GeV (dashed line) $\nu^* \to \nu\gamma$ Monte Carlo, and (f) NC DIS (solid line), single W-production (dashed line). and QED-Compton Monte Carlo (dotted line).

proceeds via the exchange of a virtual vector boson as depicted in Figure 9.

Assuming that k, k', P, P' are the four-vectors of the initial and final leptons, of the incoming nucleon and of the outgoing hadronic system, the usual variables describing the lepton-nucleon scattering are

$$Q^2 = -q^2 = -(k-k')^2\,, \tag{13}$$

$$x = \frac{Q^2}{2P.q} \qquad (0 \le x \le 1), \tag{14}$$

$$s = (k+P)^2 \approx \sqrt{4E_p^b E_e^b}\,, \tag{15}$$

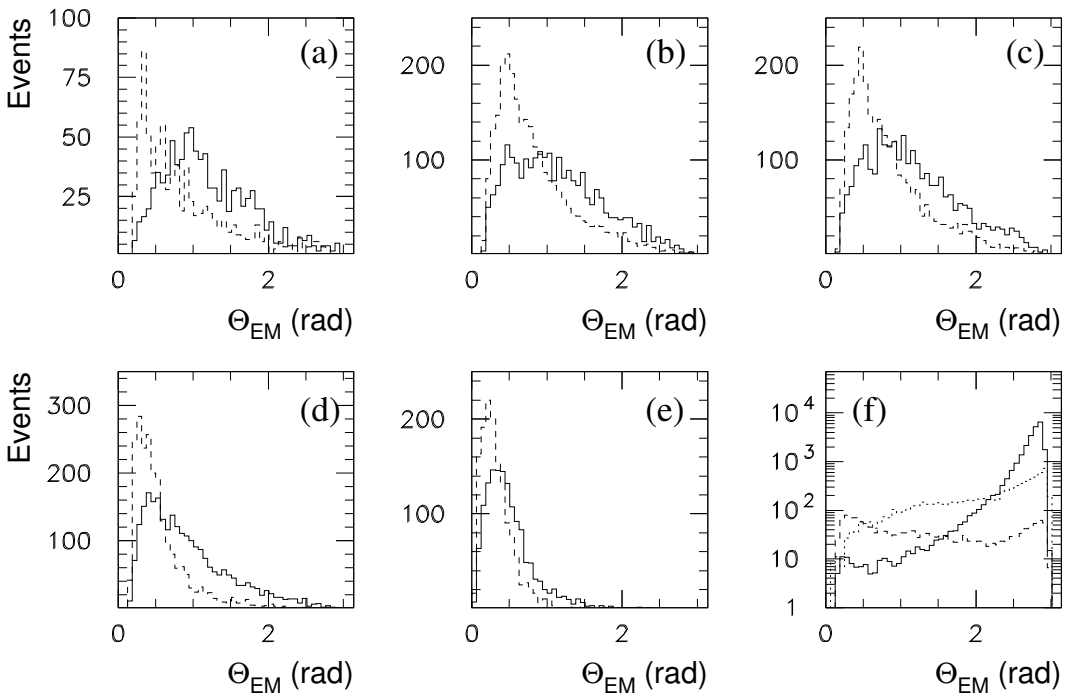

Figure 6: The polar angle distribution of the electromagnetic cluster (θ_{EM}) for (a) 125 GeV (solid line) and 225 GeV (dashed line) $e^* \to e\gamma$, (b) 125 GeV (solid line) and 225 GeV (dashed line) $e^* \to eZ \to eq\bar{q}$, (c) 125 GeV (solid line) and 225 GeV (dashed line) $e^* \to eZ \to e\nu\bar{\nu}$, (d) 125 GeV (solid line) and 225 GeV (dashed line) $e^* \to \nu W \to \nu\bar{\nu}e$, (e) 125 GeV (solid line) and 225 GeV (dashed line) $\nu^* \to \nu\gamma$, and (f) NC DIS (solid line), single W-production (dashed line). and QED-Compton Monte Carlo (dotted line).

where E_p^b and E_e^b are the energy of the incoming proton and electron, respectively, and x is the fraction of proton momentum carried by the struck quark.

The NC events mainly populate the kinematic region of low-Q^2 because of the $\frac{1}{Q^4}$ dependence of the DIS cross-section. The CC cross-section ($\frac{d\sigma}{dQ^2} \sim \frac{1}{(Q^2+M_W^2)^2}$) on the other hand approaches a constant value as $Q^2 \to 0$ due to the W propagator. For $Q^2 \approx 1$ GeV^2 the cross-section for NC is about 10^8 times larger than the cross-section for CC. At $Q^2 = M_W^2$ the differential cross-sections for NC and CC have

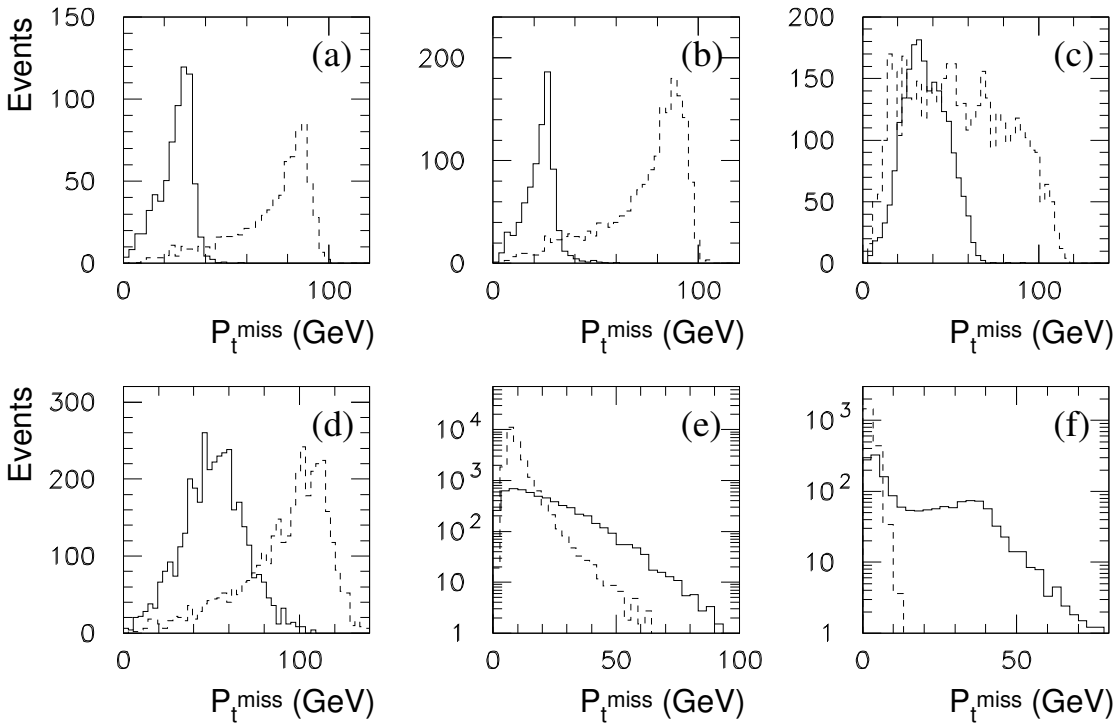

Figure 7: Distribution of the missing transverse momentum (P_t^{miss}) for (a) 125 GeV (solid line) and 225 GeV (dashed line) $e^* \to \nu W \to \nu q\bar{q}'$, (b) 125 GeV (solid line) and 225 GeV (dashed line) $e^* \to eZ \to e\nu\bar{\nu}$ Monte Carlo, (c) 125 GeV (solid line) and 225 GeV (dotted line) $e^* \to \nu W \to \nu\bar{\nu}e$, (d) 125 GeV (solid line) and 225 GeV (dashed line) $\nu^* \to \nu\gamma$, (e) CC DIS (solid line), NC DIS (dashed line), and (f) single W-production (solid line) and photoproduction (dashed line) Monte Carlo.

the same magnitude and with increasing Q^2 the differential CC cross-section falls off more slowly than the differential NC cross-section.

3.2 QED-Compton Scattering

The experimental signature of QED-Compton events is an electron-photon pair with a balanced condition in the transverse energy and low visible hadronic activity. This hadronic activity is lost down the beam pipe. A schematic diagram

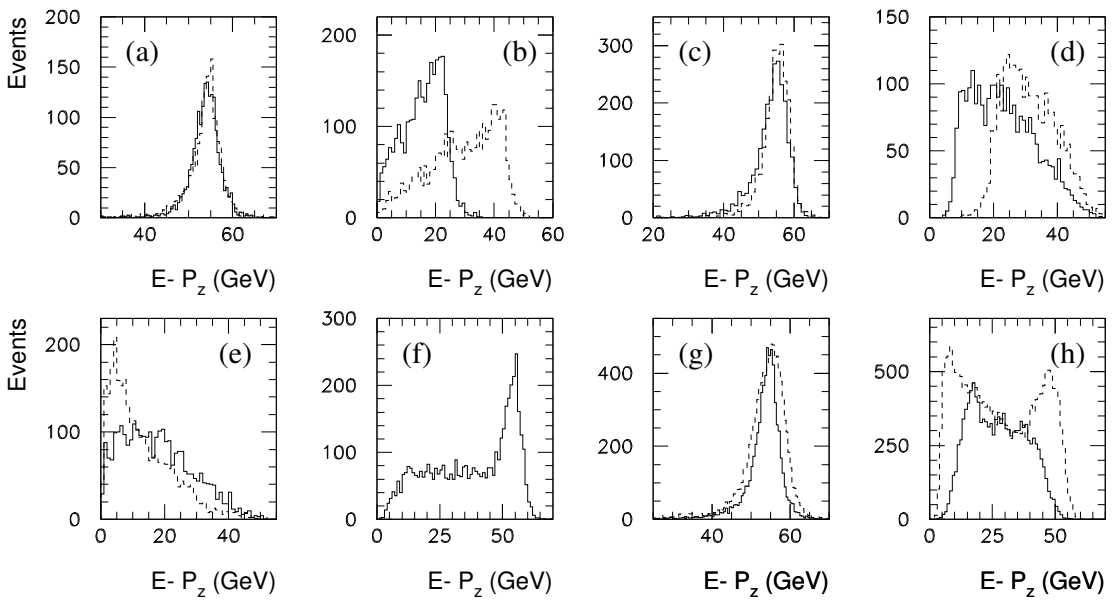

Figure 8: Distribution of the longitudinal energy variable $(E - P_z)$ for (a) 125 GeV (solid line) and 225 GeV (dashed line) $e^* \to e\gamma$, (b) 125 GeV (solid line) and 225 GeV (dashed line) $e^* \to eZ \to e\nu\bar{\nu}$, (c) 125 GeV (solid line) and 225 GeV (dashed line) $e^* \to eZ \to eq\bar{q}$, (d) 125 GeV (solid line) and 225 GeV (dashed line) $e^* \to \nu W \to \nu q\bar{q}'$, (e) 125 GeV (solid line) and 225 GeV (dashed line) $e^* \to \nu W \to \nu\bar{\nu}e$, (f) single W-production (dashed line), (g) QED-Compton (solid line) and NC DIS (dashed line), and (h) CC DIS (solid line), and photoproduction (dashed line) Monte Carlo.

describing QED-Compton scattering is shown in Figure 10.

In a QED-Compton scattering process, the movement of the final state electron and photon is in the direction of the incoming electron, whereas the movement of the final state photon and electron in excited electron decays is toward the direction of the incoming proton. Due to the major differences in their angular distributions, the QED-Compton scattering and excited electron decays can be statistically separated.

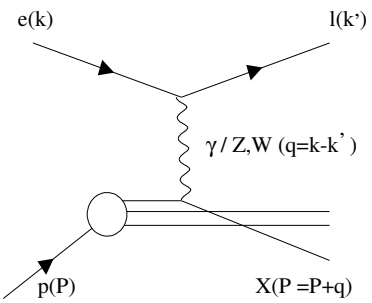

Figure 9: Schematic diagram describing deep inelastic ep scattering. The four-vectors of the particles, or particle systems, are given in parentheses. In neutral current deep inelastic scattering l is an electron (with γ/Z exchange) and in charged current process l is a neutrino (with W boson exchange).

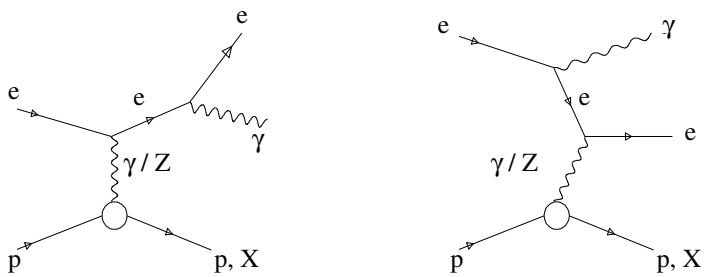

Figure 10: Schematic diagram describing QED-Compton scattering.

3.3 Photoproduction

At $Q^2 \approx 0$ the electron beam radiates photons which interact with protons. Since such photons are emitted almost parallel to the initial electron direction and are almost on the mass shell, these processes may be regarded as a photon-proton collision. Experimentally a photoproduction process is one in which the scattered electron is lost in the rear beam pipe, which restricts Q^2 to be less than a few GeV^2.

The photon may couple to a valence or sea quark. This leads to so-called "direct photon" scattering processes which have two possible diagrams in the lowest order of perturbative calculation: in case of the QCD Compton Scattering ($\gamma q \rightarrow gq$) the virtual quark emits a gluon, Figure 11(a), and in the Photon-Gluon Fusion (PFG) process ($\gamma q \rightarrow q\bar{q}$) a quark-antiquark pair is created, see Figure 11(b).

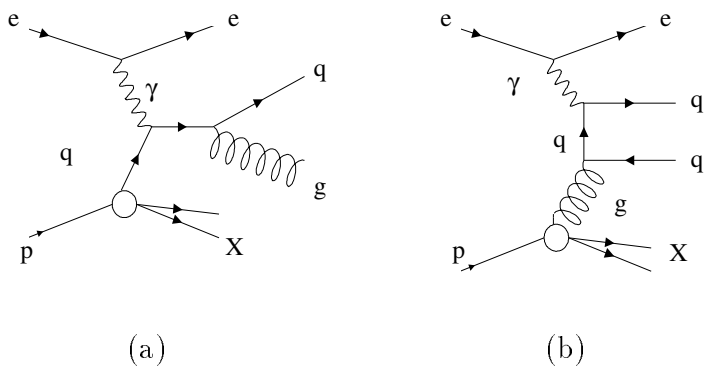

Figure 11: Schematic diagrams represent the lowest order "direct photon" processes (a) QCD Compton Scattering and (b) Photon-Gluon Fusion.

In a new class of so-called "resolved photon" processes, hard 2→2 scattering between constituents of the photon and the proton may occur, see Figure 12.

Both direct and resolved γp processes give rise to jets and these topologies can be background to F^* production.

3.4 Single W-production

The reaction

$$ep \rightarrow eW^{\pm}X$$

is the major W production process in ep collisions at HERA. It is expected to have a total cross-section about 1 pb [18]. The process

$$ep \rightarrow \nu W^{\pm}X$$

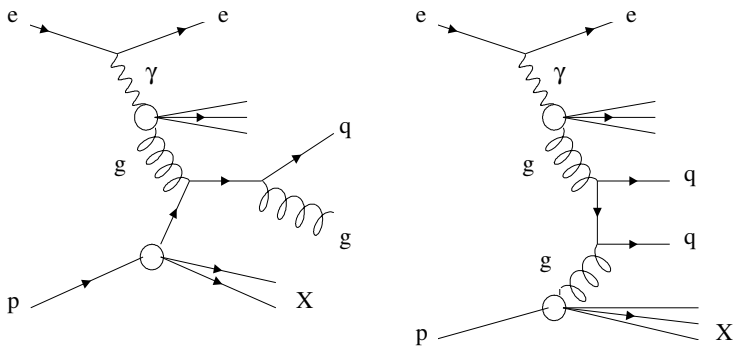

Figure 12: Diagrams for "resolved photon" processes, where the hadronic structure of the photon is manifested.

which has a very small cross-section, can be neglected at the present HERA luminosities. The graphs in Figure 13 indicate the basic contribution to the total W production cross-section in which the W boson decays into a fermion-antifermion $(f\bar{f})$ pair, either $e\nu$ or $q\bar{q}$.

In W production at $Q^2 \leq 4$ GeV^2, the electron escapes down the rear beam pipe, and the electron from W decay looks like a DIS electron. Therefore, this is a background for e^* production.

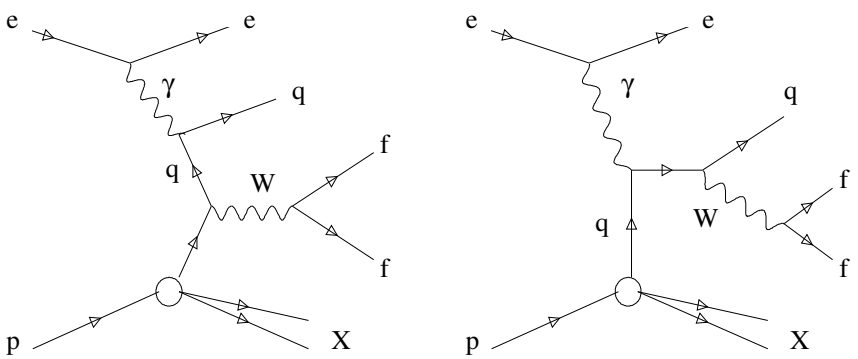

Figure 13: Feynman diagrams of the main processes contributing to the W production in the reaction $ep \to eWX$.

Chapter 4

Experiment Setup

This thesis is based on data from the ZEUS experiment at HERA. In this chapter the accelerator HERA, the ZEUS detector and the data acquisition system are described.

4.1 HERA

The Hadron Electron Ring Accelerator, HERA, is the first electron-proton collider in the world. HERA offers the unique possibility of studying the scattering between electrons of 27.5 GeV and protons of 920 GeV. The 6.3 km circumference HERA tunnel runs between 10 and 25 meters deep under ground. There are four experimental halls. The layout of the HERA ring is shown in Figure 14. The two beams consist of bunches of particles circulating in the rings in the opposite directions. At two of the four interaction points, the rings intersect each other in such a way that the two beams are brought into collision to provide ep interactions. Some of the HERA design parameters are given in Table 2.

4.2 Luminosity

HERA was operated with proton and positron beams during the 1996 to 1997

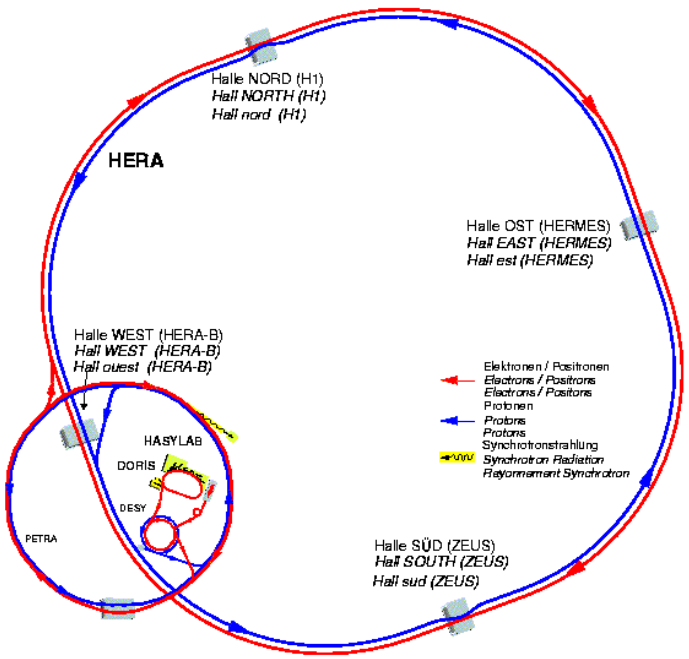

Figure 14: Layout of the HERA ring.

running period. The proton beam energy was 820 GeV and the positron beam energy was 27.5 GeV corresponding to a center-of-mass energy of 300 GeV. ZEUS collected 38.4 pb^{-1} from collisions of positrons and protons during 1996-97 data taking periods.

During the 1997/1998 break in HERA operation, new vacuum pumps were installed in the electron ring which allowed running in e^-p as well as e^+p mode. HERA was then operated with 920 GeV proton and 27.5 GeV electron beam energies corresponding a the center-of-mass energy of 318 GeV. Figure 15 shows the integral luminosity, delivered by HERA from 1994 to 1999.

Table 2. HERA parameters at the end of 1997.

Parameter	Achieved
Center-of-mass Energy, GeV	300
Proton Energy, GeV	820
Electron Energy, GeV	27.5
Luminosity, $cm^{-2}s^{-1}$	1.4×10^{31}
p-ring Magnetic Field, T	4.65
e-ring Magnetic Field, T	0.165
Proton Current, mA	100
Electron Current, mA	40
Number of bunches	189
The Time Between Crossings, ns	96

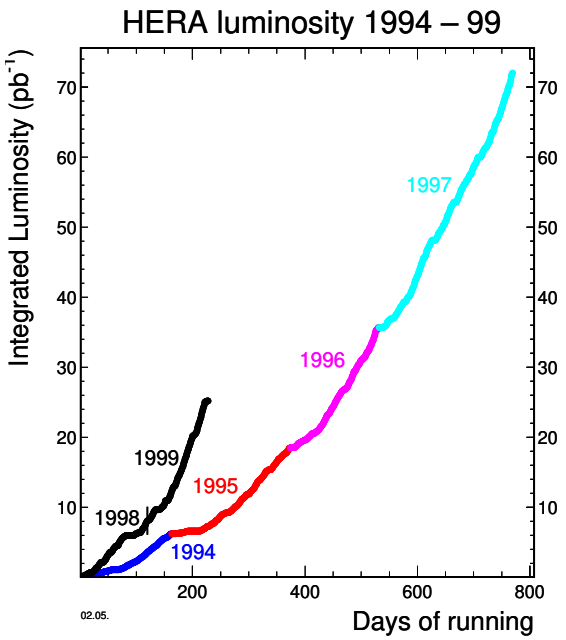

Figure 15: ZEUS Luminosities.

4.3 The Zeus Experiment

The ZEUS detector is located in the south hall of HERA and its primary goals are to determine with high precision the energies, directions and nature of single particles and particle jets created in the interactions [19]. The layout of the ZEUS experiment is shown in Figure 16. The heart of the ZEUS detector is the uranium scintillator calorimeter (CAL) [20] which measures energies and directions of particles and particle jets with high precision. This calorimeter hermetically encloses a central drift chamber (CTD) [21] which measures the tracks of charged particles.

This chamber is surrounded by a thin superconducting solenoid producing a magnetic field of 1.43 Tesla for determining the momenta of charged particles from track curvature. The influence of the magnetic field of the thin solenoid on the HERA beam dynamics is compensated by a superconducting solenoid (compensator) creating a field of 5 Tesla.

An iron wall equipped with two layers of scintillation counters (VETOWALL) is placed near the tunnel exit in order to detect the background particles that are produced upstream by the proton beam.

4.3.1 The Uranium Calorimeter

Calorimeters are an important class of particle detectors used for measuring the energy and position of a particle by its total absorption. The central idea is that the primary particles incident on the calorimeter are completely absorbed and the absorbed energy is converted into a measurable signal, which is proportional to the energy of the incident particle.

The primary particles entering the calorimeter interact with the materials making up the detector, producing secondary particles which in turn interact with the

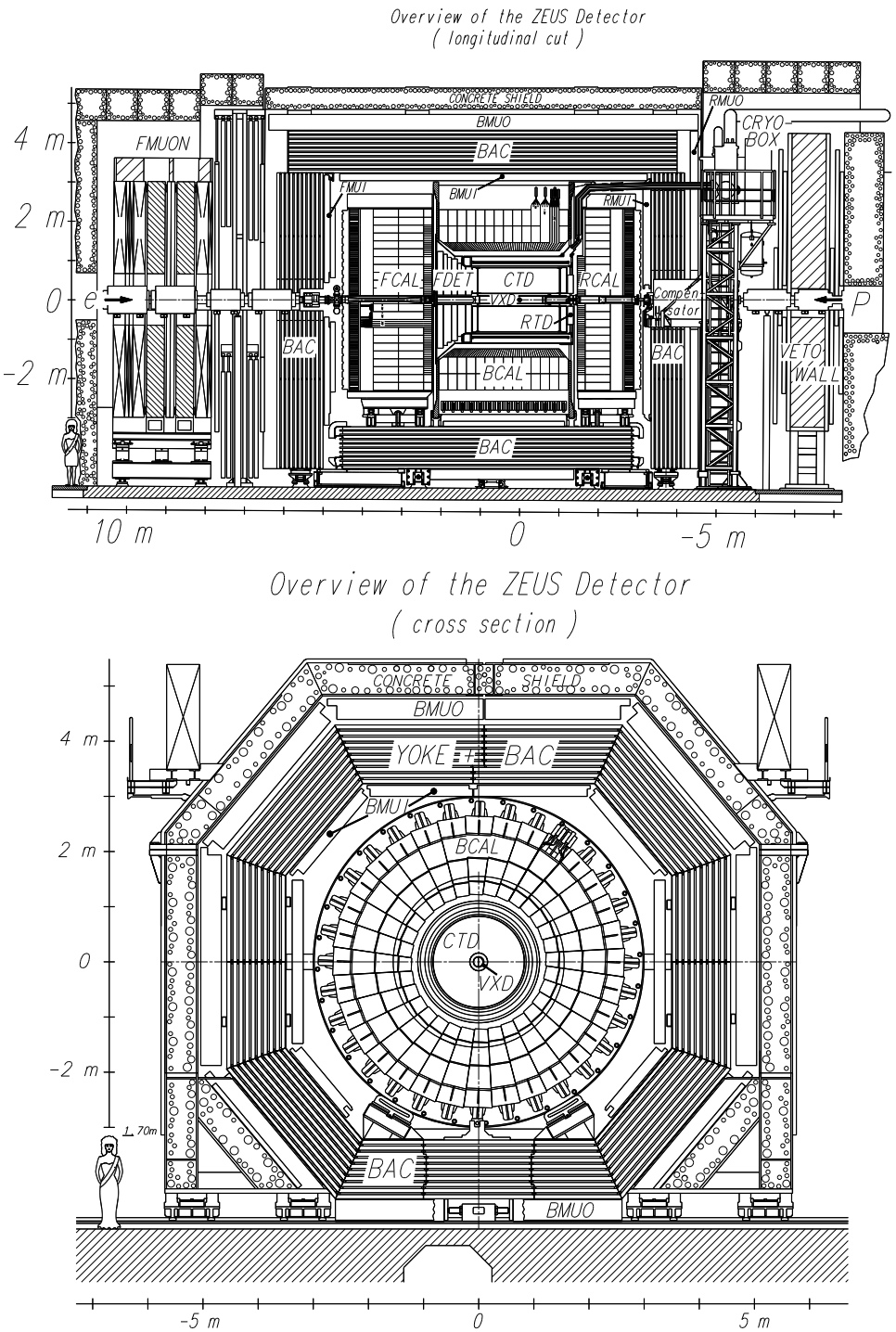

Figure 16: Longitudinal and transverse projection of the ZEUS detector.

material giving more particles. This leads to development of a particle shower or cascade, in which part of it is detected. Two types of showers can be distinguished, electromagnetic and hadronic. Electromagnetic showers interact only electromagnetically and are made up photons, electrons, and positrons, whereas hadronic showers are developed by hadrons such as pions subject to the strong interactions.

The ZEUS depleted-uranium scintillator calorimeter has an energy resolution of

$$\frac{\sigma_E}{E} = \frac{18\%}{\sqrt{E}} \oplus 1\%,$$

for electrons and

$$\frac{\sigma_E}{E} = \frac{35\%}{\sqrt{E}} \oplus 2\%$$

for hadrons[6], where E is in GeV [19]. It covers the polar angle range $2.2^o < \theta < 176.5^o$. The basic structure of the calorimeter is plates of depleted uranium[7], clad in stainless steel foil, interleaved with plastic scintillator tiles (SCSN-38). Each layer is approximately one radiation length (1 X_0) thick.

Through the production of π^0s which decay into two photons, hadronic showers also contain an electromagnetic component. A larger amount of the hadronic cascade energy is lost in intranuclear inelastic collisions and nuclear binding energy. This causes the electromagnetic part of the hadronic shower to yield larger signals than the pure hadronic part, resulting in a larger spread in the global measured response. Compensation can be achieved by increasing the response of the calorimeter to hadronic showers using plates of depleted uranium interleaved with scintillator tiles. Using hydrogenous materials in scintillators much of this lost energy will be recovered. The spallation neutrons from the nuclear breakup transfer a large fraction of their kinetic energy to the hydrogen nucleus, producing recoil protons. These low energy protons have very short range and they deposit

[6]The term $\oplus$ means that the error is added in quadrature.

[7]An alloy of 98.4% ^{238}U, 1.4% Nb, and $\leq$ 0.2% ^{235}U.

their energy in the scintillators. The thickness ratio of 3.3 mm uranium to 2.6 mm scintillator is chosen to give the correct relative signal for the charged particle component compared with the neutron component so that the response to electrons and hadrons is the same [22].

The calorimeter is divided into a forward, a barrel, and a rear part with 7, 5 and 4 interaction lengths (λ), respectively. The forward (FCAL), barrel (BCAL), and rear (RCAL) sections cover polar angles $2.2^o < \theta < 39.9^o$, $36.7^o < \theta < 129.1^o$, and $128.1^o < \theta < 176.5^o$, respectively.

The scintillator tiles form a tower which is read out on both sides by wavelength shifter bars (WLS). A tower is longitudinally segmented into an electromagnetic subtower (EMC) of 1λ ($25\ X_o$) and two (one for the rear section) hadronic subtowers (HAC1 and HAC2) of 3λ each (2λ for the barrel section). The divisions between the EMC and HAC sections greatly help in distinguishing between the electromagnetic showers and hadronic showers, because the incident electrons and photons deposit almost all their energy in the EMC sections, whereas hadrons deposit a substantial fraction in the HAC section.

Each subtower is called a cell and is read out by two photomultiplier tubes (PMT's), one on either side. The calorimeter is segmented into a total of of 5918 cells. The typical transverse dimensions of a HAC is 20 cm $\times$ 20 cm. EMC's are further segmented to 5 cm $\times$ 20 cm in the towers in the forward and barrel sections, and to 10 cm $\times$ 20 cm in the rear section. Towers make up modules, and modules are stacked to make up the calorimeter. Figure 17 shows a cut-away view of a ZEUS FCAL module, showing alternating layers of depleted uranium and scintillator strips, wavelength shifters, and photomultipliers.

The calorimeter also provides timing information. The timing resolution is below 1 ns for energy deposits greater than 4.5 GeV. The calorimeter timing for a given calorimeter module is calculated by averaging the times measured by all

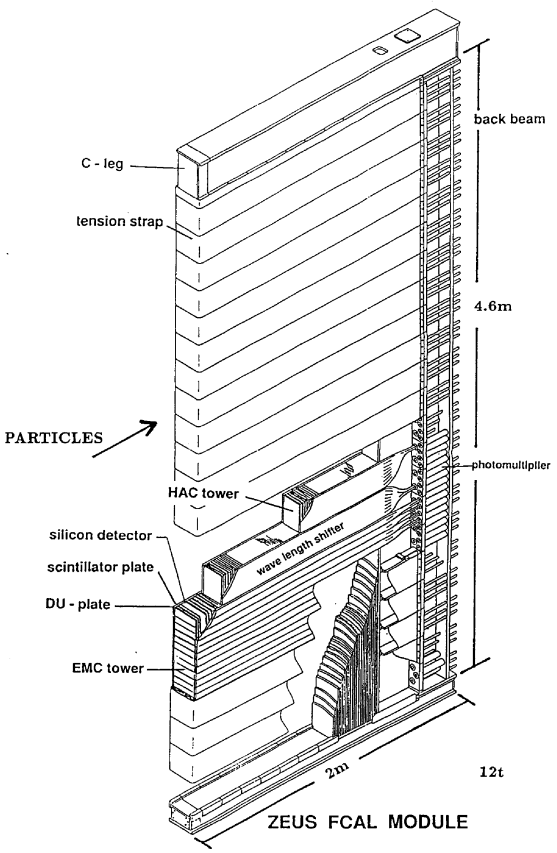

Figure 17: A cut-away view of a ZEUS FCAL module, showing alternating layers of depleted uranium and scintillator strips, wavelength shifters, and photomultipliers.

PMTs belonging to it, with energies exceeding the threshold of 200 MeV.

4.3.2 Central Tracking Detector

The central tracking detector consists of a cylindrical jet type drift chamber with an outer radius of 85 cm and an overall length of 240 cm covering the polar angle region $15^o < \theta < 164^o$ [21]. Its total material thickness was minimized to be about 0.9 X_o (equivalent to 8 cm of aluminum). Track position and dE/dx

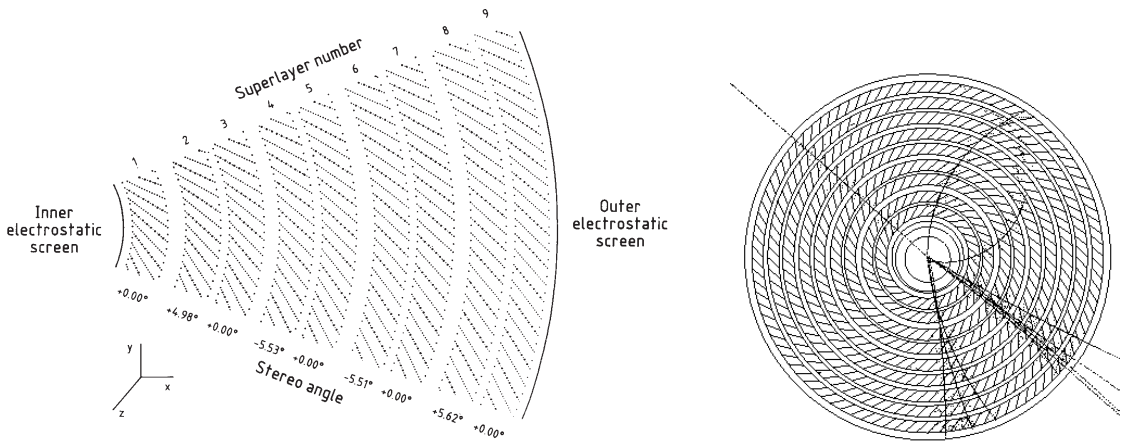

(a) (b)

Figure 18: (a) Cross-section (octant) of the CTD. (b) A transverse cut through the CTD. The solid lines indicate the trajectories of charged particles.

losses are measured in nine superlayers each with eight layers of sense wires. The structure is shown in Figure 18.

The transverse momentum resolution is

$$\frac{\sigma(p_t)}{p_t} = 0.005 p_t \oplus 0.016$$

(p_t in GeV/c). For full length tracks with momenta $p_t > 5$ GeV/c, the vertex resolution is 0.1 cm in the transverse plane and 0.4 cm along the Z axis.

4.3.3 Luminosity Monitor

The luminosity was obtained from the rate of bremsstrahlung, $ep \to ep\gamma$, for which the cross-section is well known. It is based on the coincidence measurement of the electron and the photon in the luminosity monitor (LUMI). The photons are detected in a lead-scintillator calorimeter placed 107 m from the interaction point [23]. The electron detector is positioned at a distance of 35 m from the interaction point.

The cross-section for bremsstrahlung can be calculated using the Bethe-Heitler approximation [24]. The luminosity is obtained from the LUMI counting rate N_{LUMI} with

$$\mathcal{L} = \frac{N_{LUMI}}{\sigma_{BH} \cdot \epsilon_{LUMI}},$$

where σ_{BH} is the theoretical Bethe-Heitler cross-section and ϵ_{LUMI} is the expermentally measured acceptance.

4.4 Trigger and Data Acquisition

The ZEUS experiment employs a three level trigger [25] and a readout system designed to select ep physics events with high efficiency, while rejecting backgrounds caused by proton and electron beam-gas interaction, cosmic rays, and detector noise. It was designed to deal with the 96 ns intervals between bunch crossings and the high rate of background. Each trigger level uses the information available to decide quickly whether to keep or discard the event.

To accommodate the short (96 ns) interval between HERA bunch crossings, the trigger and readout are pipelined, accepting new event information at each 96 ns interval and storing it for 5 μs while a trigger decision is being made. Event information such as energy sums or rudimentary tracking, is fully read out only upon a First Level Trigger (FLT) accept, minimizing deadtime due to readout latency. The first level trigger accepts data at a rate of up to 1 kHz. The FLT has an output rate of a few hundred Hz which is sent to the component readout system and the Second Level Trigger (SLT).

The SLT reduces the data rate by roughly a factor of ten. The SLT has enough time to calculate quantities such as calorimeter energy and timing. After removing events which fail vetos based on calorimeter timing and energy, simple filters are applied to select events which should be passed to the next stage. If the SLT

accepts an event, the Event Builder collects and organizes all the data from the components before sending the complete event information to the Third Level Trigger (TLT). The SLT reduces the event rate to less than 100 Hz.

The TLT runs a version of the offline reconstruction code and processes events using data from all the components. It uses calorimeter timing and track reconstruction to reject much of the remaining non-colliding beam background. Fast algorithms perform an almost full reconstruction to provide input for various physics filters which classify and select appropriate events. The result of a specific trigger algorithm (YES or NO) is recorded as a trigger bit located in a data table.

During the process of reconstruction, filters are applied to the data and pass the accepted events to the Data Summary Tapes (DST). These forms of filter bits called DST-bits are assigned that could be useful in the further offline analyses. In addition, the entire year's data sample is stored in mini-DST format for fast access. These mini-DSTs contain in compressed form all the information needed for most analyses.

Chapter 5

Monte Carlo Simulation

Monte Carlo programs indicate what should happen in an interaction and how it will be measured in the experimental device. A Monte Carlo simulation of excited fermion production and decay is necessary to calculate the efficiency of our selection criteria.

Figure 19 gives a schematic picture of Monte Carlo event generation in ep processes. The central part of the event generation consists of the simulation of the hard scattering process, where partons a and b scatter and produce partons c and d. After the hard scattering, the final partons c and d, as well as the electron and proton remnants, must fragment and decay in order to produce the stable final state particles.

5.1 The e^*/ν^* Event Generator

The excited fermion event generator HEXF V4.0 [26] is a program that is designed to produce excited fermion Monte Carlo events in ep collision at HERA. This generator is based on the model specified in Section 2.1 and is used to generate signal Monte Carlo events.

The structure function of the elastic region is described by electric and magnetic form factors and that of the quasi-elastic region is described by a phenomenological

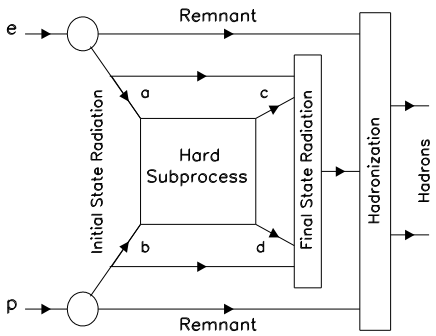

Figure 19: Schematic model of ep interactions.

parameterization from Brasse *et al.* [27]. The deep inelastic region is described by the structure functions MRSA from the PYSTFU [28] library. In order to study the efficiency of ZEUS, parameters in the excited lepton production must be chosen in a specific way. For e^* production, we have adopted the convention $f = f'$ in the Lagrangian given by Eq. (2), while we chose $f = -f'$ for ν^* production. About 42 selected excited electron mass points were also generated for 1996/97 (e^*) and 1998/99 (ν^*) to study the efficiency, see Table 3.

Table 3 Signal Monte Carlo samples used in this analysis.

Channel	e^*/ν^* Mass (GeV)	Year	# Events
$e^* \to e\gamma$	100, 125, 150, 175, 200, 225, 250	1997	3000/mass
$e^* \to eZ \to eq\bar{q}$	110, 125, 150, 175, 200, 225, 250	1997	3000/mass
$e^* \to eZ \to e\nu\bar{\nu}$	110, 125, 150, 175, 200, 225, 250	1997	3000/mass
$e^* \to \nu W \to \nu q\bar{q}'$	100, 125, 150, 175, 200, 225, 250	1997	3000/mass
$e^* \to \nu W \to \nu\bar{\nu}e$	100, 125, 150, 175, 200, 225, 250	1997	3000/mass
$\nu^* \to \nu\gamma$	100, 125, 150, 175, 200, 225, 250	1999	2000/mass

The effects of initial state radiation from the incident electron is taken into

account in the Wiezsäcker-Williams framework [29]. In this approximation, the dominant contribution to radiative corrections is assumed to come from the emission of a photon collinear with respect to the electron. The hadronic final state is simulated using the matrix element and parton shower (MEPS) approach of LEPTO 6.1 [29] for the QCD cascade, and JETSET 7.4 [30] for the hadronization.

5.2 Background Simulation

The Monte Carlo samples used for background estimates are listed in Table 4, which lists the generator cuts applied, the cross-section, the total number of events, and the corresponding integrated luminosity.

5.2.1 NC/CC Simulation

DJANGO 6.24 [32] with the CTEQ 4D structure function is used to simulate the backgrounds from NC DIS and CC DIS. The hadronic final state is simulated using the Color-Dipole Model as implemented in ARIADNE [33] for the QCD cascade.

A second NC and CC DIS sample was used to study the uncertainty of estimating the background. In this set of Monte Carlo events, the hadronic final state is simulated using the matrix element and parton shower (MEPS) approach for the QCD cascade, see Table 5.

5.2.2 QED-Compton Simulation

Backgrounds from elastic and quasi-elastic QED-Compton scattering are simulated using COMPTON 2.0 [34]. However, this generator does not simulate the hadronic system. Therefore, DJANGO is used to simulate the backgrounds from

inelastic QED-Compton scattering. There is an overlap region between the generated Django (NC) events and the Compton 2.0 events in the case of DIS. In Django there is a cut on the mass of the hadronic system (5 GeV). So to exclude the overlap region between Django and COMPTON 2.0, we took only events with hadronic mass less than 5 GeV in COMPTON 2.0 events.

5.2.3 Photoproduction Simulation

Resolved and direct photoproduction backgrounds are simulated with the HERWIG generator [35]. HERWIG is a general purpose event generator, where QCD corrections for the lepton-hadron mode are performed by either parton shower or $\mathcal{O}(\alpha_s)$ QCD matrix element. The events were generated with a standard cut of $Q^2 < 4$ GeV^2 and a minimum transverse momentum of the two outgoing partons from the hard scattering $p_t > 8$ GeV. Events generated with these cuts are then selected by requiring that the generator-level total transverse energy $E_t > 28$ GeV.

5.2.4 W-production Simulation

The production of vector bosons ($ep \rightarrow eW^{\pm}X$) is simulated using EPVEC generator [18]. Hadronization is simulated with JETSET. The cross-section was calculated by dividing the phase space into two regions, DIS and resolved photon.

Table 4. Background Monte Carlo samples used in this analysis.

Generator	Generator Cuts	# Events	Luminosity
$e^+p \quad (\sqrt{s} = 300\,\text{GeV})$			
NC DIS (DJANGO)	$Q^2 > 40$ GeV^2	140 K	5.7 pb^{-1}
	$Q^2 > 100$ GeV^2	140 K	18.5 pb^{-1}
	$Q^2 > 400$ GeV^2	200 K	185 pb^{-1}
	$Q^2 > 1250$ GeV^2	25 K	136 pb^{-1}
	$Q^2 > 5000$ GeV^2	12 K	900 pb^{-1}
	$Q^2 > 10000$ GeV^2	12 K	5042 pb^{-1}
CC DIS (DJANGO)	$Q^2 > 10$ GeV^2	25 K	602 pb^{-1}
	$Q^2 > 5000$ GeV^2	15 K	5914 pb^{-1}
	$Q^2 > 10000$ GeV^2	5 K	10423 pb^{-1}
W Production (EPVEC)	W^- (dis)	20 K	61800 pb^{-1}
	W^+ (dis)	20 K	51100 pb^{-1}
	W^- (res. photon)	20 K	200000 pb^{-1}
	W^+ (res. photon)	20 K	158000 pb^{-1}
PHP (HERWIG 5.8)	(dir) $P_t^{hard} > 8$ GeV, $E_t > 28$ GeV	230 K	113 pb^{-1}
	(res) $P_t^{hard} > 8$ GeV, $E_t > 28$ GeV	245 K	35pb^{-1}
QED-Compton	(elastic+quasi.) $20 < M_{e\gamma} \leq 50$ GeV	230 K	113 pb^{-1}
	(elastic+quasi.) $50 < M_{e\gamma} \leq 100$ GeV	245 K	35 pb^{-1}
	(elastic+quasi.) $M_{e\gamma} > 100$ GeV	245 K	35 pb^{-1}
$e^-p \quad (\sqrt{s} = 318\,\text{GeV})$			
NC DIS (DJANGO)	$Q^2 >$100 GeV^2	200 K	24 pb^{-1}
	$Q^2 > 400$ GeV^2	200 K	17 pb^{-1}
	$Q^2 > 1250$ GeV^2	20 K	92 pb^{-1}
	$Q^2 > 5000$ GeV^2	20 K	457.5 pb^{-1}
	$Q^2 > 20000$ GeV^2	10 K	11539 pb^{-1}
CC DIS (DJANGO)	$Q^2 > 10$ GeV^2	25 K	314 pb^{-1}
	$Q^2 > 5000$ GeV^2	15 K	1008 pb^{-1}
	$Q^2 > 10000$ GeV^2	5 K	899 pb^{-1}

5.3 Detector Simulation

MOZART is a GEANT [36] based package through which all simulated events are passed. It simulates the passage of particles through the components of the detector accounting for the physics processes such as particle decay and interaction, energy loss in dead materials[8], multiple scattering, etc. The triggers were simulated by the ZGANA [37] package. Having passed all the detector and trigger requirements, the events are reconstructed.

Table 5. MEPS set of background Monte Carlo samples used in this analysis.

Generator	**Generator Cuts**	**# Events**	**Luminosity**
$e^+p \quad (\sqrt{s} = 300\,\text{GeV})$			
NC DIS (MEPS)	$Q^2 > 400$ GeV^2	27 K	24.9 pb^{-1}
	$Q^2 > 1250$ GeV^2	25 K	136 pb^{-1}
	$Q^2 > 5000$ GeV^2	12 K	917 pb^{-1}
	$Q^2 > 10000$ GeV^2	12 K	5050 pb^{-1}
CC DIS (MEPS)	$Q^2 > 10$ GeV^2	20 K	488 pb^{-1}
	$Q^2 > 5000$ GeV^2	14.5 K	5718 pb^{-1}
	$Q^2 > 10000$ GeV^2	5 K	9839.5 pb^{-1}
$e^-p \quad (\sqrt{s} = 318\,\text{GeV})$			
CC DIS (MEPS)	$Q^2 > 10$ GeV^2	20 K	488 pb^{-1}
	$Q^2 > 5000$ GeV^2	14.5 K	5718 pb^{-1}
	$Q^2 > 10000$ GeV^2	5 K	9839.5 pb^{-1}

[8]Tracking chambers, a magnetic coil and various mechanical constructions are installed in front of the calorimeter. These materials degrade the measured signal and the energy resolution of the calorimeter and are called dead materials.

Chapter 6

Event Reconstruction

In this chapter we discuss the event reconstruction and present the kinematic variables relevant to this analysis.

6.1 Track Reconstruction and Vertex finding

The VCTRAK [39] package reconstructs particle trajectories in the tracking detectors. VCTRAK uses data from the CTD, and starts tracking from a seed in the outer layer. These are followed inward to the origin at $x = y = 0$. A seed consists of three CTD hits from a superlayer. A fourth, virtual, hit is added at the beam line in order to guide the hit inwards. The track candidate is extrapolated inward, gathering additional hits with increasing precision.

To reconstruct the primary event vertex, tracks incompatible with the beam line are removed and with a simple vertex fit, the (x, y, z) of the remaining tracks are calculated. Finally with full vertex fitting procedure, an adjustment between the direction and curvature of tracks and the final vertex position is made.

In ZEUS, a small portion of excited electron or neutrino events consist of a final state in which the energy is deposited close to the forward beam hole. This is the case for high mass excited electrons decaying into a photon and an electron, or $e^* \rightarrow eZ \rightarrow e\nu\bar{\nu}$ and $e^* \rightarrow \nu W \rightarrow \nu\bar{\nu}e$. In such events the particles fall

outside the angular region that is covered by the CTD, and the events will lack a reconstructed vertex. In this analysis this type of event is cut out by a vertex requirement which leads to a reduction of overall efficiencies of $e^* \rightarrow e\,\gamma$ and $\nu^* \rightarrow \nu\,\gamma$ signal Monte Carlo events by less than 1%, while decreasing the overall efficiency of $e^* \rightarrow \nu W \rightarrow \nu\bar{\nu}e$ decay mode by 7%.

6.2 The Calorimeter Reconstruction

Measurement of the energy of particles interacting in the uranium calorimeter is based on the proportional relationship between the light seen in the left and right PMTs of each calorimeter cell and the deposited energy. The calibration of this process has been determined from test beams [38].

Every cell consists of two readouts, one each from the left and right sides. In general, in obtaining the energy of the cell, the sum of the two sides will be calculated. However, in conditions where one of the two channels is having a problem due to a readout failure or noise, an estimate of the energy of the cell can be obtained by using the good channel and multiplying by 2. This redundancy ensures the robustness of the calorimeter data acquisition. It is important to note that the calorimeter must be hermetic to see missing momentum. If both channels in a cell are effectively bad, there is a "hole" in the calorimeter. During 1996-97 running period the fraction of the holes in the calorimeter was on average around 0.01% and during 1998-99 was no more than 0.05%.

Offline corrections are applied to the calculated energy, including detector effects from cracks and spaces, and PMT gain corrections.

6.3 Clustering of Energy Deposits

We define islands as the objects in which the calorimeter cells with non-zero

energy deposits are grouped. Islands correspond to single particles entering the calorimeter. If a cell has sufficient energy, it becomes a candidate to be connected with one of its neighbors. The connections are made to the highest energy nearest neighbor. This procedure is repeated for all cells. The merging is done separately in each calorimeter section and also separately for FCAL, BCAL, and RCAL.

The spatial separation between calorimeters introduces a complication for clustering algorithms in handling the energy deposits of a single particle which is not confined to one calorimeter section, since the energy will be split into more than two clusters. A further algorithm based on the opening angles between clusters is used to perform a final merge of islands, which properly handles the boundaries between calorimeters [40]. Figure 20 shows the schematic representation of the cell island clustering.

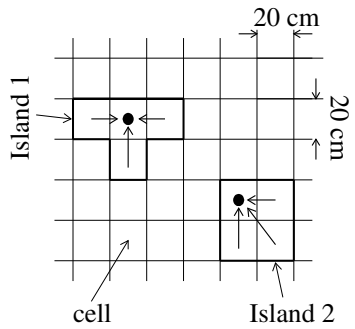

Figure 20: Schematic representation of the cell island clustering. The dots denote towers which are island seeds. The trail of pointers to the neighboring tower with the most energy is shown by the thick black arrows. The thick black lines delimit the boundary of an island.

6.4 Kinematic Variables

In this section we present the global event quantities used for event selection in the excited electron and neutrino search.

The longitudinal energy variable, $E - P_z$, is defined as

$$E - P_z = \sum_i (E_i - p_{zi}) \tag{16}$$

where

$$E_i = \sqrt{p_{xi}^2 + p_{yi}^2 + p_{zi}^2}$$

is the energy in the ith calorimeter cell (above a set threshold). As we mentioned in Chapter 3, when only particles in the proton direction remain undetected, this variable is expected to reach values close to double the electron beam energy (55 GeV) for NC DIS type events or below this quantity for CC DIS and photoproduction events.

The absolute value of the vector sum of the transverse energy of the calorimeter cells is referred to p_t^{miss} (so-called missing transverse momentum),

$$P_t^{miss} = \sqrt{(\sum_i P_{xi})^2 + (\sum_i P_{yi})^2} \tag{17}$$

We also define

$$P_t^{miss}(\theta > 10^o) = \sqrt{(\sum_i^{\theta>10^o} P_{xi})^2 + (\sum_i^{\theta>10^o} P_{yi})^2} \tag{18}$$

where the FCAL cells in the forward cone $\theta < 10^o$ are excluded. The sensitivity to particles within the proton remnant will be reduced this way as well.

The scalar sum of the transverse energy deposited in the calorimeter is denoted by

$$E_t = \sum_i \sqrt{P_{xi}^2 + P_{yi}^2} \tag{19}$$

where sum runs over all calorimeter cells above a set threshold.

The quantity

$$E_t^{had} = \sum_i^{had} \sqrt{P_{xi}^2 + P_{yi}^2} \tag{20}$$

is the transverse energy associated only with the hadronic state where the sum with superscript had excludes the FCAL cells in the forward cone $\theta < 10^o$ and cells in the calorimeter sum, and the cells belong to clusters which are identified as candidate electrons or photons.

The total effective mass measured by the calorimeter is denoted by

$$M^{Total} = \sqrt{(\sum_i^{\theta>10^o} E_i)^2 - (\sum_i^{\theta>10^o} P_{xi})^2 - (\sum_i^{\theta>10^o} P_{yi})^2 - (\sum_i^{\theta>10^o} P_{zi})^2} \qquad (21)$$

where the sum excludes the FCAL cells in the forward cone $\theta < 10^o$. Finally we denote the hadronic mass as

$$M^{had} = \sqrt{(\sum_i^{had} E_i)^2 - (\sum_i^{had} P_{xi})^2 - (\sum_i^{had} P_{yi})^2 - (\sum_i^{had} P_{zi})^2}. \qquad (22)$$

The final state which results from the interaction may or may not contain an electron or photon in the main calorimeter. When the final state does have electromagnetic showers, the polar angle and the energy of the showers are denoted by θ_{EMi} and E_{EMi} respectively ($i = 1, 2, ...$).

6.5 Electromagnetic Cluster Identification

In this analysis, the identification of electromagnetic clusters is done by using the EM electron finder, which is a neural network based algorithm for identifying electromagnetic clusters [41]. It is based on probability distributions for relevant detector quantities such as the fraction of energy in the HAC layers, the fraction of energy in a module, the highest energy module, and the detailed parameterizations of the detector response for electrons.

In this analysis an island is accepted as a candidate if the energy of the island exceeds 4 GeV and its probability exceeds 0.001. The probability requirement is raised to 0.01 for electromagnetic clusters with polar angle less than 0.3 rad. The last condition suppresses the number of fake electromagnetic candidates from high

energy $\pi^0 \to \gamma\gamma$ decays in a jet, populated in the forward direction, see Figure 21(c).

For events passing the above selection criteria, the efficiency of the EM electron finder is above 95%. It suffers from small efficiency losses at the F/BCAL and B/RCAL gaps [42, 43] as shown in Figure 22.

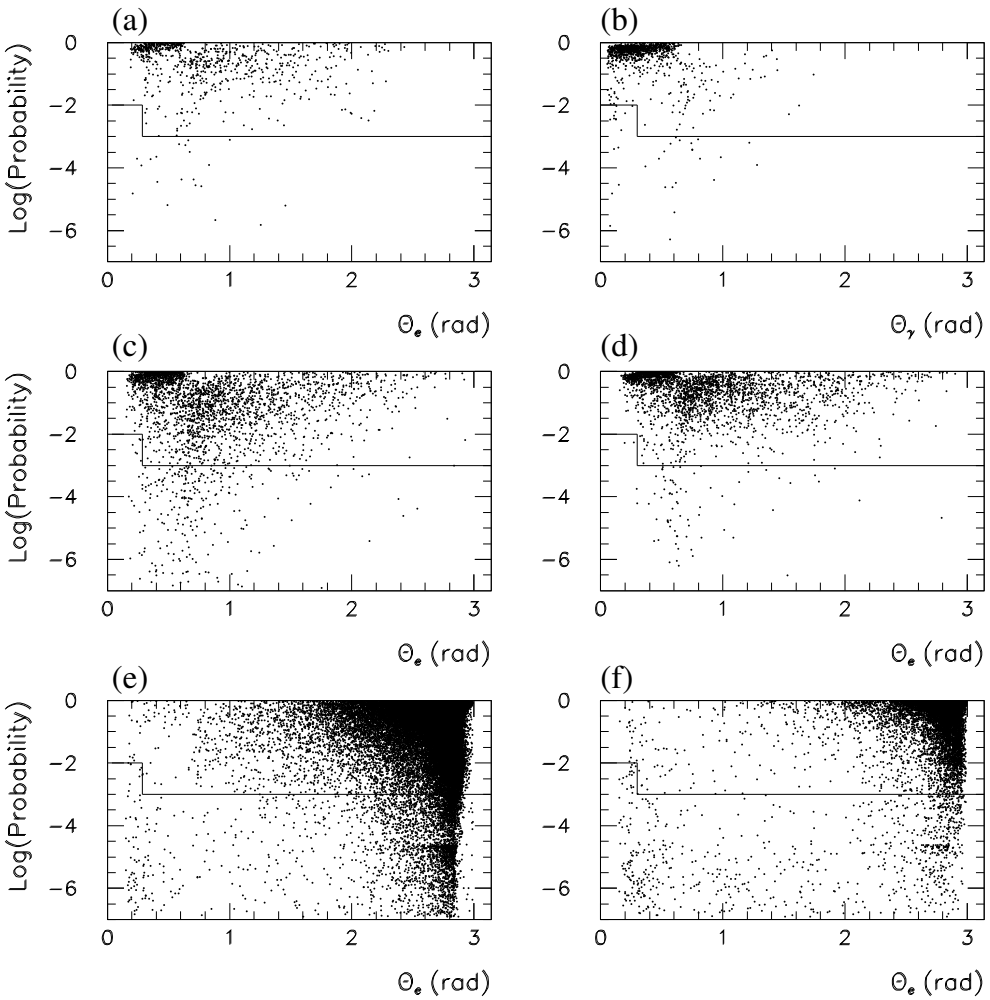

Figure 21: Distribution of the probability versus the polar angle of the electromagnetic cluster for (a) 225 GeV $e^* \to e\gamma$ (the final electron), (b) 225 GeV $e^* \to e\gamma$ (the final photon), (c) 225 GeV $e^* \to eZ \to eq\bar{q}$, (d) 225 GeV $e^* \to eZ \to e\nu\bar{\nu}$, (e) NC DIS Monte Carlo, and (f) data.

6.5.1 Electron Energy Corrections

A dead material correction is applied to the energy of the electromagnetic clusters in the BCAL or the FCAL, using the 1996/97 dead material map in combination with a non-uniformity correction [44]. The basis of this correction is a map of non-active material in front of the calorimeter. Figure 23 shows the mean difference between the true and reconstructed corrected (solid histogram) and uncorrected (dotted histogram) electron energy, and between the true and reconstructed corrected polar angle of the electron for NC DIS Monte Carlo.

6.5.2 Track Matching Requirements

A matching CTD track is the major requirement for an electromagnetic cluster to be considered as an electron candidate. Electrons with polar angle greater than 0.3 rad are required to have a track with a momentum greater than 5 GeV that extrapolates to within 10 cm of the electron. The distribution of the momenta of the tracks ($P_{t,EM}^{Trk}$) is plotted for excited electron, data, and NC DIS Monte Carlo events in Figure 24. To do so we required one isolated (see the following section) electron with transverse energy greater than 10 GeV, a polar angle less than 2.5 rad, and 35 GeV $< E - P_z <$ 65 GeV. In order to avoid missing many excited electron candidate events, electrons with polar angle less than 0.3 rad do not have to have a track.

On the other hand, the single important requirement in the selection of photons is that there is no track matching the electromagnetic cluster within some distance of closest approach.

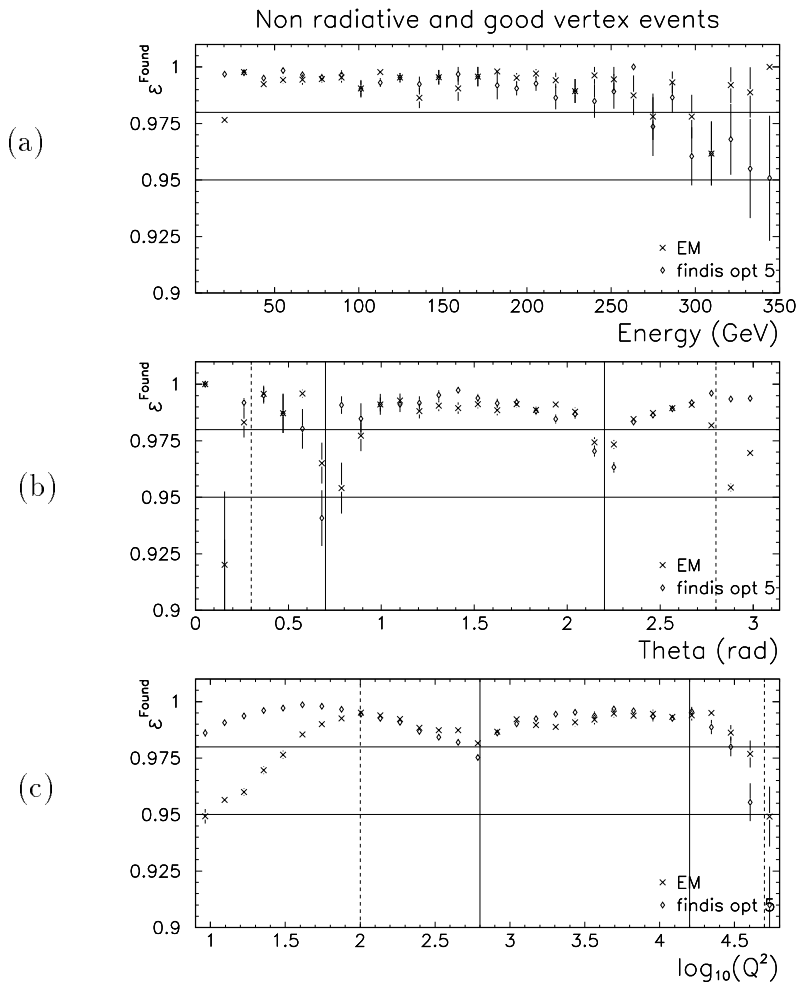

Figure 22: The efficiency (ϵ^{Found}) of EM and Sinistra (Sira 5) electron finders versus (a) the energy, (b) the polar angle of the electron found, and (c) Q^2 [42]. Horizontal lines represent 2% loss (upper line) and 5% loss (lower line), vertical full lines indicate calorimeter limits and vertical dashed lines represent CTD end.

6.5.3 Electron Isolation Requirements

Electron isolation is a major precautionary action that is taken in order to avoid electron misidentification due to photons in the hadron jet. Furthermore, in order to reduce the fake electron background the candidate electrons should be

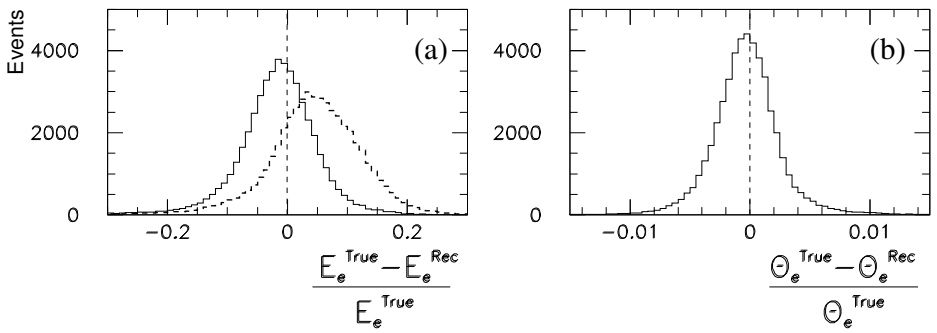

Figure 23: The mean difference between the true and reconstruction corrected (solid histogram) and uncorrected (dashed histogram) (a) electron energy, and (b) the polar angle of the electron for NC DIS Monte Carlo.

well isolated from other activity in the event.

The measure used is the isolation energy, defined as

$$E_{EM}^{iso} = \sum_i E_{non-electron}^i$$

where the summation extends over all calorimeter cells not assigned by the EM electron finder to the electromagnetic cluster that lie with an (η, ϕ) cone of radius

$$R = \sqrt{(\Delta\eta)^2 + (\Delta\phi)^2}$$

centered about the electron direction.[9]

It has been found that $R = 0.8$ units allows an effective separation of isolated and non-isolated electrons. In fact, excited lepton events with an electron in their final state contain very little non-electron energy. Therefore, $E_{EM}^{iso}(R < 0.8) <$ 2 GeV is used. This rejects fewer excited lepton events while removing many fake ones from background, Figure 25.

In the case where an excited electron decays into an electron and two jets, $e^* \to eZ \to eq\bar{q}$ the electron isolation cut may not be applied, because here the electron may be in close proximity to one of the jets, see Figure 25(d).

[9]The pseudorapidity, is defined as $\eta = \ln(\tan\frac{\theta}{2})$ where θ is the polar angle.

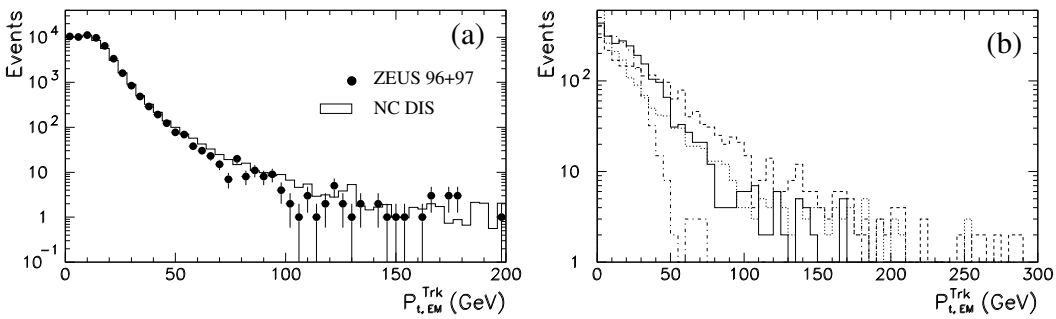

Figure 24: The distribution of the track momenta ($P_{t,EM}^{Trk}$) for (a) data (solid black point) and NC DIS (open histogram) Monte Carlo, and for (b) 125 GeV (solid line) and 225 GeV (dotted line) $e^* \to \nu W \to \nu\bar{\nu}e$, 125 GeV (dash-dotted line) and 225 GeV dashed line) $e^* \to eZ \to eq\bar{q}$ Monte Carlo. The $P_{t,EM}^{Trk}$ distributions for $e^* \to eZ \to e\nu\bar{\nu}$ are similar to those for $e^* \to eZ \to eq\bar{q}$.

It is notable to mention that the number of the calorimeter cells making up the electromagnetic cluster is normally less for electrons than for fake electrons. For this reason, an upper limit of 30 is placed on the number of calorimeter cells in order to reject candidates with abnormally large spatial extents.

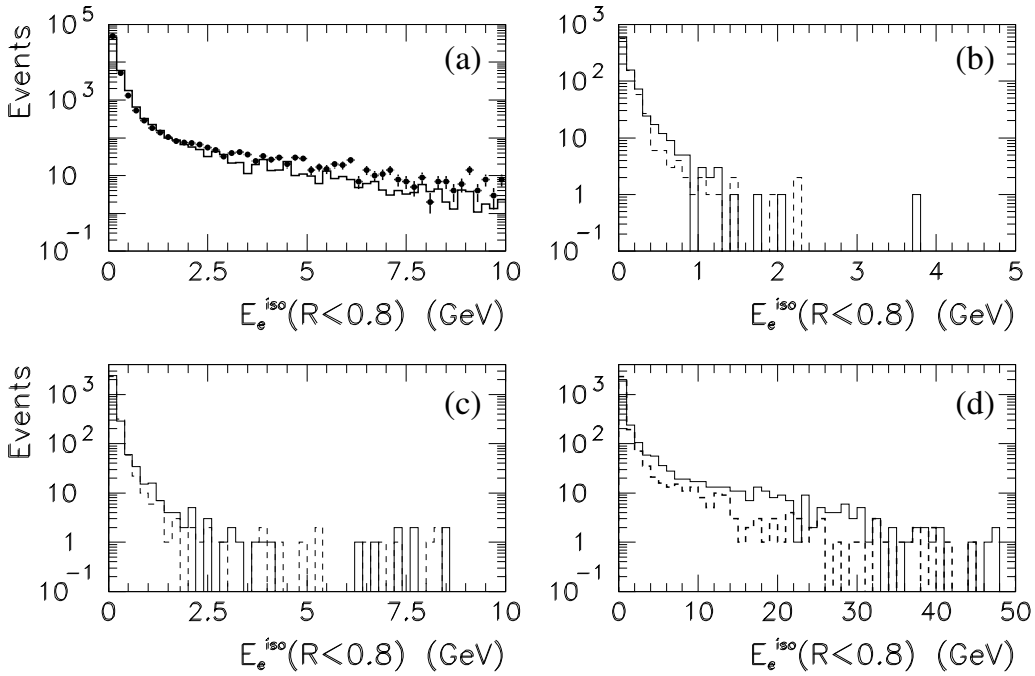

Figure 25: The distribution of the energy in an $\eta - \phi$ cone of radius 0.8 that is not assigned to the electron candidate, $E_e^{iso}(R < 0.8)$, for (a) data (solid black points) and NC DIS (open histogram) Monte Carlo, and for (b) 125 GeV (solid line) and 225 GeV (dashed line) $e^* \to e\gamma$, (c) 125 GeV (solid line) and 225 GeV (dashed line) $e^* \to eZ \to e\nu\bar{\nu}$, (d) 125 GeV (solid line) and 225 GeV (dashed line) $e^* \to eZ \to eq\bar{q}$. The $E_e^{iso}(R < 0.8)$ distributions for $e^* \to \nu W \to \nu\bar{\nu}e$ are similar to those for $e^* \to eZ \to e\nu\bar{\nu}$.

Chapter 7

Data Selection

Among all the events collected during the run, only a subset is relevant to the excited electron or neutrino search. In this analysis, the selection of candidate events for excited lepton decays starts with the experimental trigger, followed by the offline event reconstruction and the final analysis. The first two topics are discussed in this chapter.

Based on the experimental signatures of the final states, we split the data into a sample of events with at least one electromagnetic cluster in their final state and a sample of events without any electromagnetic cluster. In this analysis, the data were subjected to a series of cuts for the purpose of separating excited electron and neutrino candidates from backgrounds.

7.1 Online Event Selection

As was described in Section 4.4, a three-level trigger system is used to collect the data. The transverse energy deposit[10] in the calorimeter and track information from the CTD plays an important role in the efficiency of an event in the FLT.

Timing information is used to reject the background in the SLT. As well, E_t

[10] At FLT the transverse energy refers to the total transverse energy in the whole calorimeter excluding the two inner FCAL rings.

and $E-P_z$ thresholds are applied in the SLT to select high and medium E_t events. The TLT applies stricter timing, cosmic ray and other background rejection cuts than the SLT. Here again, a reconstructed vertex consistent with the ep collisions is used to recalculate the E_t as well as the $E-P_z$ for events.

7.1.1 DST Selection

In this analysis, the following DST bits of the ZEUS Exotics Physics Group are used as a starting point of the offline analysis: NC DIS (DST33), high P_T^{miss} (DST34), high E_t (DST36) events with a good vertex (DST37). The details of the principle cuts for these bits are given in Appendix A.

The DST events are stored on a tape mass storage system and in a reduced format which is later available on hard disks. The following selection have been defined in order to collect high-E_t events with and without electromagnetic cluster events:

(DST33 .or. DST34 .or. DST36) .and. DST37.

We define the efficiency of a selection criteria simply as the ratio of the number of Monte Carlo events passing the selection criteria to the total number of generated events for a specific mass point. Table 6 provides a list of the efficiency with which the excited electron and neutron Monte Carlo events pass the logical combination (DST33 .or. DST34 .or. DST36). The efficiencies for all masses and all decay modes are above 97.5%. As can be seen from Table 6, requiring a good vertex (DST 37) in addition reduces the efficiency of the signal Monte Carlo (see Section 6.1).

In general, the higher the mass of the excited lepton, the less the efficiency. Moreover, the loss of decay products through the forward beam hole increases because the electron or photons are boosted more forward. For a decay containing

a W, if the W partially escapes then the event cannot be triggered. The efficiency for the νW channel is less at all masses due to the escaping neutrino; this is particularly true at high masses where one of the e^* decay products escape through the forward beam hole.

Table 6: The efficiency of the signal Monte Carlo due to trigger effects.

Mode \ F^* Mass (GeV)	**100/110**[†]	**125**	**150**	**200**	**225**	**250**
Trigger Logic (DST33 .or. DST34 .or. DST36)						
$e^* \to e\gamma$	99.5%	99.2%	99.6%	99.9%	99.8%	99.6%
$e^* \to eZ \to eq\bar{q}$	99.4%	99.9%	99.9%	100%	100%	100%
$e^* \to eZ \to e\nu\bar{\nu}$	97.5%	97.9%	99.4%	99.7%	99.8%	99.7%
$e^* \to \nu W \to \nu q\bar{q}'$	99.3%	99.9%	99.9%	100%	100%	100%
$e^* \to \nu W \to \nu\bar{\nu}e$	98.5%	98.3%	98.4%	98.1%	97.5%	97.5%
$\nu^* \to \nu\gamma$	99.7%	99.8%	100%	92.7%	99.8%	99.8%
Trigger Logic (DST33 .or. DST34 .or. DST36) .and. DST37						
$e^* \to e\gamma$	96.7%	97.1%	96.4%	95.7%	94.2%	94.7%
$e^* \to eZ \to eq\bar{q}$	97.6%	98.3%	98.3%	98.1%	98.2%	98.2%
$e^* \to eZ \to e\nu\bar{\nu}$	91.2%	95.1%	95.1%	94.2%	92.7%	93.1%
$e^* \to \nu W \to \nu q\bar{q}'$	97.6%	97.9%	98.3%	97.8%	98.2%	97.9%
$e^* \to \nu W \to \nu\bar{\nu}e$	94.3%	91.6%	89.6%	82.0%	77.3%	72.5%
$\nu^* \to \nu\gamma$	92.4%	93.0%	92.7%	91.3%	90.9%	90.0%

[†] To evaluate the efficiency, we have used signal Monte Carlo events with mass of 100 GeV for $e^* \to e\gamma$, $e^* \to \nu W$, and $\nu^* \to \nu\gamma$ decay modes and 110 GeV for $e^* \to eZ$ decay channels.

7.2 Offline Cuts

The major focus of the first stage of offline analysis is to select e^* and ν^* candidate events with and without electromagnetic clusters while rejecting events which originate from non-ep collisions. Examples of this are interactions of beam

protons with residual gas in the beam pipe (beam-gas events), cosmic rays and halo muons.[11] In addition, events arising from occasional faulty operation of the hardware need to be rejected.

7.2.1 Corrections

Particles originating from the *ep* interaction point traverse different material before reaching the main calorimeter. Depending on the particle types, the measured energy in the calorimeter is reduced as particle lose energy within the material material located in front of it, making correction necessary.

The following corrections are applied to data or Monte Carlo events, after they are selected by the DST bits and before any cuts in this analysis have been applied:

- **Calorimeter Energy Scale Corrections**: A map of dead material in front of the calorimeter was obtained for both Monte Carlo and data using CERN test beam data and events generated by Monte Carlo. The map was generated for electrons shooting at different θ and ϕ angles. Then the energy loss was fitted as a function of the momentum for various thickness of absorber in front of the FCAL prototype [44]. There is a multiplication factor due to non-uniformity and dead material between the actual calorimeter energy scale and that simulated. The corrections applied are +8% and +4% to BHAC and BEMC cell energies respectively, +2.5% to RCAL energies (both EMC and HAC), and +4% for FEMC and -5% for FHAC.

- **Calorimeter Position Correction**: Because of a measured discrepancy between data and Monte Carlo, the cells in the BCAL are shifted in the

[11] Halo muons produced at upstream in the proton beam pipe with the interaction of protons and residual gas in the beam pipe or off orbit protons and the beam pipe.

z-direction by 6.5 mm for data [45]. There is also a z-shift of 1.1 cm in the RCAL [46].

- **Hadronic Final State Correction**: The hadronic correction [47] includes a back-splash (albedo) correction, energy corrections for losses in dead material maps for 96/97[12], and a correction for energy loss in super-cracks between the F/BCAL and R/BCAL parts. The back-splash from the calorimeter and the showering in the material in front of the calorimeter will cause energy deposits far from the true particle direction. These effects cause an additional contribution to $E - P_z$ of the order of 1 GeV.

  The radiation length of the inactive materials plays an important role in determining the losses in inactive material and the correction of the losses before particles reach the calorimeter is done according to the radiation length of the material. By analyzing the ratio of measured to true energy for Monte Carlo events, either as a function of the energy and the amount of inactive material or as function of the energy and the fraction of energy in EMC section, the correction has been made possible [47].

7.2.2 Cleaning Cuts

In order to ensure that the selected events are ep interactions, the following selection cuts, common to all channels, were applied.

- **Data Quality Cut**: The bad runs which had major component problems or caused by unstable HERA beams were rejected. The events in the remaining runs had to have a valid ep bunch crossing.

[12]The dead material is not expected to change between 1996 and 1997.

- **Vertex Cut**: An event vertex measured by the CTD within 50 cm of the nominal collision point along the beam axis is the major requirement for all the selected events. Figure 26 is a good indicator of the vertex distribution along the z-axis before applying this cut. The separation of the events based on their reconstructed vertex selection, removes a large fraction of the cosmic background where muons pass through the calorimeter without entering the inner detector.

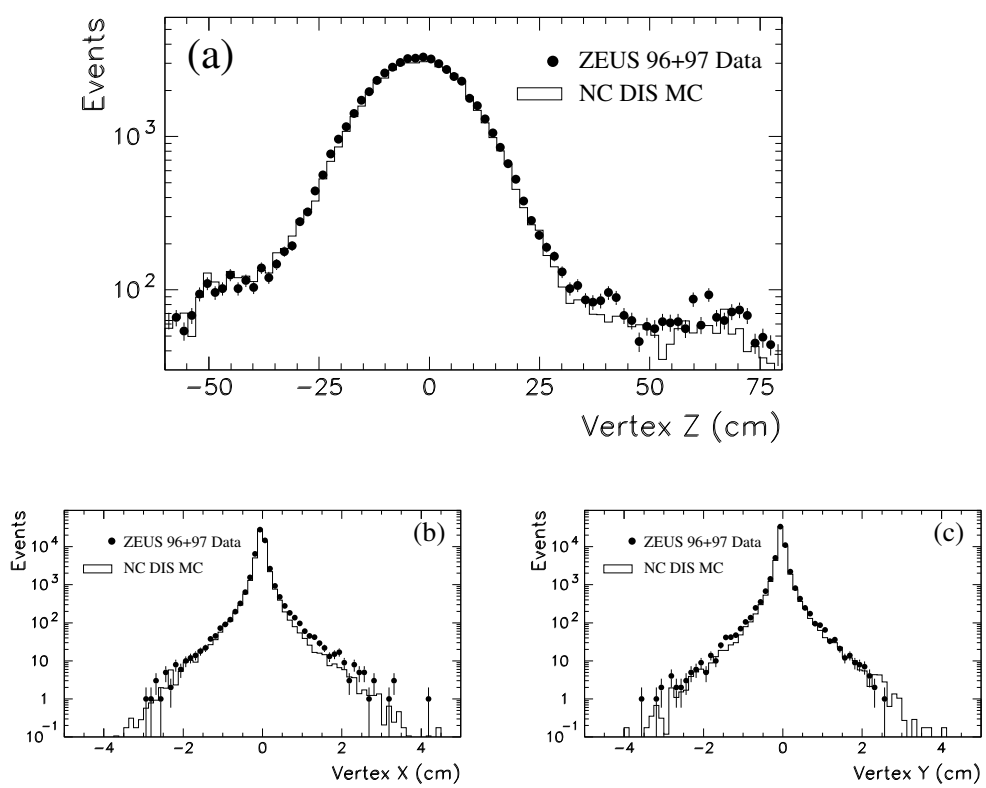

Figure 26: (a) The z-vertex distribution along the beam axis, (b) the x- and (c) y-vertex distributions.

- **Noise Suppression**: Another major problem is the calorimeter cell noise which is primarily created as a result of uranium radioactivity. This noise is

suppressed by a cut at about four times the rms of the noise signal (NOISE 94/96 [48]). This corresponds to a cut of 60 MeV for EMC cells and 110 MeV for HAC cells.

- **Calorimeter Anti-Spark Cut**: Since a calorimeter cell is read out by two PMTs, the detection of signals caused by electronic sparks around PMTs is possible by examining the energy imbalance between[13] them.

  All cells with energy greater than 0.2 GeV and very high energy imbalance (greater than 0.9) are excluded. Also, the candidate electromagnetic shower needs to have more than one calorimeter cell in order to be able to suppress the PMT sparks.

  Any cell with (Energy $\times$ imbalance) $>$ 99.9 GeV is removed.[14] Also any isolated cell with a bad PMT with imbalance equal to zero is rejected.

- **Halo/Cosmic Muon Cut**: Reject if the event has a pattern of energy deposit in the CAL consistent with a cosmic muon or proton beam associated muon.

- **Timing Cut**: The following cuts have been made to reject the beam-gas and cosmic muon events. The event is rejected if the global time calculated by the calorimeter ($|t_g|$) lies outside $\pm$ 6 ns. Here, the time of the event is defined as the energy weighted mean of the times measured by each PMT.

---

[13]The energy imbalance is defined as

$$\left| \frac{E^{\rm PMT}_{\rm Left} - E^{\rm PMT}_{\rm Right}}{E^{\rm PMT}_{\rm Left} + E^{\rm PMT}_{\rm Right}} \right|$$

where $E^{\rm PMT}_{\rm Left}$($E^{\rm PMT}_{\rm Right}$) is the energy of the left (right) PMT.

[14]Since CALTRU table which stores all energy, imbalance, timing and other information for each calorimeter cell, cuts energies at 100 GeV, it is important to impose this condition for each calorimeter cell.

For calculation of an average time, at least two PMTs are required. Furthermore, the total energy of cells that compute the time must be greater than 1 GeV.

The synchronization of PMT times is such that particles moving with the speed of light from the nominal ep crossing reach a given cell at $t = 0$, see Figure 27(a).

To reject beam-gas events, Figure 27(b), which occur outside the calorimeter and strike the RCAL before the nominal ep interaction time, the following cuts are applied:

$$|t_f| < 6 \text{ ns}, \quad |t_r| < 6 \text{ ns}, \quad \text{and} \quad |t_f - t_r| < 6 \text{ ns},$$

where the timings t_f and t_r were calculated for the FCAL and RCAL, respectively.

To reject cosmic rays passing successively through the upper and lower parts of the calorimeter, Figure 27(c), we require

$$|t_b| < 6 \text{ ns} \quad \text{and} \quad |t_u - t_d| < 6 \text{ ns}\,,$$

where the timings t_b, t_d and t_u were calculated for the BCAL, down and up halves of the calorimeter.

Table 7 shows the efficiency of signal Monte Carlo events after cleaning cuts (including the trigger efficiency).

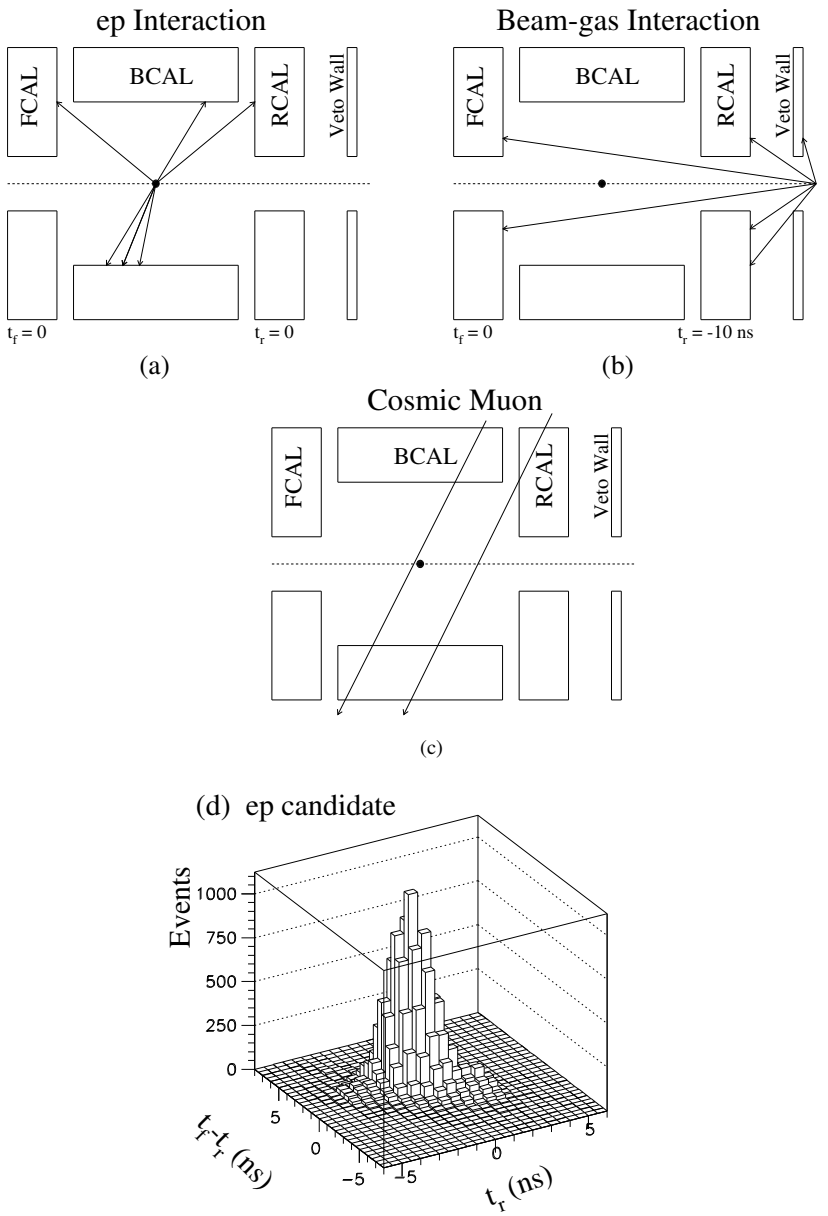

Figure 27: Typical signature of (a) an nominal ep interaction, (b) the beam-gas events, and (c) the cosmic muon. (d) Distribution of the signal time measured in the RCAL (t_r) versus the difference $t_f - t_r$ between the signal times seen in FCAL and RCAL.

Table 7: The efficiency of the signal Monte Carlo after cleaning cuts (including the trigger effects).

Mode \ e^* Mass (GeV)	**100/110**†	**125**	**150**	**200**	**225**	**250**
$e^* \to e\gamma$	93.3%	94.0%	94.0%	92.6%	91.4%	91.8%
$e^* \to eZ \to eq\bar{q}$	83.5%	88.6%	91.0%	92.2%	92.7%	93.2%
$e^* \to eZ \to e\nu\bar{\nu}$	86.3%	91.0%	91.2%	90.2%	88.4%	88.7%
$e^* \to \nu W \to \nu q\bar{q}'$	92.6%	93.2%	93.8%	93.2%	93.1%	93.0%
$e^* \to \nu W \to \nu\bar{\nu}e$	89.1%	87.3%	85.7%	78.4%	73.8%	69.3%

† To evaluate the efficiency, we have used signal Monte Carlo events with mass of 100 GeV for $e^* \to e\gamma$, and $e^* \to \nu W$ decay modes and 110 GeV for $e^* \to eZ$ decay channels.

Chapter 8

e^* Event Samples

The e^+p 1996+97 data corresponds to an integrated luminosity of 38.4 pb^{-1}. After the cleaning cuts described in Chapter 7, the data sample consists of 1,640,798 events. Using further cuts described in this chapter, we select two data samples to use for physics analysis, corresponding to states in which decays of the excited electrons either contain or do not contain an electromagnetic particle (e or γ).

The search for excited electrons is based on these two samples.

8.1 Events with Electromagnetic Cluster

Most of the decay modes of the excited electron contain at least one high transverse energy electromagnetic cluster in the final state,

$$e^* \to e\gamma, \qquad e^* \to eZ \to eq\bar{q}, \qquad e^* \to eZ \to e\nu\bar{\nu}, \qquad e^* \to \nu W \to \nu\bar{\nu}e.$$

These final state events can be categorized into two distinguishable classes. One category is the one without missing transverse momentum (NC type), like the first two decay modes; the other category is those with missing transverse momentum (high P_t^{miss} type) like the last two decay channels.

To establish an e^* sample of events with at least one electromagnetic cluster in the final state we require:

- the EM electron finder finds at least one energetic electromagnetic cluster that has transverse energy above 10 GeV ($E_t^{EM} > 10$ GeV). If the polar angle of the EM clusters are less than 0.3 rad the threshold is raised to 30 GeV.

- The number of cells in the electromagnetic cluster candidate should be greater than one and less than 30.

- Each electromagnetic cluster must have a polar angle less than 2.5 rad. Due to the asymmetric energies of the HERA beams, heavy excited electrons will be boosted in the forward direction. This in turn will result in the decay products being most often found at relatively forward angles.

- The electromagnetic clusters have to be "isolated": the sum of the calorimeter energy, within an $\eta - \phi$ cone of radius 0.8 which is centered on the cluster and not associated with the electromagnetic cluster, should be less than 2 GeV.[15]

- The longitudinal energy $E - P_z < 70$ GeV. The cut on $E - P_z$ rejects events for which the configuration of energy deposits in the calorimeter is forbidden by the energy-momentum conservation assuming an ep collision.

Figure 28 shows the distributions of the background Monte Carlo (MC) and data after these cuts (the background Monte Carlo is normalized to the total 96+97 integrated luminosity of 38.4 pb^{-1}).

[15] This condition is not required for $eq\bar{q}$ search, see Section 6.5.3.

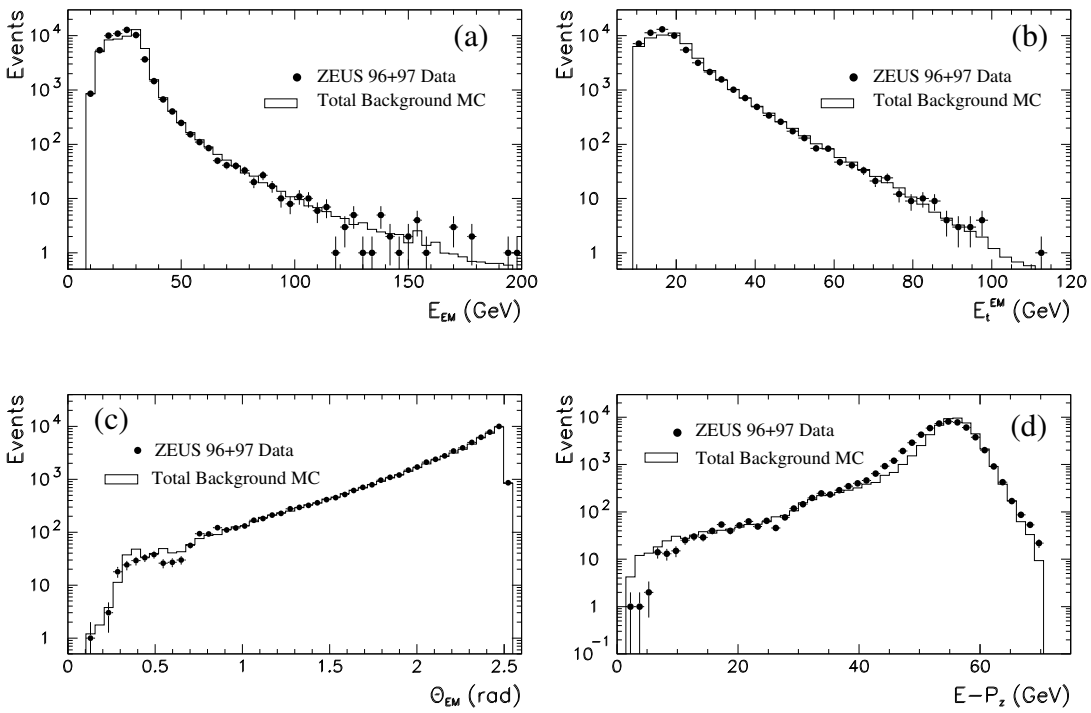

Figure 28: Comparison of data and total background Monte Carlo for the e^* events sample with an electromagnetic cluster in the final state. Distribution of (a) the electromagnetic cluster energy, (b) the transverse energy of the electromagnetic cluster, (c) the polar angle of the electromagnetic shower, (d) the longitudinal energy $E - P_z$.

8.2 Events without Electromagnetic Cluster

The decay

$$e^* \to \nu W \to \nu q\bar{q}'$$

has no electromagnetic cluster in the final state. Due to the escaping neutrino, the signature is missing transverse momentum, P_t^{miss}.

To establish an e^* sample of events with P_t^{miss} we require:

- events are rejected if they contain at least one clean electromagnetic clus-

ter. An electromagnetic cluster is a candidate in the calorimeter which has identified by the EM electron finder with a minimum energy of 4 GeV and probability of greater than 0.001 (this probability was tightened to 0.01 for events with polar angles less than 0.3 rad).

- A minimum missing transverse momentum of 10 GeV where the forward 10^o cone of the FCAL calorimeter is excluded ($P_t^{miss}(\theta > 10^o) > 10$ GeV). A large number of the NC DIS and γp events will be removed by this cut.

  This cut also removes beam-gas events which have the energy deposit concentrated at small polar angles in the FCAL.

- The longitudinal energy $E - P_z < 70$ GeV.

- Since the hadronic decay modes of the excited electrons contains a large hadronic transverse energy we require $E_t^{had} > 50$ GeV.

- Overall, a beam-gas event has the characteristics of low momentum (a few hundred MeV) tracks associated with the vertex as well as a large number of tracks which are not correlated with the vertex. By using these characteristics, the following cuts are applied to reject beam-gas events:

$$N_{good}^{Trk} \geq 1 \quad \text{and} \quad N_{good}^{Trk}/N_{Total}^{Trk} > 0.1,$$

  where N_{good}^{Trk} is the number of tracks in the angular range $15^o < \theta < 165^o$ with transverse momentum $p_t > 0.2$ GeV associated with reconstructed vertex, and N_{Total}^{Trk} is the number of reconstructed tracks.

  Figure 29 shows the distribution of the ratio of good tracks to total tracks before the application of the cuts on good tracks. As can be seen in the figure, there are a large number of events that have only fake tracks that do not correspond to the trajectory of a physical particle but occur as a result of

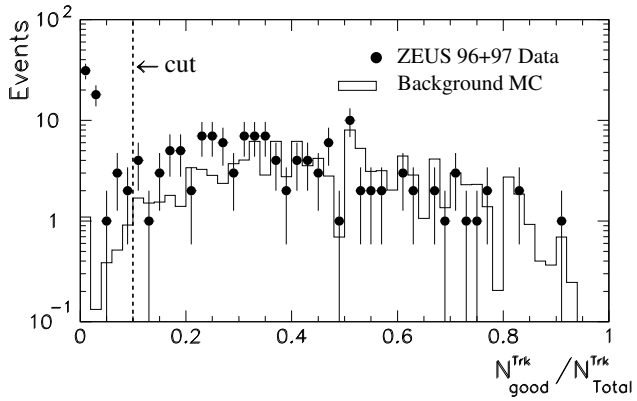

Figure 29: The distribution of the ratio of good tracks to total tracks before applying the cut on good tracks.

hits from different particles or even noise hits in the data. The distribution is not described at lower values by the Monte Carlo models.

After applying these tracking conditions, the number of good tracks is well described in the Monte Carlo as can be seen in Figure 30(d).

- The P_t^{miss} computed from the calorimeter excluding the largest P_t^{miss} cell must be greater than 10 GeV. This requirement suppressed the PMT sparks.

Figure 30 shows the distributions of total background Monte Carlo (including CC DIS, Photoproduction, and NC DIS) and data for the e^* sample of e^* events without an electromagnetic cluster in their final state (The background Monte Carlo is normalized to the luminosity of the data).

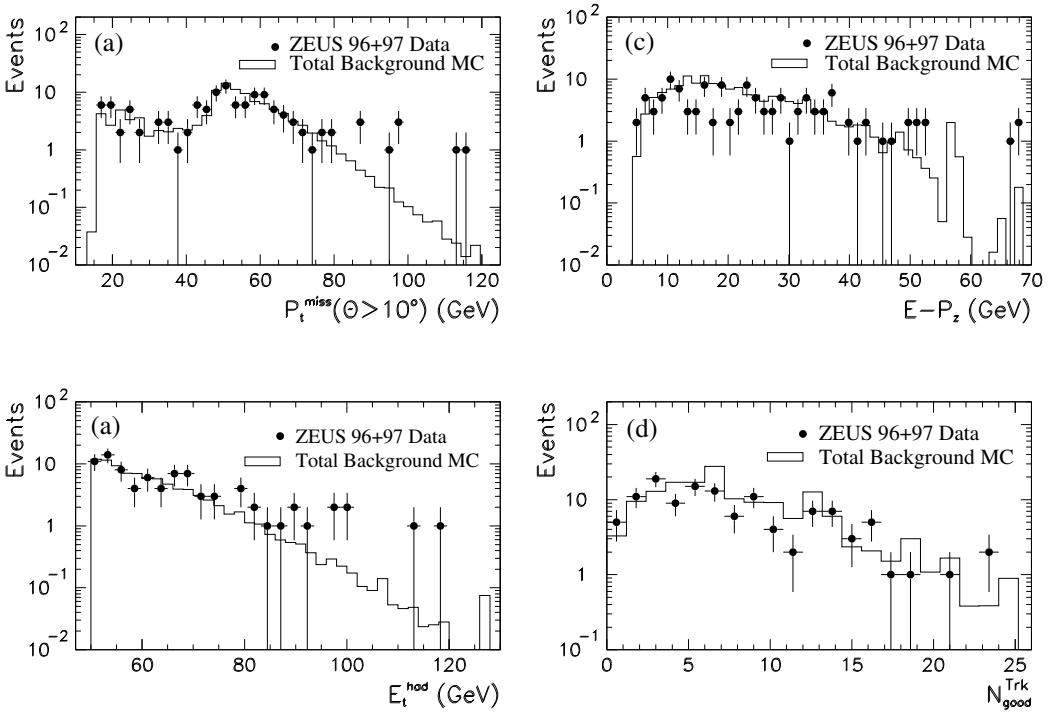

Figure 30: Comparison of data and background Monte Carlo (CC DIS + Photoproduction + NC DIS) for the sample of e^* events without an electromagnetic cluster in their final state. Distribution of (a) the missing transverse momentum, (b) the longitudinal energy $E - P_z$, (c) the hadronic transverse energy, (d) the number of good tracks.

8.3 Summary of e^* Event Samples

Table 8 summarizes the e^* event samples. At this stage the number of remaining events in the e^* event sample is 57371, containing at least one electromagnetic cluster in the final state. However, the number of remaining events in the e^* event sample with no electromagnetic cluster is 122, see Table 8. The number of events in the e^* event sample with at least one electromagnetic cluster but without requiring the isolation (used for $eq\bar{q}$ search) is 58098, which is a little

higher than the background estimation of 55915.3. This discrepancy is due to NC events with an energetic π^0 in the forward direction which is misidentified as an electromagnetic cluster.

Table 8: The summary of the e^* event samples.

e^* event sample with a least one EM cluster		
Data	**Background MC**	
57371	**55635.9**	
	NC DIS	55350.4
	QED-Compton	166.4
	Photoproduction	113.6
	W-Production	3.6
	CC DIS	1.9
e^* event sample with no EM cluster		
Data	**Background MC**	
122	**121.2**	
	CC DIS	104.9
	Photoproduction	9.5
	NC DIS	3.0

Table 9 gives the efficiency of signal Monte Carlo events after establishing the e^* event samples. It is clear that the electrons have very low energy for e^* masses just above the heavy boson masses and subsequently, the detection efficiency there is low. However, it increases with increasing e^* mass.

Table 9: The efficiency of the signal Monte Carlo after e^* event sample cuts.

Mode \ e^* Mass (GeV)	**100/110**†	**125**	**150**	**200**	**225**	**250**
Events with at least one electromagnetic cluster						
$e^* \to e\gamma$	82.8%	85.5%	87.7%	88.4%	86.6%	89.9%
$e^* \to eZ \to eq\bar{q}$	65.0%	78.9%	84.1%	89.0%	91.1%	91.3%
$e^* \to eZ \to e\nu\bar{\nu}$	69.2%	81.1%	85.8%	86.0%	84.7%	86.0%
$e^* \to \nu W \to \nu\bar{\nu}e$	81.2%	78.7%	76.8%	70.4%	65.9%	62.0%
Events with no electromagnetic cluster						
$e^* \to \nu W \to \nu q\bar{q}'$	24.0%	64.0%	72.1%	71.8%	72.7%	69.8%

† To evaluate the efficiency, we have used signal Monte Carlo events with mass of 100 GeV for $e^* \to e\gamma$, and $e^* \to \nu W$ decay modes and 110 GeV for $e^* \to eZ$ decay channels.

Chapter 9

e^* Mass Reconstruction

In the process of an excited lepton, F^*, decaying into an ordinary lepton, F, and a gauge boson, V, the signal would appear as a resonance peak in the FV invariant mass distribution. In general the FV invariant mass can be calculated as

$$\begin{aligned} M_{FV}^2 &= (p_F + p_V)^2 \\ &= (E_F + E_V)^2 \\ &- (P_{Fx} + P_{Vx})^2 - (P_{Fy} + P_{Vy})^2 - (P_{Fz} + P_{Vz})^2 \end{aligned} \tag{23}$$

where

$$p_F = (E_F, P_{Fx}, P_{Fy}, P_{Fz}) \qquad \text{and} \qquad P_V = (E_V, P_{Vx}, P_{Vy}, P_{Vz})$$

are the four-momenta of the decay lepton and gauge boson, respectively.

9.1 $e\gamma$ Invariant Mass

The electron-photon invariant mass, $M_{e\gamma}$, can be calculated from the measured four-momenta of the electron and photon in the calorimeter. The double angle method is an alternative method to determine the invariant mass $M_{e\gamma}$

$$M_{e\gamma}^2 \;=\; (2E_e^b)^2\,\frac{\sin\theta_\gamma + \sin\theta_e + \sin(\theta_\gamma+\theta_e)}{\sin\theta_\gamma + \sin\theta_e - \sin(\theta_\gamma+\theta_e)} \tag{24}$$

where θ_e and θ_γ are the polar angles of the electron and photon respectively and E_e^b is the electron beam energy (see Appendix B.1).

Figures 31 and 32 compare the resolution determined in invariant mass $M_{e\gamma}$ using the double angle method and the standard method using the calorimeter energy. The mass peaks from signal Monte Carlo events were fit with Gaussian lineshapes which were used to extract the resolution.

The double angle method gives better resolution. This is due to the fact that it applies the longitudinal energy conservation ($E - P_Z \;=\; 2\,E_e^b$) and neglects the transverse momentum of the recoiling hadronic system. It also reduces the sensitivity to systematic uncertainty in the calorimeter energy scale.

It should be mentioned that the double angle method does not improve the mass resolution for inelastically produced e^*, because ignoring the recoiling hadronic system is not entirely valid for these type of events. However, since the excited electrons are produced dominantly via the exchange of low-Q^2 photons, it is taken to be adequate. Also since the assumption $E - P_z = 2E_e^b$ is not valid for events with initial state radiation, it leads to a high energy tail in the $e\gamma$ invariant mass distribution.

9.2 eZ Invariant Mass

Due to the limited hadronic resolution of the calorimeter as well as leakage in the very forward region, the calculation of the invariant mass from the calorimeter

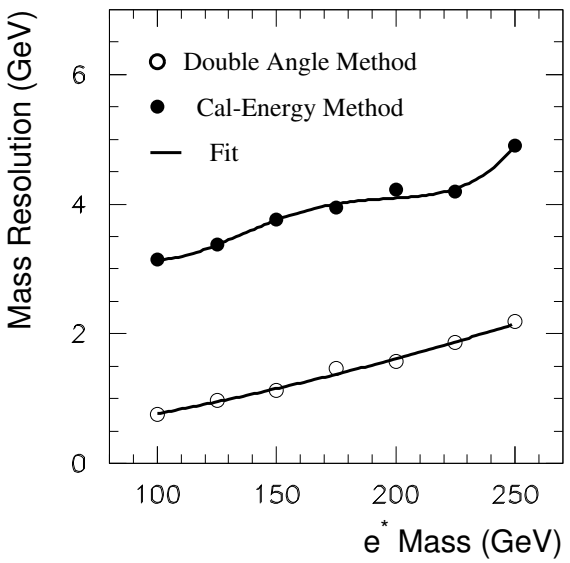

Figure 31: Comparison of the resolution determined in invariant mass $M_{e\gamma}$ using the double angle method and the standard calorimeter energy (Cal-Energy) method for $e^* \to e\gamma$ as a function of e^* mass. The smooth curves are polynomial fits to the points.

has poor resolution. It is more accurate to calculate the invariant mass M_{eZ} from

$$M_{eZ}^2 \;=\; \frac{4\,E_e^b E_e'\,\cos^2\frac{\theta_e}{2} \;+\; M_Z^2}{1 - \frac{E_e'}{E_e^b}\,\sin^2\frac{\theta_e}{2}} \tag{25}$$

where E_e' is the final state electron energy, θ_e is the polar angle of the electron, and M_Z is the nominal Z mass,[16] see Appendix B.2.

In the above formula, it is assumed that the excited electron has negligible transverse momentum and $E - P_z = 2E_e^b$. By focusing only on the electron measurements, this method has better results than the ones which involve the computation of the total calorimetric invariant mass, Figures 33 and 34.

[16] In $eq\bar{q}$ or $e\nu\bar{\nu}$ final state decay channels, it is assumed that the mass of the $q\bar{q}$ or $\nu\bar{\nu}$ systems are equal to the Z mass.

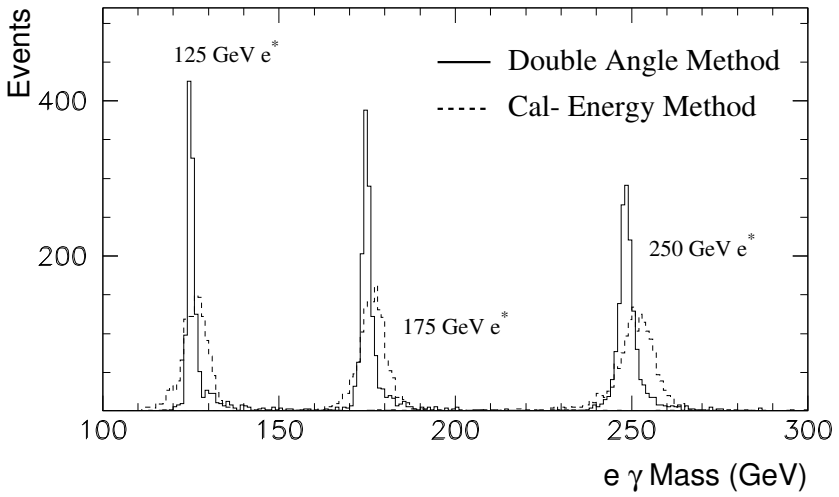

Figure 32: Distribution of the $e\gamma$ invariant mass for 125, 175, and 250 GeV $e^* \to e\gamma$ using the double angle method (solid histograms) and the standard calorimeter energy (Cal-Energy) method (dashed histograms).

9.3 νW Invariant Mass

The reconstruction of the invariant mass of the νW system, $M_{\nu W}$, is possible using the transverse momentum, P_t, of the hadronic system and $\delta \equiv E - P_z$ where E is the total energy and P_z is the momentum of the hadronic system along the z direction. Assuming that e^* is produced with negligible transverse momentum, the mass is obtained from

$$M^2_{\nu W} = \frac{4\,P_t^2\,(\,E_e^b)^2\,+\,2\,E_e^b\,M_W^2\,(\,2\,E_e^b\,-\,\delta\,)}{\delta\,(\,2\,E_e^b\,-\,\delta\,)} \tag{26}$$

where M_W is the W boson mass,[17] see Appendix B.3.

[17] In $\nu q\bar{q}$ final state decay mode, we require the constraint that the mass of the $q\bar{q}$ system is equal to the W mass.

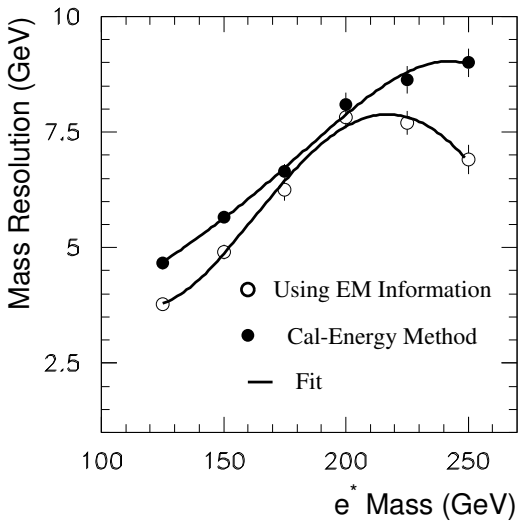

Figure 33: Comparison of the resolution in invariant mass M_{eZ} using the electron information (energy and polar angle of the electron) and the standard calorimeter energy (Cal-Energy) method for $e^* \to eZ$ as a function of e^* mass. The smooth curves are polynomial fits to the points.

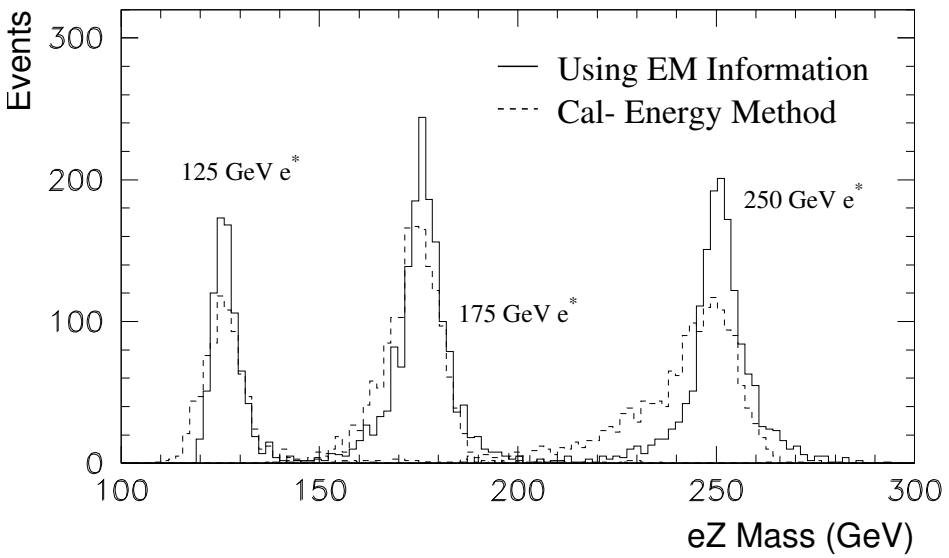

Figure 34: Distribution of the eZ invariant mass for 125, 175, and 250 GeV $e^* \to eZ \to eq\bar{q}$ using the double angle method (solid histograms) and the standard calorimeter energy (Cal-Energy) method (dashed histograms).

Chapter 10

Search for Excited Electron

We now search for excited electrons using the event samples selected in Chapter 8.

10.1 $e\,\gamma$ Resonance Search

The $e^* \to e\gamma$ decay mode is the preferred channel to search for excited electrons at HERA because of its clean signature and high branching ratio ($> 30\%$ up to $M_{e^*} = 250$ GeV).

The main signature for the decay $e^* \to e\gamma$ comprises two isolated energetic electromagnetic clusters in the calorimeter and, if the proton dissociates, hadronic energy around the forward beam pipe but otherwise a quiet detector, Figure 35.

QED-Compton scattering ($ep \to e\,\gamma\,X$) and NC DIS events are the dominant background processes to this topology. NC events have an isolated π^0 in the forward direction and a scattered electron in the backward direction.

Furthermore, QED-Compton scattering has the same topology, and thus forms a non-resonant background at low invariant masses. Due to the differences in the angular distribution of the QED-Compton scattering and excited electron decays, these two can be separated.

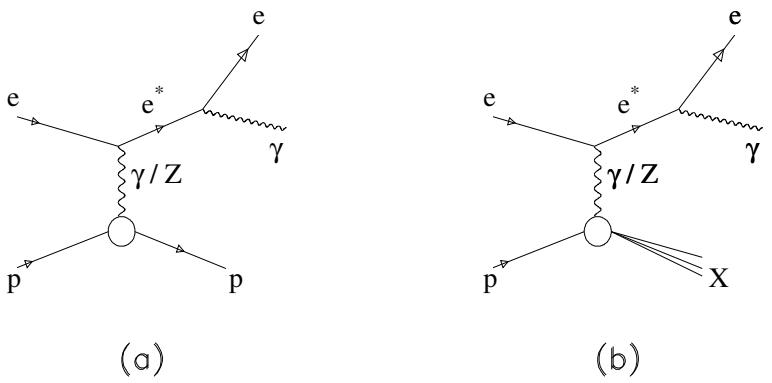

Figure 35: Diagrams for the production and decay of excited electron $e^* \to e\gamma$ via (a) elastic and (b) inelastic processes in ep collisions.

10.1.1 Final $e\gamma$ Sample

Beginning with the excited electron event sample, two energetic electromagnetic clusters[18], are sought using the EM electron finder, tuned for selection of NC DIS events. In this analysis we do not distinguish electron from photon. This treatment requires:

- the transverse energy of each electromagnetic cluster is required to be above 10 GeV, and if its polar angle is less than 0.3 rad the threshold is raised to 30 GeV, see Figure 36.

  Figure 37 presents the distribution of the transverse energy of the highest E_t electromagnetic cluster versus that of the second highest E_t electromagnetic cluster for different mass $e^*(\to e\gamma)$, NC DIS, and QED-Compton Monte

[18]Both electromagnetic clusters are accepted as candidates if their probabilities exceeds 0.001. The probabilities are raised to 0.01 for electromagnetic clusters with polar angle less than 0.3 rad.

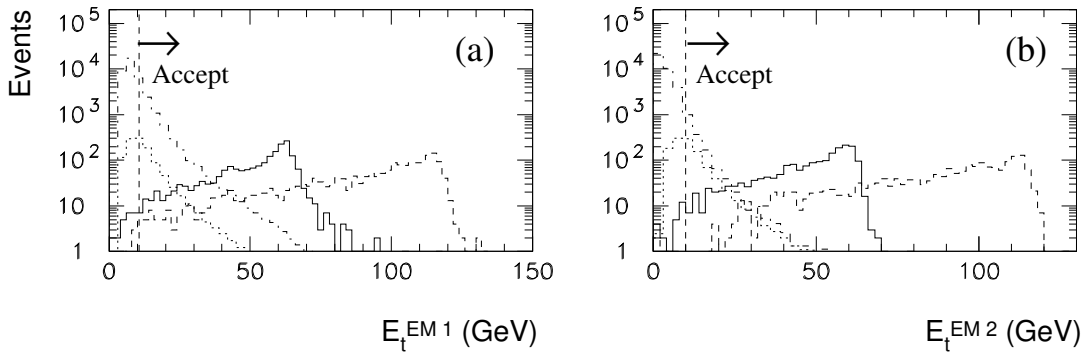

Figure 36: The distribution of transverse energy (after cleaning cuts) of (a) the highest E_t electromagnetic cluster ($E_t^{EM\,1}$), and (b) those of the the second highest electromagnetic cluster ($E_t^{EM\,2}$), for 125 GeV (solid line) and 225 GeV (dashed line) $e^*(\rightarrow e\gamma)$, NC DIS (dash-dotted line), QED-Compton Monte Carlo (dotted line), The accepted region is to the right of the dashed vertical lines.

Carlo events.[19]

- the electromagnetic clusters have to be "isolated":

$$E_{EM1}^{iso}(R < 0.8) < 2\ \text{GeV} \quad \text{and} \quad E_{EM2}^{iso}(R < 0.8) < 2\ \text{GeV}.$$

This requirement suppresses the background of NC DIS events with an energetic π^0 in the forward direction which is misidentified as a photon, Figure 38.

- Each electromagnetic cluster must have a polar angle less than 2.0 rad. Figure 39 indicates that as the e^* mass increases, the polar angle of the decay electromagnetic clusters decreases.

[19] We require the number of cells for both electromagnetic clusters to be greater than 1 and less than 30.

Figure 40 presents the distribution of polar angle of the highest E_t electromagnetic cluster versus that of the second highest E_t electromagnetic cluster for $e^*(\rightarrow e\gamma)$ signal Monte Carlo events with different masses.

The figure reflects the fact that the cut $\theta_e < 2$ rad on polar angles of the electromagnetic showers has no significant effect on the signal Monte Carlo. However, there is a dramatic suppression effect on the NC DIS and QED-Compton backgrounds.

- Events are rejected if both electromagnetic clusters have one or more matching tracks with a distance of closest approach less than 10 cm. Events are also rejected if both electromagnetic clusters are inside the efficient tracking region (polar angle more than 0.3 rad) and have no matching track.

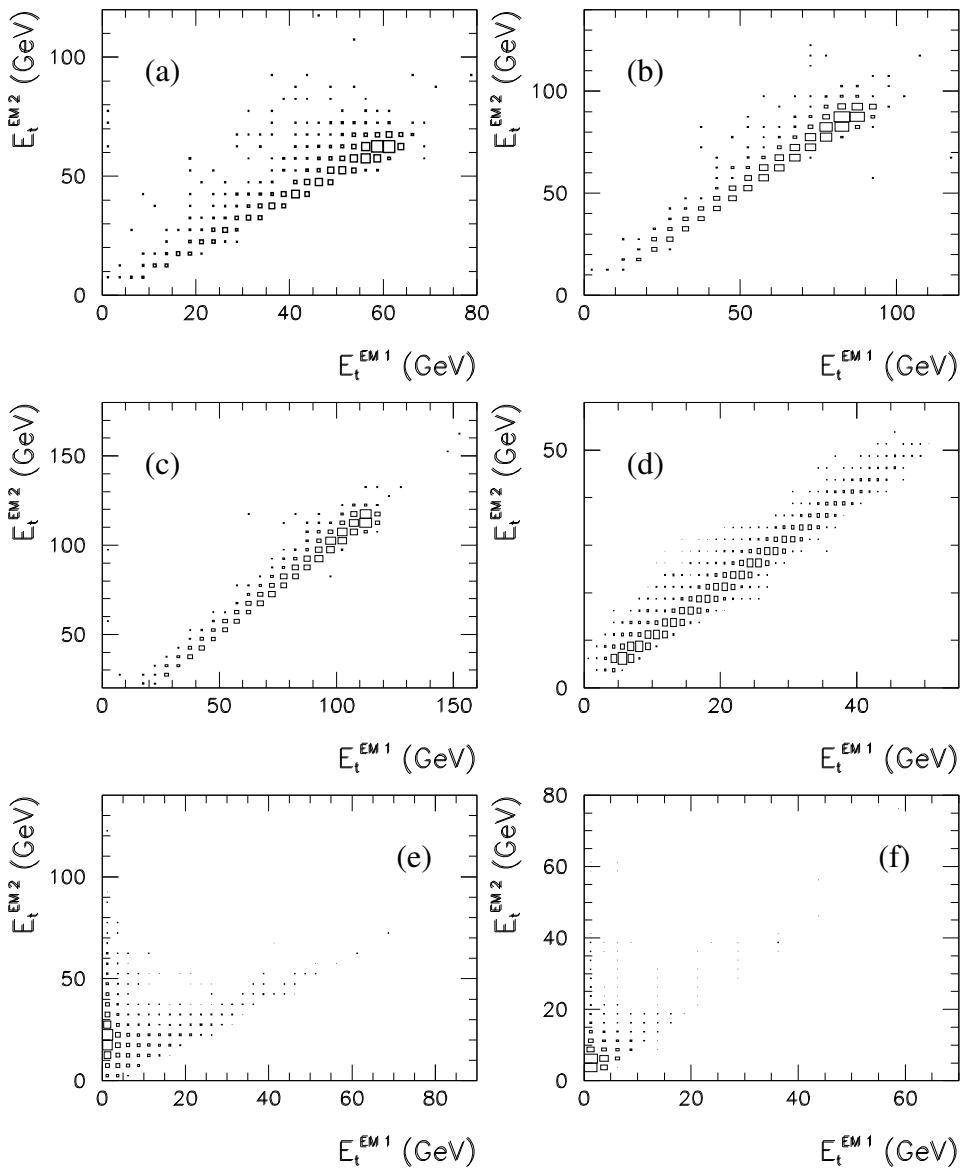

Figure 37: The distribution of transverse energy (after cleaning cuts) of the highest E_t electromagnetic cluster versus that of the second highest E_t electromagnetic shower for (a) 125 GeV, (b) 175 GeV, (c) 225 GeV $e^*(\rightarrow e\gamma)$, (d) QED-Compton, and (e) NC DIS Monte Carlo, and (d) data.

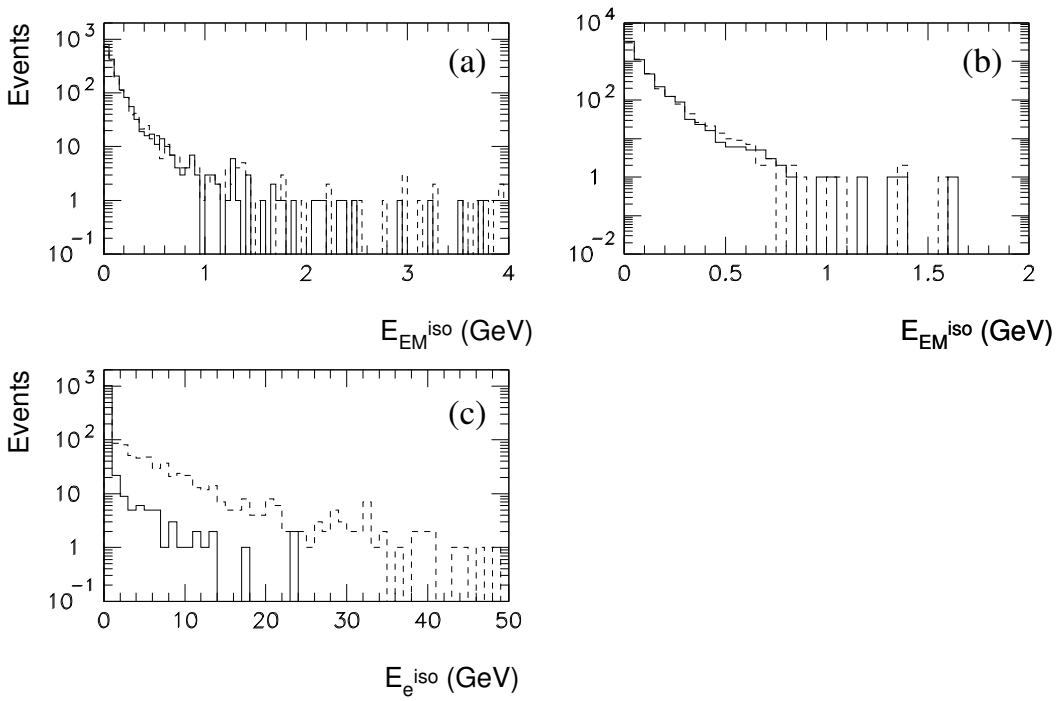

Figure 38: The distribution of the energy in an $\eta - \phi$ cone of radius 0.8 that is not assigned to the electromagnetic cluster candidate (after cut on electromagnetic cluster transverse energies) of the highest E_t (solid line) and that of the second highest E_t (dashed line) electromagnetic cluster for (a) 125 GeV $e^* \to e\gamma$, (b) QED-Compton, and (c) NC DIS Monte Carlo. The distribution for higher mass $e^* \to e\gamma$ Monte Carlo events are similar to those shown in (a).

- Events within the detector must have 35 GeV $< E - P_z <$ 65 GeV. This limits the effect of initial state radiation, see Figure 8.

- Defining the energy asymmetry factor

$$\Delta E_t^{EM} / \sum E_t^{EM} = \frac{\left| E_t^{EM1} - E_t^{EM2} \right|}{E_t^{EM1} + E_t^{EM2}},$$

  we require $\Delta E_t^{EM} / \sum E_t^{EM}$ to be less than 0.15, Figure 41.

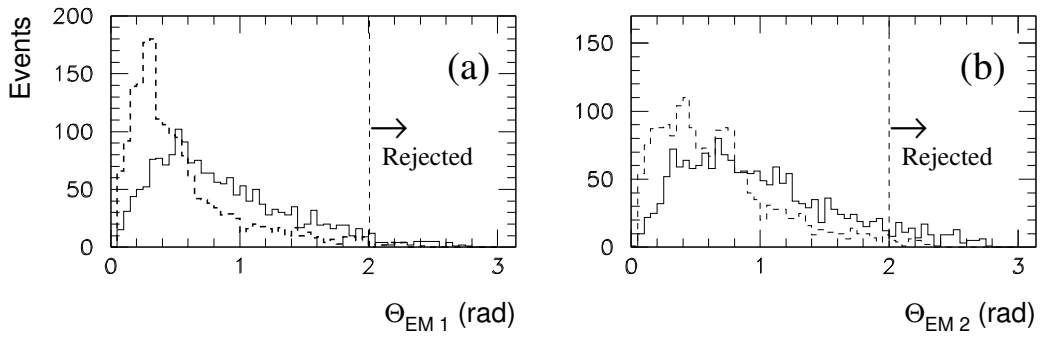

Figure 39: The polar angle distribution (after a cut on E_t and isolation of the electromagnetic clusters) of (a) the highest E_t electromagnetic cluster (θ_{EM1}), and (b) of the the second highest electromagnetic cluster (θ_{EM2}), for 125 GeV (solid line) and 225 GeV (dashed line) $e^*(\rightarrow e\gamma)$. The rejected events are to the right of the dashed vertical lines.

- The total number of tracks associated with the event vertex having transverse momentum larger than 0.2 GeV and $15^o < \theta < 165^o$, so-called good tracks, has to be 3 or less. This condition preferentially selects elastic and quasi-elastic production of excited electrons. This cut rejects most of the NC DIS events which have many tracks while not affecting QED-Compton events much as shown in Figure 42.

Figure 43 shows the distributions after all cuts for data and Monte Carlo. A total of 49 data events pass these selection criteria in fair agreement with the Monte Carlo background estimation of 63 ± 2 events. The estimation for the background from NC DIS is 26.4 events and the estimation from QED-Compton scattering is 37.1.

The effect of the various cuts are listed in Table 10. The efficiency for the signal Monte Carlo after all cuts ranges from about 60% for e^* masses of 100 GeV and increases to 77.5% at higher masses, Figure 44(a). The uncertainty on the estimation of the efficiency for most of the signal Monte Carlo events is estimated

to be less than 1%.[20].

The double angle method is a good way of determining the electron-photon invariant mass, Eq. (24). The Gaussian mass resolution for e^* Monte Carlo events ranges from 0.78 GeV for $M_{e^*} = 100$ GeV to 2.19 GeV for $M_{e^*} = 250$ GeV, Figure 44(b).

Figure 45 is an example of the comparison of the invariant mass spectrum of the data and the Monte Carlo background prediction. An example of an $e^* \to e\gamma$ signal is also shown in the figure.

There is agreement between the 8.8 ± 0.7 events expected from the background and five events with an $e\gamma$ invariant mass larger than 100 GeV. The estimation of the background from NC DIS, in this range, is expected to be 5.4 events and the estimation for the QED-Compton scattering is 3.4 events. No significant excess of events characteristic of a peak for e^* production is observed. Figure 46 shows the event display of the highest mass (158 GeV) candidate for the $e\gamma$ search.

---

[20] The uncertainty on the estimation of the efficiency for signal Monte Carlo events, $\delta\epsilon$, can be calculated from

$$\delta\epsilon = \sqrt{\frac{\epsilon(1-\epsilon)}{N}}$$

where ϵ is the overall efficiency of the signal after all cuts, and N is the total number of generated events.

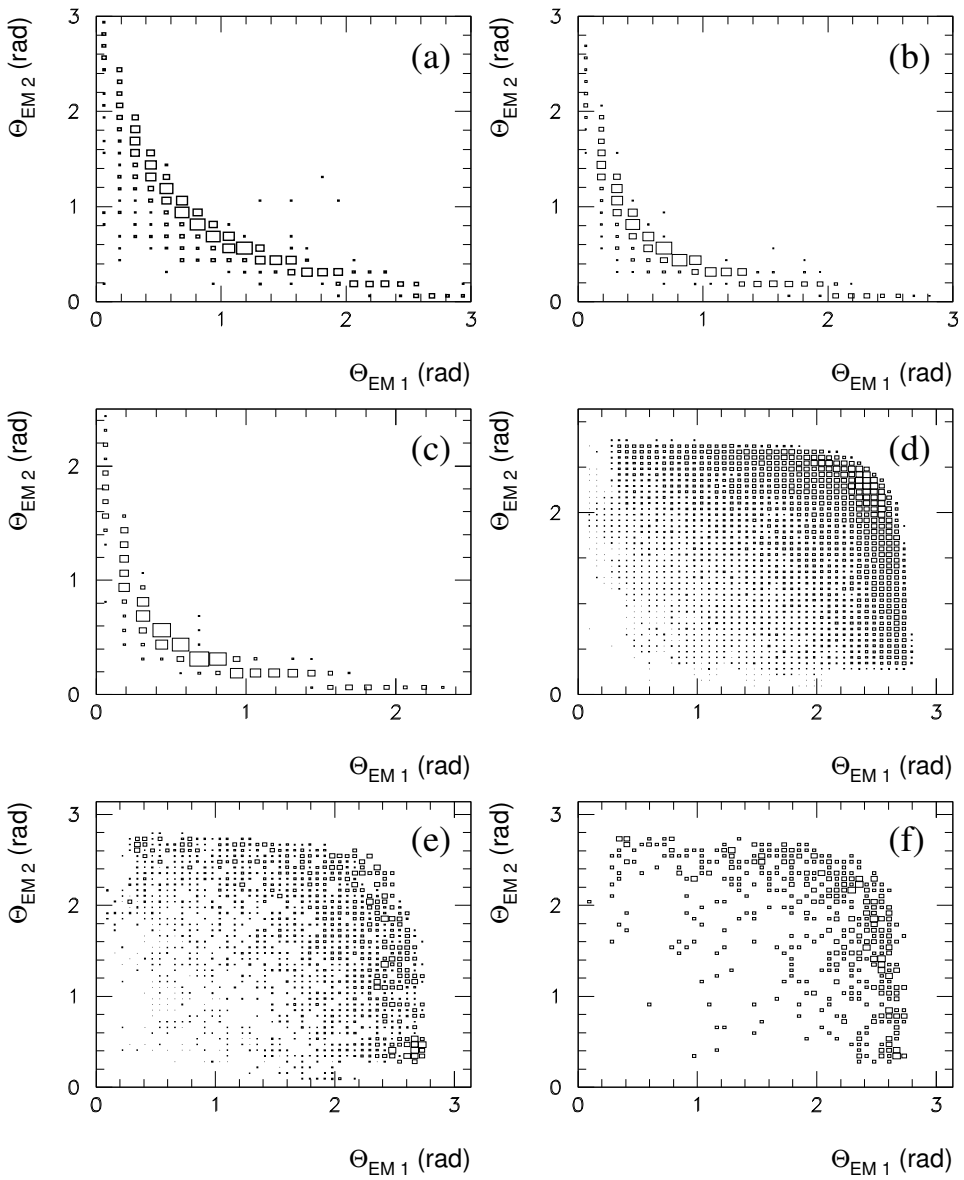

Figure 40: The distribution of polar angle (after cut on E_t and isolation of the electromagnetic clusters) of the highest E_t electromagnetic cluster versus that of the second highest E_t electromagnetic shower for (a) 125 GeV, (b) 175 GeV, (c) 225 GeV $e^*(\rightarrow e\gamma)$, and (d) QED-Compton, and (e) NC DIS Monte Carlo events, and (f) data.

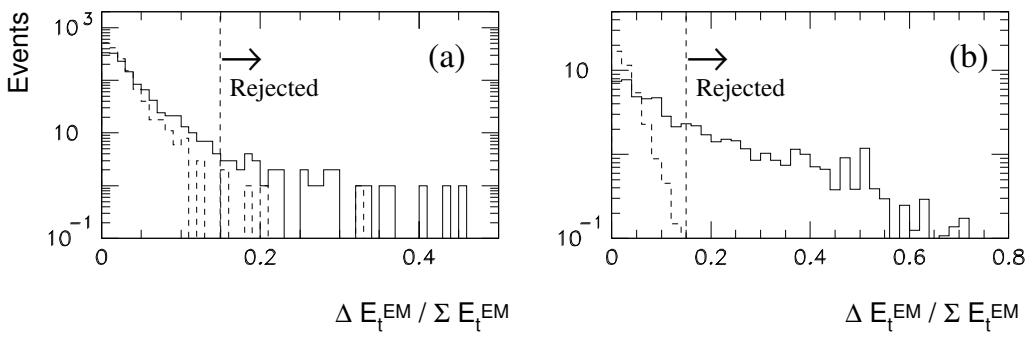

Figure 41: The distribution of the energy asymmetry, $\Delta E_t^{EM} / \sum E_t^{EM}$, (after cut on E_t and θ and isolation of the electromagnetic clusters and $E - P_z$) for (a) 125 GeV (solid line) and 225 GeV (dashed line) $e^*(\rightarrow e\gamma)$, (b) NC DIS (solid line), and QED-Compton Monte Carlo (dashed line). The rejected events are to the right of the dashed vertical lines.

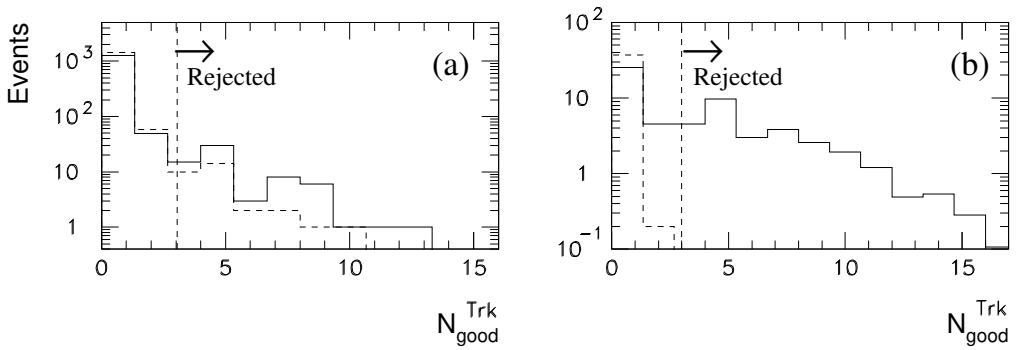

Figure 42: The distribution of number of good tracks (after cut on E_t and θ and isolation of the electromagnetic clusters and $E - P_z$ and energy asymmetry) for (a) 125 GeV (solid line) and 225 GeV (dashed line) $e^*(\rightarrow e\gamma)$, (b) NC DIS (solid line), and QED-Compton Monte Carlo (dashed line). The rejected events are to the right of the dashed vertical lines.

Figure 43: Comparison of data and background Monte Carlo after all cuts in the $e\gamma$ search. Distribution for (a) the transverse energy of the highest E_t electromagnetic cluster, (b) and that of the second highest E_t electromagnetic cluster, (c) the polar angle of highest E_t electromagnetic cluster, (d) and that of the second highest E_t electromagnetic cluster; (e) the longitudinal transverse momentum $E - P_z$, (f) the asymmetry between the transverse energy of the two electromagnetic clusters, and (g) the number of good tracks. The solid points show the 96+97 ZEUS data and the open histograms represent the expected total background from NC DIS and QED-Compton Monte Carlo events. The contribution from the QED-Compton process is shown by the shaded histograms.

Figure 43

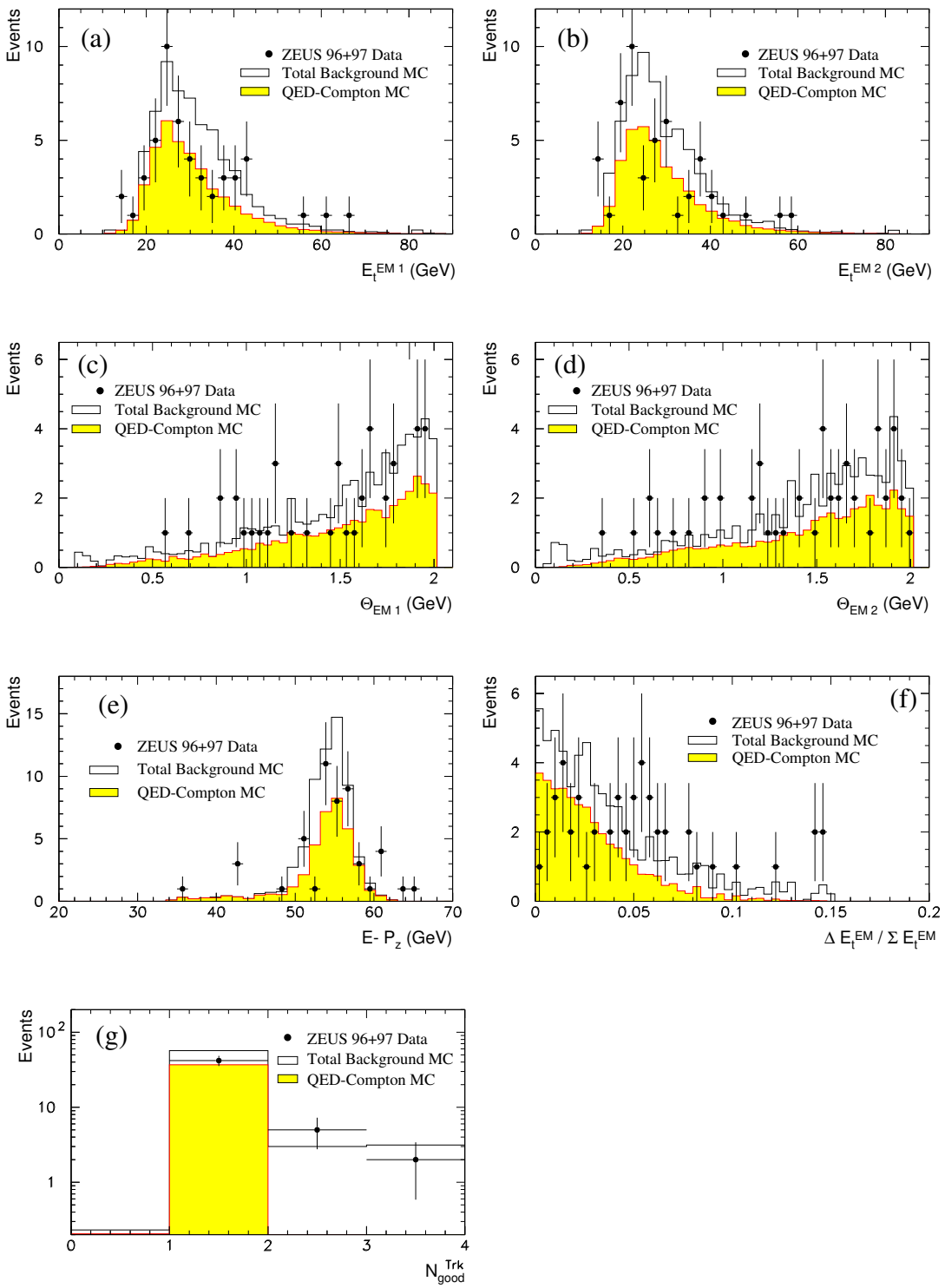
(a)
ZEUS 96+97 Data
Total Background MC
QED-Compton MC
Events
$E_t^{EM\,1}$ (GeV)
(b)
ZEUS 96+97 Data
Total Background MC
QED-Compton MC
Events
$E_t^{EM\,2}$ (GeV)
(c)
ZEUS 96+97 Data
Total Background MC
QED-Compton MC
Events
$\Theta_{EM\,1}$ (GeV)
(d)
ZEUS 96+97 Data
Total Background MC
QED-Compton MC
Events
$\Theta_{EM\,2}$ (GeV)
(e)
ZEUS 96+97 Data
Total Background MC
QED-Compton MC
Events
E- P_z (GeV)
(f)
ZEUS 96+97 Data
Total Background MC
QED-Compton MC
Events
$\Delta E_t^{EM} / \Sigma E_t^{EM}$
(g)
ZEUS 96+97 Data
Total Background MC
QED-Compton MC
Events
N_{good}^{Trk}

Table 10: (a) Efficiency for $e^* \to e\gamma$ signal Monte Carlo (fraction of accepted events). The last line in the table shows the overall efficiency. (b) The comparison between data and background Monte Carlo expectation. The table entries are the number of accepted events after each cut.

(a)

Cuts \ e^* Mass (GeV)	**100**	**125**	**150**	**200**	**225**	**250**
e^* Event Sample	82.8%	85.5%	87.7%	89.5%	86.6%	89.9%
$E_t^{EM1,EM2} > 10$ GeV†	74.1%	77.0%	82.2%	83.3%	82.2%	84.5%
$\theta_{EM1,EM2} < 2$ rad	71.8%	76.5%	81.8%	80.9%	81.9%	83.7%
At most one EM track	65.9%	71.0%	76.5%	75.1%	77.3%	78.9%
$35 < E - P_z < 65$ GeV	64.6%	70.2%	74.8%	74.1%	77.1%	78.2%
$\Delta E_t / \sum E_t < 0.15$	61.7%	68.1%	74.3%	74.0%	77.0%	78.1%
# of Good Track ≤ 3‡	59.5%	66.2%	73.6%	72.6%	76.2%	77.5%
Efficiency	**59.5%**	**66.2%**	**73.6%**	**72.6%**	**76.2%**	**77.5%**

(b)

Cuts	NC DIS	QED-Compton	**Total BG**	**DATA**
e^* Event Sample	55350.4	166.4	**55516.8**	**57371**
$E_t^{EM1,EM2} > 10$ GeV†	448.3	310.5	**758.8**	**832**
$\theta_{EM1,EM2} < 2$ rad	69.7	43.7	**113.4**	**114**
At most one EM track	57.6	41.1	**98.7**	**83**
$35 < E - P_z < 65$ GeV	54.1	37.4	**91.5**	**78**
$\Delta E_t / \sum E_t < 0.15$	36.6	37.2	**73.8**	**56**
# of Good Track ≤ 3‡	26.4	37.1	**63.5**	**49**

† Including the isolation requirement for both electromagnetic clusters.

‡ A good track is defined as a transverse momentum larger than 0.2 GeV and $15^o < \theta < 165^o$.

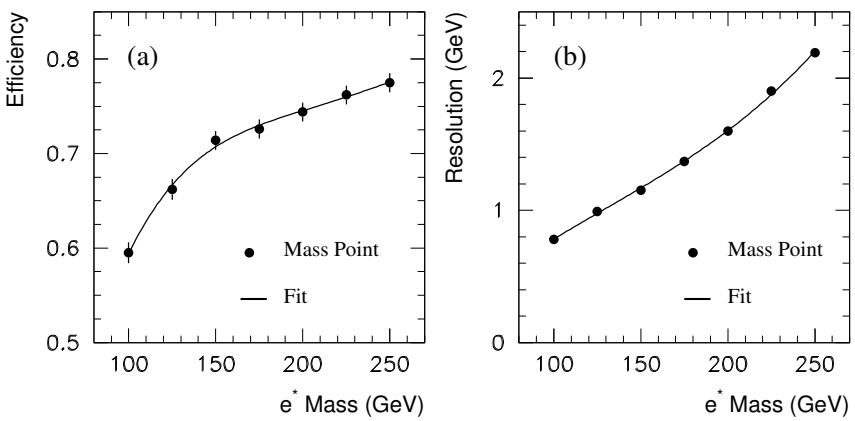

Figure 44: (a) Efficiency and (b) width of the reconstructed mass (mass resolution) for Monte Carlo e^* events decaying into $e\gamma$ as a function of the mass of the excited electron. The smooth curves are polynomial fits to the points.

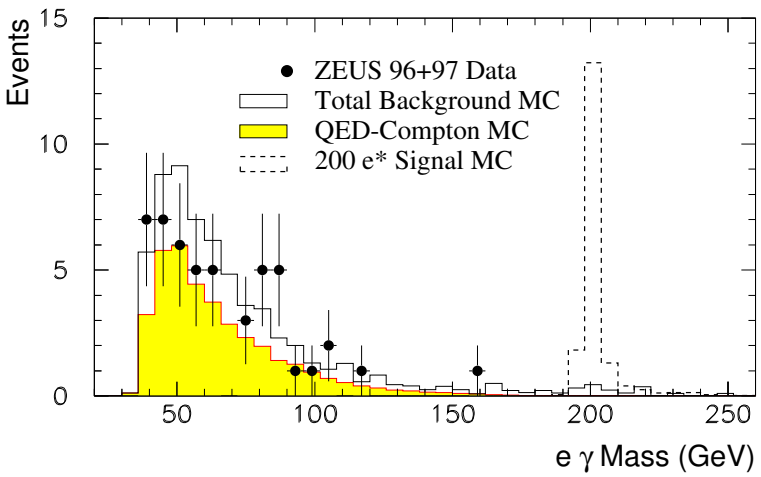

Figure 45: Invariant mass distribution of the $e\gamma$ system for $e^* \rightarrow e\gamma$ after all cuts. The solid points show the 96+97 ZEUS data and the open histogram represents the expected total background from NC DIS and QED-Compton Monte Carlo events. The contribution from the QED-Compton process is shown by the shaded histogram. An example of a signal from e^* with a mass of 200 GeV is also shown as the dashed histogram.

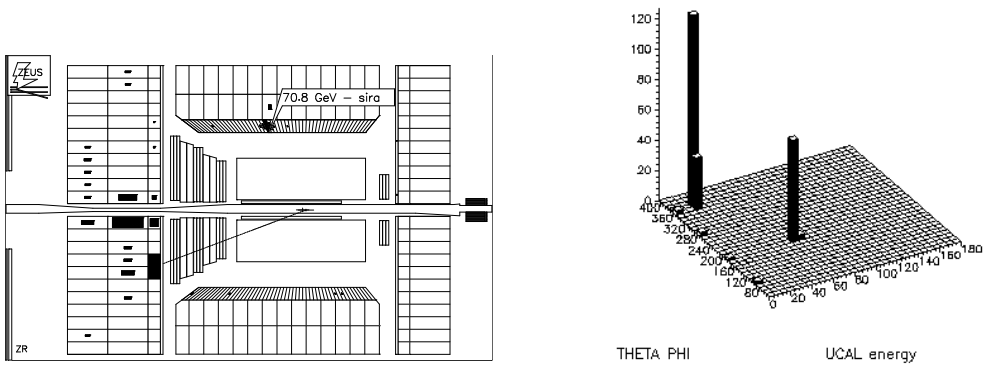

Figure 46: The highest mass candidate event for the $e\gamma$ search. The $e\gamma$ invariant mass for this event is 158 GeV. The left part of the event display shows a vertical cut through the ZEUS detector. The protons enter from right, the electron from left. The collisions occur in the center of the detector which is surrounded by CTD and the calorimeter. The final state electron (with a track) is in the FCAL and the photon in the BCAL. The right lego plot shows the distribution of transverse energy as a function of azimuth and polar angle.

10.2 $eq\bar{q}$ Resonance Search

The $eq\bar{q}$ final state could arise from the $e^* \rightarrow eZ$ decay channel with the Z decaying hadronically[21], Figure 47.

The signature for this decay is two jets with dijet invariant mass close to the Z mass and an energetic electromagnetic cluster (mainly in the forward region). The dominant background for this signature is NC DIS with more than one final state jet.

10.2.1 Final $eq\bar{q}$ Sample

To separate the signal from the background, we start with the e^* event sample containing at least one electromagnetic cluster in the final state without isolation

[21]The hadronic branching ratio of the Z boson is 69.90%.

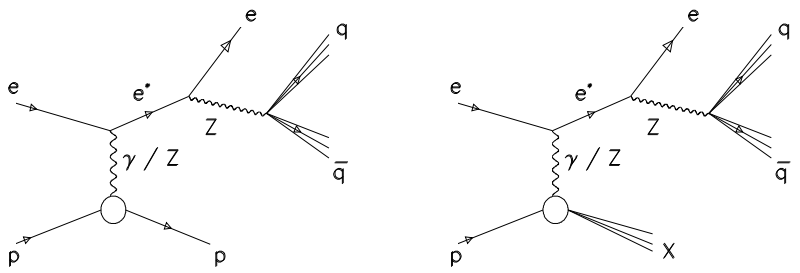

Figure 47: Diagrams for the production and decay of excited electron $e^* \to eZ \to eq\bar{q}$ via (a) elastic and (b) inelastic processes in ep collisions.

requirement and:

- raise the minimum requirement of transverse energy (E_t^e) of the electromagnetic cluster to greater than 25 GeV, see Figure 5(a). Furthermore, if its polar angle is less than 0.3 rad, the threshold is raised to $E_t^e > 30$ GeV.

  It is important to notice that since the electron in this channel may be in close proximity to one of the jets we do not require any isolation requirement, Figure 25(d).

- An electron with one track matching within a distance of closest approach of less than 10 cm is required. Moreover, the transverse momentum of the corresponding track needs to be greater than 5 GeV.

- A polar angle of less than 2 rad is required for the electromagnetic cluster, Figure 6. It should be noted that along with increase of the mass of the e^*, there will be a decrease in the polar angle of the electron. This requirement reduces the NC DIS background contribution while not affecting excited electron events much.

- We require 35 GeV $< E - P_z <$ 65 GeV, Figure 8. This selects NC events contained in the calorimeter.

- A large hadronic transverse energy (E_t^{had}) and hadronic mass (M^{had}) is expected to be produced by the hadronic Z boson decay, Figure 48. Figure 48(b) reflects the fact that the ZEUS detector is able to reconstruct Z bosons decaying into hadronic final states. A tail toward lower hadronic mass at higher e^* masses is due to the loss of the hadrons from the decay of the Z boson in the very forward region. Figure 49 is an indicator of the reconstruction of Z mass resolution as well as a shift of mass from the nominal Z mass as a function of e^* mass. In any of these conditions where $E_t^{had} > 60$ GeV and $M_{had} > 80$ GeV or if $E_t^{had} > 80$ GeV and $M_{had} > 40$ GeV, the events are accepted, Figure 50. A good efficiency for high mass excited fermion events is provided by this latter cut.

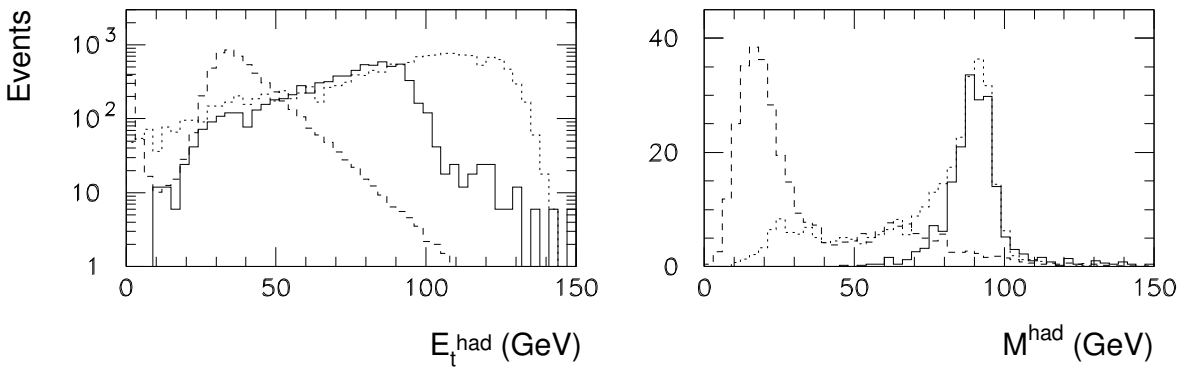

Figure 48: The distribution of (a) the hadronic transverse energy (E_t^{had}) for 125 GeV (solid line) and 225 GeV (dotted line) $e^*(\rightarrow eZ \rightarrow eq\bar{q})$, NC DIS (dashed line) after cuts on E_t and θ of the electron and $E - P_z$, and (b) the distribution of the hadronic mass (M^{had}) for 125 GeV (solid line) and 225 GeV (dotted line) $e^*(\rightarrow eZ \rightarrow eq\bar{q})$, and NC DIS (dashed line) Monte Carlo, after cuts on E_t and θ of the electron and $E - P_z$, and also requiring $E_t^{had} > 60$ GeV.

- For the further reduction of the background the ratio M^{Total}/M_{eZ}, where M^{Total} is the total effective mass measured with the calorimeter, Eq. (21), has to be between 0.8 and 1.2, Figure 51.

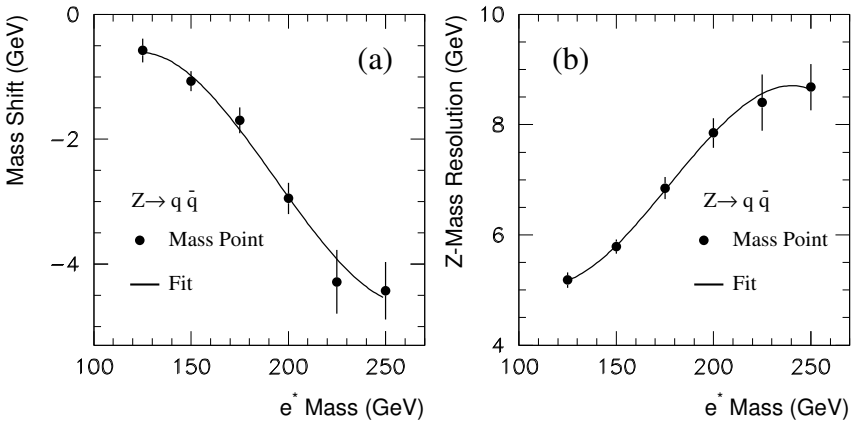

Figure 49: (a) The difference between the reconstructed Z mass and the nominal Z mass, (b) the reconstructed Z mass resolution as a function of e^* mass. The smooth curves are polynomial fits to the points.

Figure 52 shows the distribution after all cuts for data and Monte Carlo. There are 29 events accepted with an expected background of 26.5 ± 0.9 events. The effect of the various cuts are listed in Table 11. The overall efficiency for $e^* \to eZ \to eq\bar{q}$ of the selection cuts for masses above 150 GeV is about 50%, Figure 53(a). Here, the information of electron (energy and polar angle of electron) is used to calculate the eZ invariant mass, Eq. (25). The Gaussian mass resolution for e^* Monte Carlo events is less then 7 GeV for masses up to 250 GeV, Figure 53(b).

Figure 54 shows the invariant mass spectrum of the data compared with the Monte Carlo background prediction. An example of e^* signal Monte Carlo is also shown in the figure. No significant excess of events characteristic of a peak for e^* production is observed. Figure 55 shows the event display of the highest mass candidate for the $eq\bar{q}$ search. The invariant mass of this event is 235 GeV.

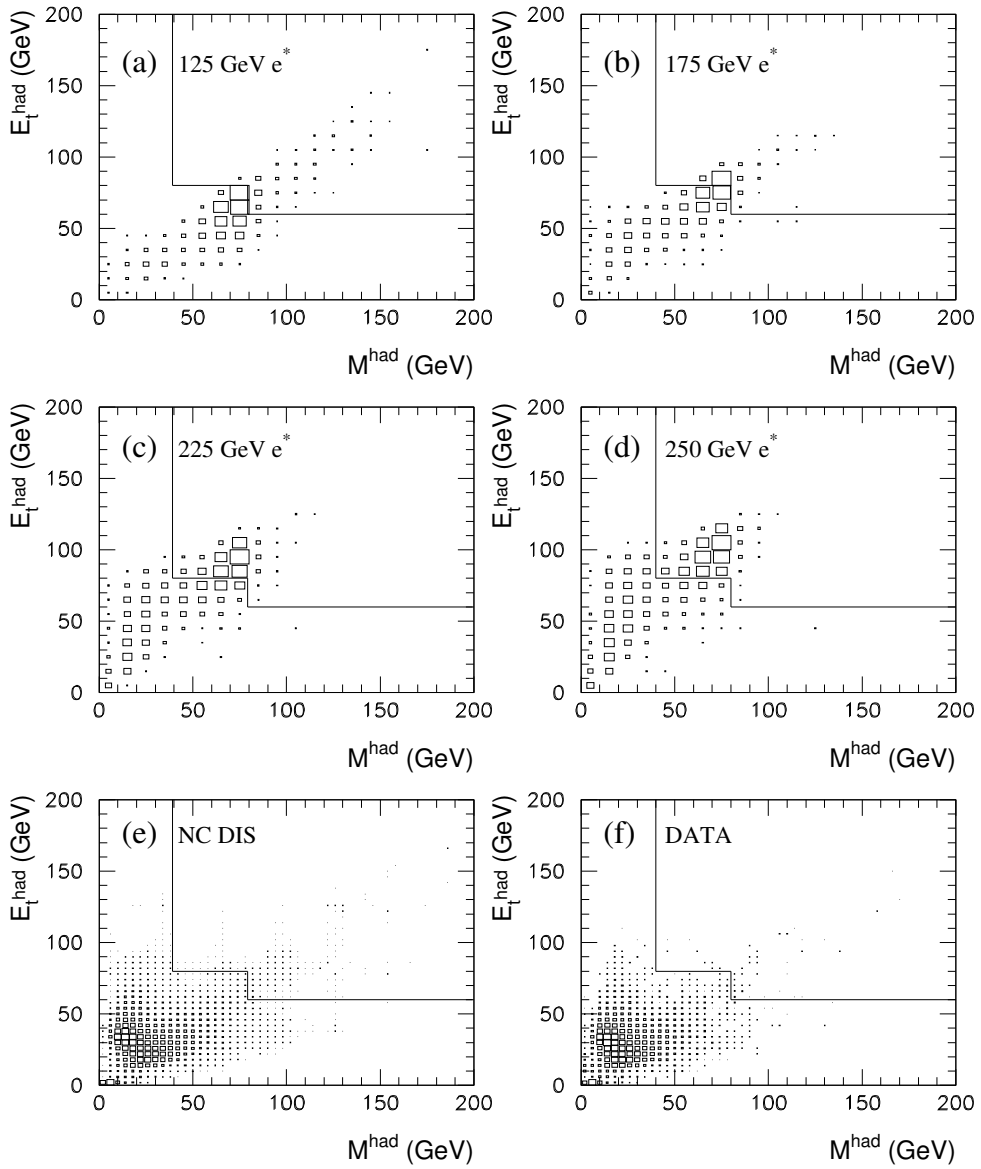

Figure 50: The distribution of the hadronic mass (M^{had}) versus the transverse hadronic energy (E_t^{had}) for (a) 125 GeV, (b) 175 GeV, (c) 225 GeV, and (d) 250 GeV $e^*(\rightarrow eZ \rightarrow eq\bar{q})$, (e) NC DIS Monte Carlo, and (f) data. The solid lines show the cut; the accepted region is to the upper right.

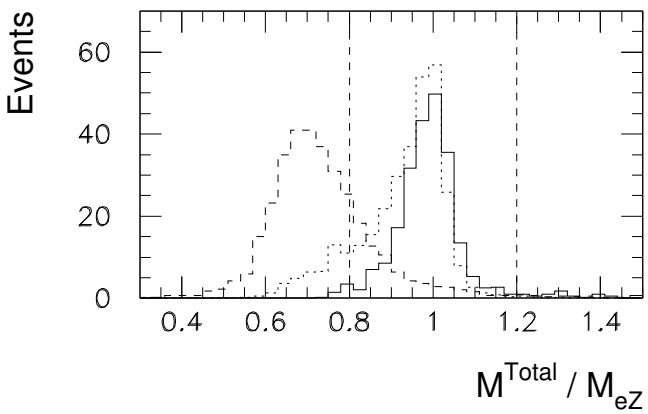

Figure 51: The distribution of the ratio M^{Total}/M_{eZ} for 125 GeV (solid histogram) and 225 GeV (dotted histogram) $e^*(\rightarrow e\,Z \rightarrow e\,q\,\bar{q}\,)$, and NC DIS Monte Carlo (dashed histogram). The accepted region is between the two dashed lines.

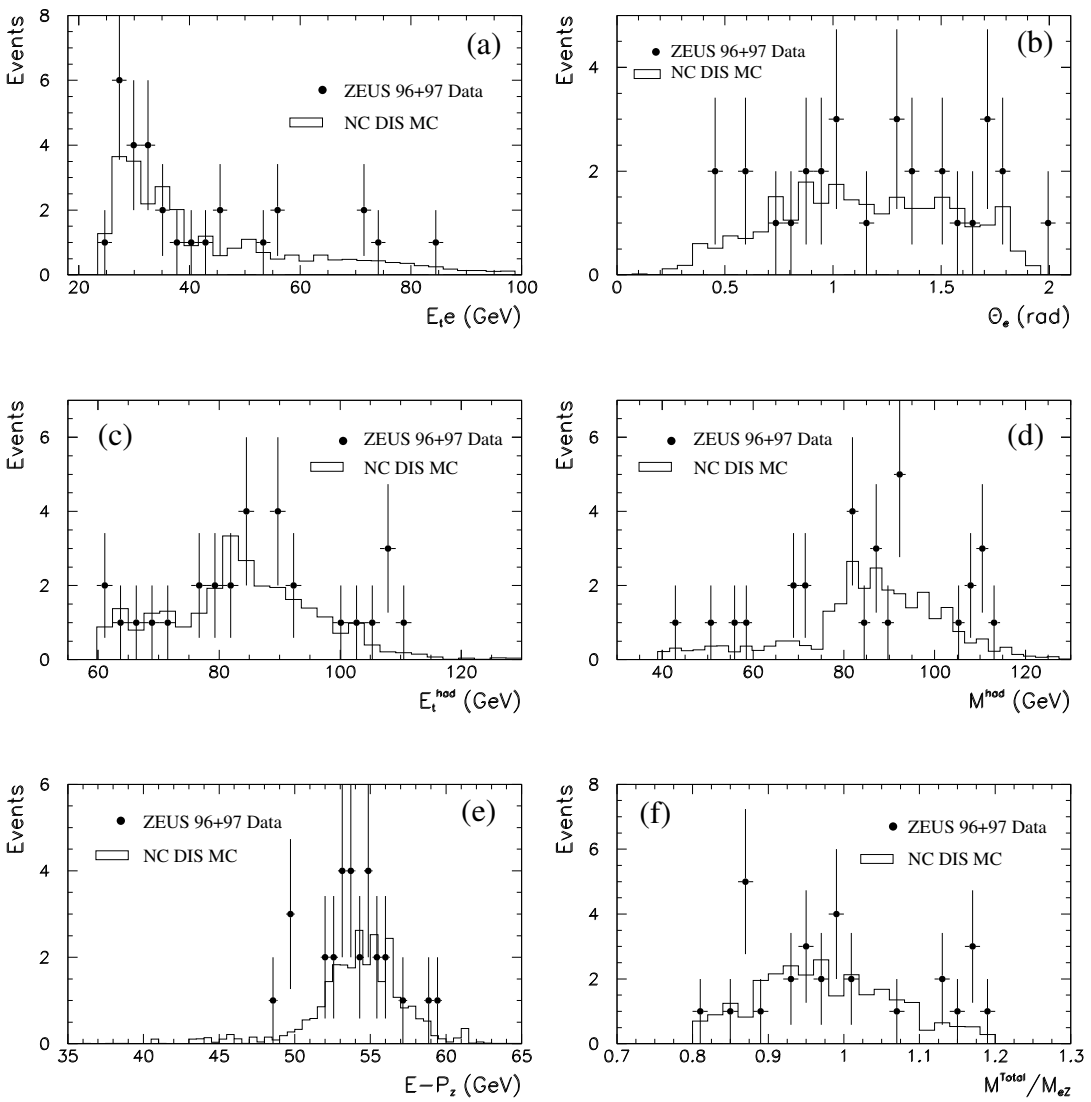

Figure 52: Comparison of data and NC DIS background Monte Carlo after all cuts in $eq\bar{q}$ search. Distribution of (a) the electron transverse energy, (b) the polar angle of the electron, (c) the hadronic transverse energy, (d) the hadronic mass, (e) the longitudinal energy $E-P_z$, and (f) the ratio M_{Total}/M_{eZ}, where M_{Total} is the total effective mass measured with the calorimeter.

Table 11: (a) Efficiency for $e^* \to eZ \to eq\bar{q}$ signal Monte Carlo analysis (the fraction of accepted events). The last line in the table shows the overall total efficiency, (b) the comparison between data and background Monte Carlo expectation. The table entries are the number of accepted events after each cut.

(a)

Cuts \ e^* Mass (GeV)	**125**	**150**	**175**	**200**	**225**	**250**
e^* Event Sample	78.9%	84.1%	88.0%	89.0%	91.1%	91.3%
$E_t^e > 25$ GeV	41.4%	73.0%	81.6%	84.8%	86.9%	87.7%
$\theta_e < 2$ rad	41.4%	73.0%	81.6%	84.8%	86.9%	87.7%
$35 < E - P_z < 65$ GeV	39.3%	69.7%	79.3%	82.8%	84.8%	86.1%
Hadronic Cut†	27.8%	47.7%	52.9%	57.0%	55.5%	52.9%
$0.8 < M^{Total}/M_{eZ} < 1.2$	26.7%	47.2%	52.9%	56.5%	54.5%	51.9%
Efficiency	**26.7%**	**47.2%**	**52.9%**	**56.5%**	**54.5%**	**51.9%**

(b)

Cuts	**Total BG**	**DATA**
e^* Event Sample	**55915.3**	**58098**
$E_t^e > 25$ GeV	**9883.5**	**9183**
$\theta_e < 2$ rad	**6064.8**	**5917**
$35 < E - P_z < 65$ GeV	**5956.4**	**5776**
Hadronic Cut†	**29.5**	**34**
$0.8 < M^{Total}/M_{eZ} < 1.2$	**26.5**	**29**

† Hadronic cut is defined as: either $E_t^{had} > 60$ GeV and $M^{had} > 80$ GeV or $E_t^{had} > 80$ GeV and $M^{had} > 40$ GeV.

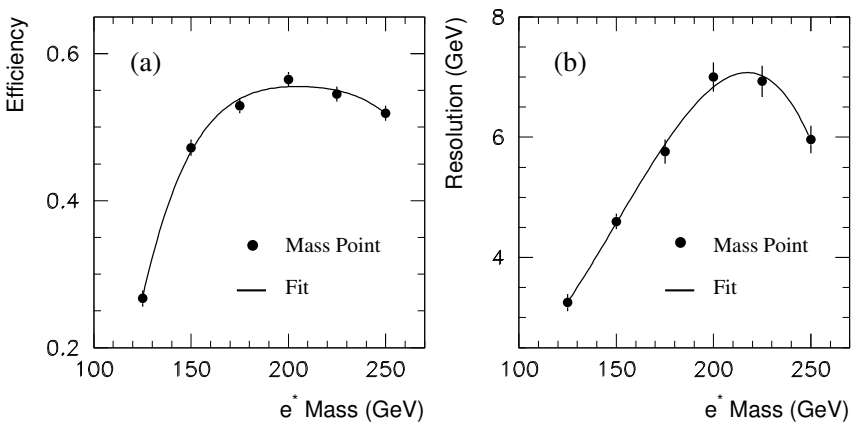

Figure 53: (a) Efficiency and (b) width of the reconstructed mass (mass resolution) for Monte Carlo $e^* \to eZ \to eq\bar{q}$ as a function of the mass of the excited electron. The smooth curves are polynomial fits to the points.

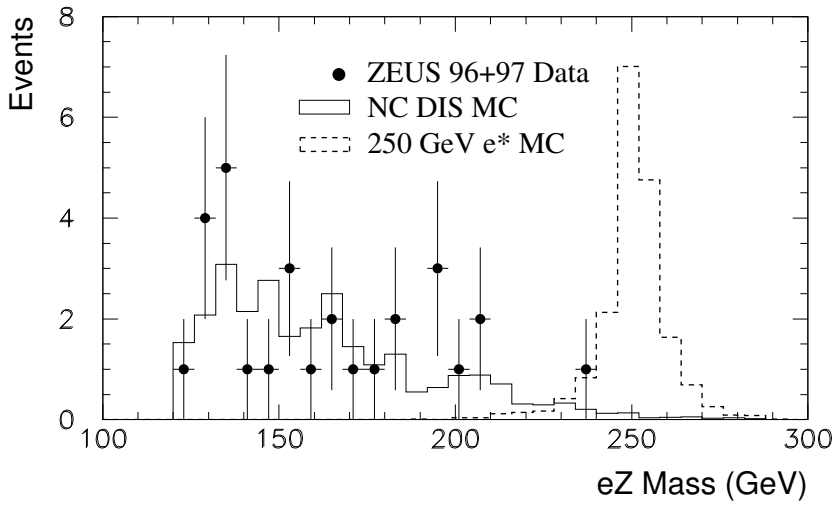

Figure 54: Invariant mass distribution of the eZ system for $e^* \to eZ \to eq\bar{q}$ after all cuts. The solid points show the 96+97 ZEUS data and the open histogram represents the expected total background from NC DIS Monte Carlo simulation. An example of a signal from e^* with a mass of 250 GeV is also shown as the dashed histogram.

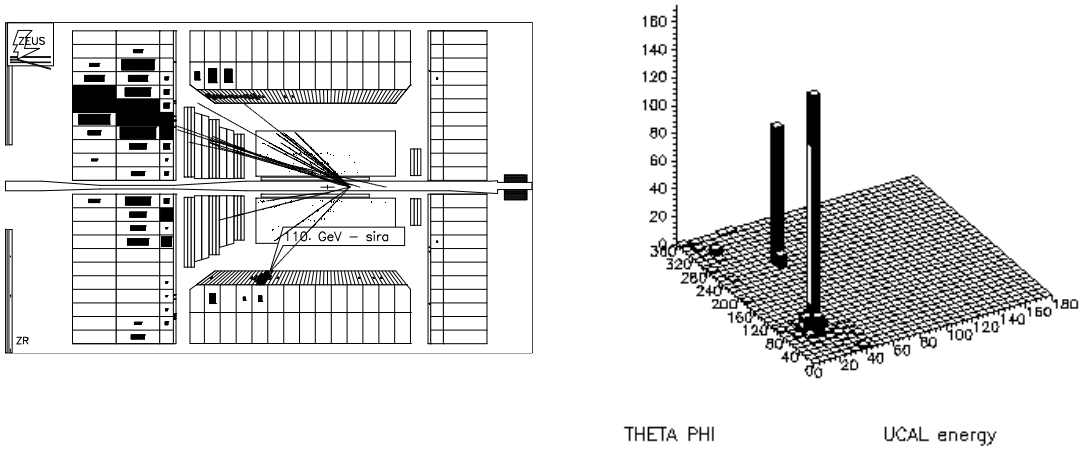

Figure 55: The highest mass candidate event for the $eq\bar{q}$ search. The $eq\bar{q}$ invariant mass is 235 GeV. The left part of the event display shows a vertical cut through the ZEUS detector. The final state electron (with a track) is in the BCAL and the jet in the forward direction. The right lego plot shows the distribution of transverse energy as a function of azimuth and polar angle.

10.3 $e\nu\bar{\nu}$ Resonance Search

The $e\nu\bar{\nu}$ final state could arise from

$$e^* \rightarrow e\,Z \rightarrow e\,\nu\,\bar{\nu}$$

or

$$e^* \rightarrow \nu\,W \rightarrow \nu\,\bar{\nu}\,e$$

decay modes.[22] A single high E_t electron in the detector is the signature for this decay mode; a low E_t recoil jet might appear in the detector as well. Events are expected to have high missing transverse momentum, Figure 56. The decay modes

$$e^* \rightarrow e\,Z \rightarrow e\,\nu_e\,\bar{\nu}_e\,, \quad e\,\nu_\mu\,\bar{\nu}_\mu\,, \quad \text{and} \quad e\,\nu_\tau\,\bar{\nu}_\tau$$

cannot be separated from each other.

[22] The branching ratio for $Z \rightarrow \nu\bar{\nu}$ is 20.01% and that of $W \rightarrow e\,\bar{\nu}$ is 10.9%.

Single W-production and NC DIS are the main backgrounds for this process, although CC DIS also contributes.

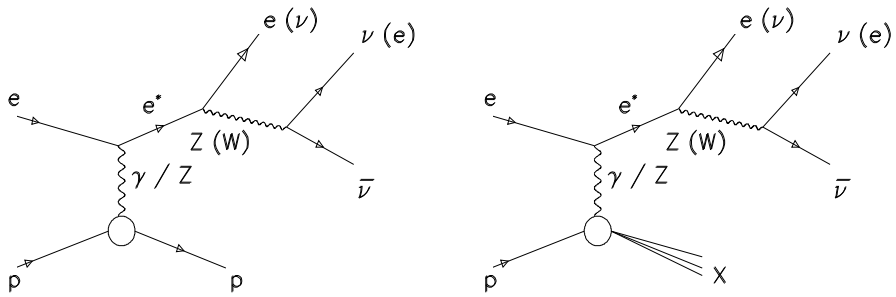

(a) (b)

Figure 56: Diagrams for the production and decay of excited electron $e^* \to eZ \to e\nu\bar{\nu}$ or $e^* \to \nu W \to \nu e\bar{\nu}$ via (a) elastic and (b) inelastic processes in ep collisions.

10.3.1 Final $e\nu\bar{\nu}$ Sample

Starting from the e^* event sample with at least an electromagnetic cluster we require:

- an isolated electron ($E_e^{iso}(R < 0.8) < 2$ GeV) with a transverse energy greater than 10 GeV, Figure 5. If its polar angle is less than 0.3 rad, the threshold is raised to 30 GeV. We also require one track matching with transverse momentum greater than 5 GeV within a distance of closest approach less than 10 cm. Sometimes the electron finder picks a high energy π^0 from the jets in CC DIS as an electromagnetic cluster.

- The electromagnetic cluster is required to have a polar angle less than 2 rad, Figure 6. In contrast to NC DIS, the separation of single W-production and of CC DIS events is very difficult, because the angular distribution of single

W-production and some of CC DIS events are boosted in forward direction like e^* events.

- The events are expected to be unbalanced in transverse energy, so the missing transverse momentum must be greater than 20 GeV. For further suppression of non-ep collisions, $P_t^{miss}(\theta > 10^o) > 20$ GeV, where the energy in a cone of 10^o around the forward beam pipe is excluded, Figure 7.

- Due to presence of neutrinos in the final state, there is no expectation that any recoil jet (if there is any) will be exactly back-to-back in ϕ with the electron. Consequently, we require

$$\cos(\phi_{\rm e} - \phi_{\rm had}) > -0.95$$

(so-called acoplanarity cut) if the hadronic transverse energy $E_{\rm t}^{\rm had}$ is larger than 2 GeV. $\phi_{\rm had}$ is the azimuthal angle for the hadronic system

$$\phi_{\rm had} = \tan^{-1}\left(\frac{\sum_i^{had} Pyi}{\sum_i^{had} Pxi}\right). \qquad (27)$$

Calorimeter cells within the forward 10° cone and those which belong to the electromagnetic shower are both excluded from the calculation of $E_{\rm T}^{\rm had}$ and $\phi_{\rm had}$. It can be seen from Figure 57 that the jet and the electron are back-to-back in the transverse plane and transverse momentum balances for most NC DIS events.

- We suppress NC DIS events by requiring $P_t^{miss}/E_t > 0.4$. All the calorimeter cells are assigned for the computation of both the vector sum P_t^{miss} and the scalar sum E_t, Figure 58. This requirement also rejects the spark events and the cosmic ray events that travel through the detector, produce a track, and deposit energy consistent with an electron in the calorimeter.

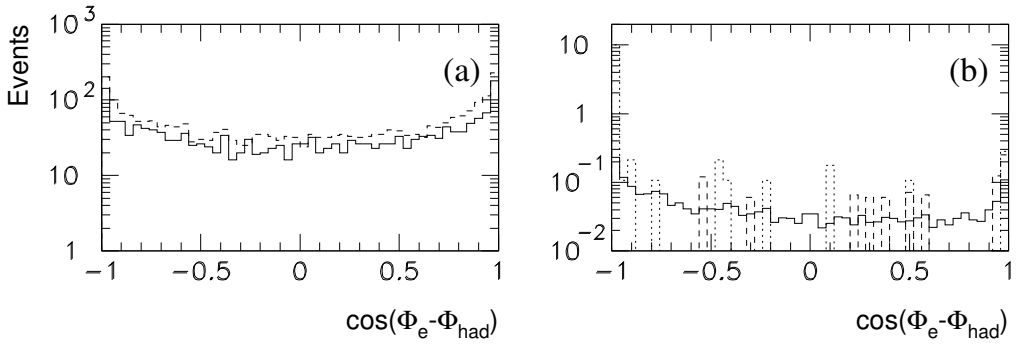

Figure 57: The distribution of $\cos(\phi_{\rm e} - \phi_{\rm had})$ after cuts on E_t, θ of the the electron and P_t^{miss}, for (a) 125 GeV (solid line) and 225 GeV (dashed line) $e^* \to eZ \to e\nu\bar{\nu}$. and for (b) single W-production (solid line), NC DIS (dotted line). and CC DIS (dashed histogram) Monte Carlo. The $\cos(\phi_{\rm e} - \phi_{\rm had})$ distribution for $e^* \to \nu W \to \nu e\bar{\nu}$ are similar to those in (a).

Figure 59 compares data and background Monte Carlo before applying the acoplanarity cut. At this stage 19 data events pass these selection criteria, in agreement with the Monte Carlo background estimation of 15.5 $\pm$ 1.1 events.

After applying all cuts only one event is observed with an expected background of 3.3 $\pm$ 0.5 events. The expected background from NC DIS, from W-production, and from CC DIS are expected to be 0.9 $\pm$ 0.2 events, 1.8 $\pm$ 0.5, and 0.6 $\pm$ 0.2 events respectively. The effects of the various cuts are listed in Tables 12 and 13.

The overall efficiency for $e^* \to e\,Z \to e\nu\bar{\nu}$ and $e^* \to \nu W \to e\nu\bar{\nu}$ is shown in Figures 60(a) and 61(a) as a function of mass for both analyses. It is above 70% for e^* mass greater than 150 GeV and increases to about 81% at $M_{e^*} = 250$ GeV in $e^* \to e\,Z \to e\nu\bar{\nu}$ decay channel, while it is lower in the $e^* \to \nu W \to e\nu\bar{\nu}$ decay mode, decreases from 70% at mass 125 GeV to 60% at 250 GeV mainly because the W or its decay products partially escape through the forward beam pipe.

To determine the $e\nu\bar{\nu}$ invariant mass, Eq. (25) is used (see Section 9.2) and the Gaussian mass resolution for the e^* Monte Carlo events ranges from 3.3 GeV to 9 GeV for $e^* \to e\,Z \to e\nu\bar{\nu}$ mode but it degrades from 10 GeV to 56 GeV for

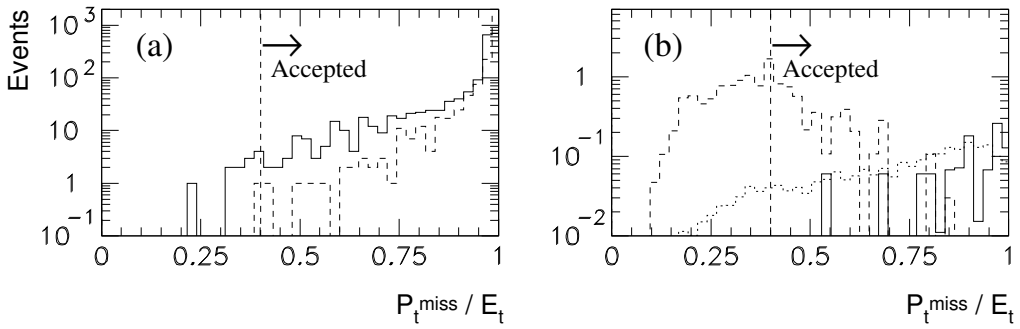

Figure 58: The distribution of P_t^{miss}/E_t after cuts on E_t, θ of the the electron and P_t^{miss}, for (a) 125 GeV (solid line) and 225 GeV (dashed line) $e^* \to eZ \to e\nu\bar{\nu}$. and for (b) single W-production (solid line), NC DIS (dotted line). and CC DIS (dashed histogram) Monte Carlo. The $\cos(\phi_{\rm e} - \phi_{\rm had})$ distribution for $e^* \to \nu W \to \nu e\bar{\nu}$ are similar to those in (a). The accepted events are to right of the vertical dashed lines.

$e^* \to \nu W \to e\nu\bar{\nu}$.

Figure 62 presents the invariant mass spectrum of the selected events and the Monte Carlo background prediction of 3.3 events. The expected lineshape for an example signal is also shown. No significant excess of events is observed in characteristic peak for e^* production. Figure 63 shows the event display of the single e^* candidate for this channel with an eZ invariant mass of 136 GeV.

The $e^* \to \nu W \to e\nu\bar{\nu}$ channel increases the efficiency in the νW by only 10% and its mass resolution degrades dramatically, so this channel was not included in the e^* search for setting the upper limit on the cross-section production times the branching ratio. Therefore candidates found in this channel are included in the eZ search.

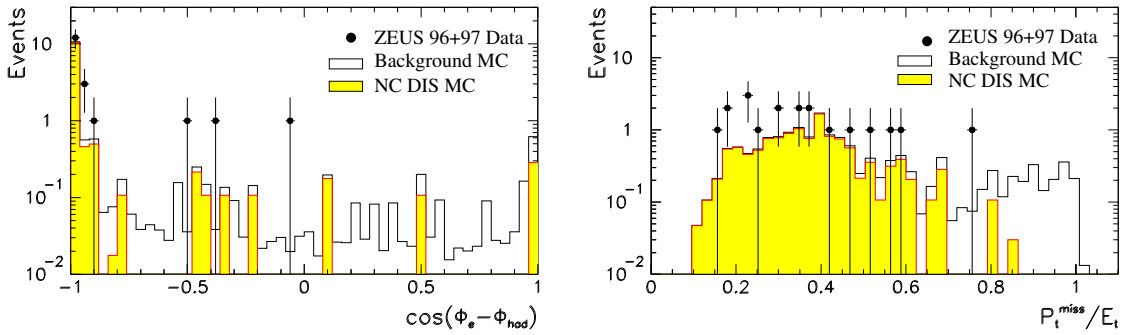

Figure 59: Comparison between data and background Monte Carlo before applying the acoplanarity cut in $e\nu\bar{\nu}$ search. Distribution of (a) $\cos(\phi_{\rm e} - \phi_{\rm had})$ and (b) P_t^{miss}/E_t. The solid points show the 96+97 ZEUS data and the open histogram represents the expected total background Monte Carlo simulation. The contribution from the NC DIS process is shown by the shaded histogram.

Table 12: (a) Efficiency for $e^* \to eZ \to e\nu\bar{\nu}$ signal Monte Carlo (the fraction of accepted events). The last line in the table shows the overall events accepted. (b) The comparison between data and background Monte Carlo expectation. The table entries are the number of accepted events after each cut.

(a)

Cuts \ e^* Mass (GeV)	**125**	**150**	**175**	**200**	**225**	**250**
e^* Event Sample	81.1%	85.8%	85.2%	86.0%	84.7%	86.0%
$\theta_e < 2$ rad	79.7%	80.4%	81.1%	82.3%	82.1%	83.6%
$p_t^{miss} > 20$ GeV	62.7%	79.7%	81.0%	82.3%	82.0%	83.5%
Acoplanarity cut†	61.2%	77.8%	79.0%	80.1%	80.0%	81.0%
$P_t^{miss}/E_t > 0.4$	60.9%	77.6%	78.9%	81.1%	80.0%	81.0%
Efficiency	**60.9%**	**77.6%**	**78.9%**	**81.1%**	**80.0%**	**81.0%**

(b)

Cuts	NC DIS	W	CC DIS	**Total bg**	**DATA**
e^* Event Sample	55350.4	3.6	1.9	**55355.9**	**57371**
$\theta_e < 2$ rad	11742.9	3.2	1.6	**11747.7**	**11970**
$p_t^{miss} > 20$ GeV	12.2	2.3	1.0	**15.5**	**19**
Acoplanarity cut†	1.9	2.1	1.0	**5.0**	**4**
$P_t^{miss}/E_t > 0.4$	0.9	1.8	0.6	**3.3**	**1**

† Acoplanarity cut is defined as: if $E_t^{had} > 2$ GeV then $\cos(\phi_e - \phi_{had}) >$ -0.95.

Table 13: Efficiency for $e^* \to \nu W \to \nu \bar{\nu} e$ signal Monte Carlo analysis (the fraction of accepted events). The last line in the table shows the overall total efficiency.

Cuts \ e^* Mass (GeV)	**125**	**150**	**175**	**200**	**225**	**250**
e^* Event Sample	78.7%	76.8%	74.4%	70.4%	65.9%	62.0%
$\theta_e < 2$ rad	75.1%	75.2%	73.6%	69.8%	65.7%	61.9%
$p_t^{miss} > 20$ GeV	72.0%	71.2%	67.9%	63.9%	60.3%	57.1%
Acoplanarity cut†	70.3%	69.0%	66.1%	62.1%	58.4%	55.9%
$P_t^{miss}/E_t > 0.4$	70.0%	68.8%	65.8%	62.0%	58.4%	55.9%
Efficiency	**70.0%**	**68.8%**	**65.8%**	**62.0%**	**58.4%**	**55.9%**

† Acoplanarity cut is defined as: if $E_t^{had} > 2$ GeV then $\cos(\phi_e - \phi_{had}) >$ -0.95.

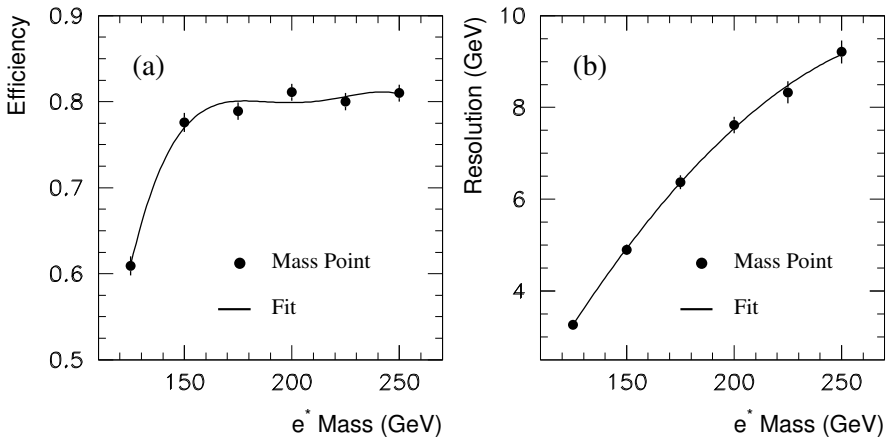

Figure 60: (a) Efficiency and (b) width of the reconstructed mass (mass resolution) for Monte Carlo $e^* \to eZ \to e\nu\bar{\nu}$ as a function of the mass of the excited electron. The smooth curves are polynomial fits to the points.

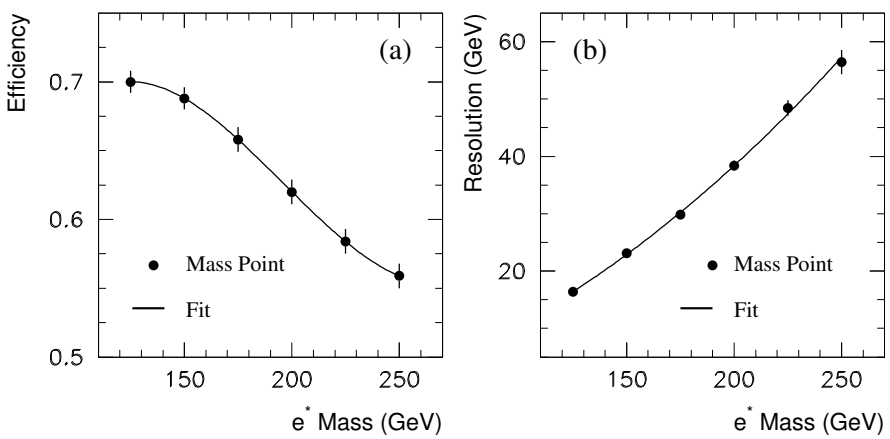

Figure 61: (a) Efficiency and (b) width of the reconstructed mass (mass resolution) for Monte Carlo $e^* \to \nu W \to \nu e\bar{\nu}$ as a function of the mass of the excited electron.

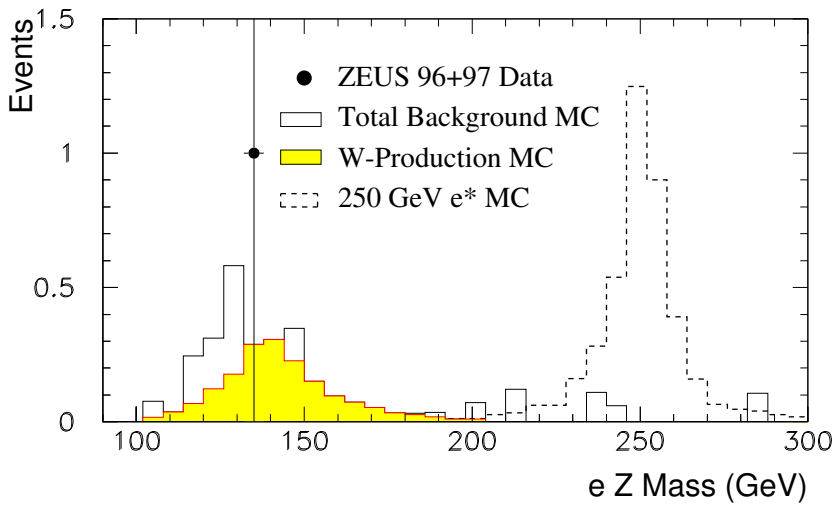

Figure 62: Invariant mass distribution of the eZ system for $e^* \to eZ \to e\nu\bar{\nu}$ after all cuts. The solid point show the 96+97 ZEUS data and the open histogram represents the expected total background and the darker histogram denotes the W-Production Monte Carlo simulation. An example of a signal from e^* with a mass of 250 GeV is also shown as the dashed histogram.

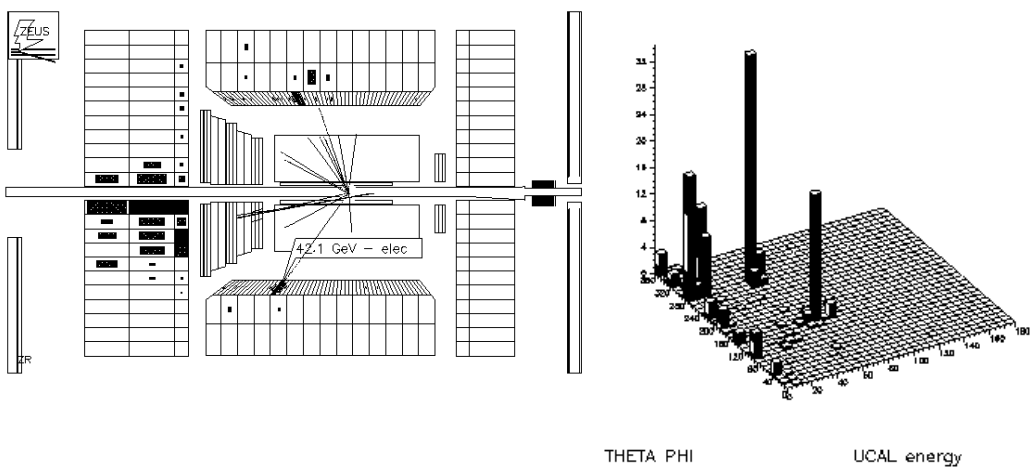

Figure 63: The single candidate event for the e $\nu\bar{\nu}$ search. The eZ invariant mass is 136 GeV. The left part of the event display shows a vertical cut through the ZEUS detector. The final state electron (with a track) is in the BCAL. The right lego plot shows the distribution of transverse energy as a function of azimuth and polar angle.

10.4 $\nu q\bar{q}'$ Resonance Search

The $\nu q\bar{q}$' final state would arise from the $e^* \to \nu W$ decay channel when the W decays hadronically.[23] For large e^* mass this decay mode dominates over other decay channels [14, 15] and it gives a good sensitivity for an e^* search in this region (branching ratio $> 40\%$ for $M_{e^*} > 150$ GeV).

The signature is characterized by large unbalanced transverse momentum with large hadronic transverse energy and large hadronic mass, Figure 64. The dominant background is multi-jet CC DIS, although NC DIS and photoproduction also contribute. The signal would manifest itself as a resonance peak in both the $\nu q\bar{q}'$ and hadronic invariant mass distributions with the latter near the W mass.

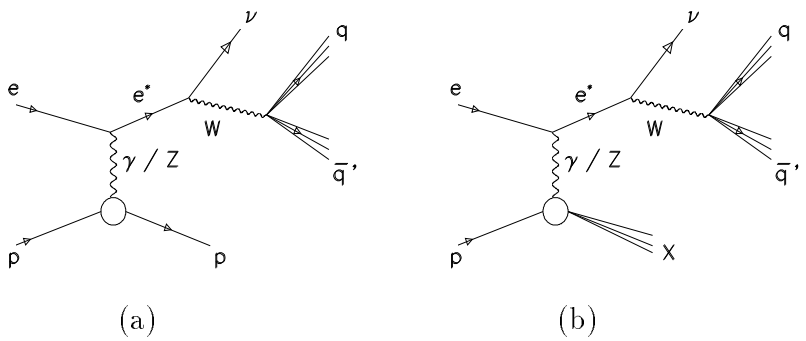

Figure 64: Diagrams for the production and decay of excited electron $e^* \to \nu W \to \nu q\bar{q}'$ via (a) elastic and (b) inelastic processes in ep collisions.

10.4.1 Final $\nu q\bar{q}'$ Sample

To separate the signal from the background, we start with the e^* event sample with no electromagnetic cluster in the final state. In each event:

- the missing transverse momentum $P_t^{miss}(\theta > 10^o)$, calculated excluding the

[23] The hadronic branching ratio of W boson is 67.8%.

energy in a cone of 10° around the forward beam pipe, is required to be greater that 25 GeV, Figure 7. This requirement removes most of the NC DIS and Photoproduction backgrounds which tend to have lower missing transverse momentum, but does not reject high P_t CC DIS events significantly, Figure 7.

- We require 10 GeV $< E - P_z <$ 45 GeV, Figure 8.

- In this decay the only energy observable in the detector is due to the hadronic decay of the W boson. The hadronic W decay is expected to produce large hadronic transverse energy (E_t^{had}) and hadronic mass (M^{had}), Figures 65.[24] Figure 66 presents the W mass resolution as well as a shift of mass from the nominal W mass as a function of e^* mass.

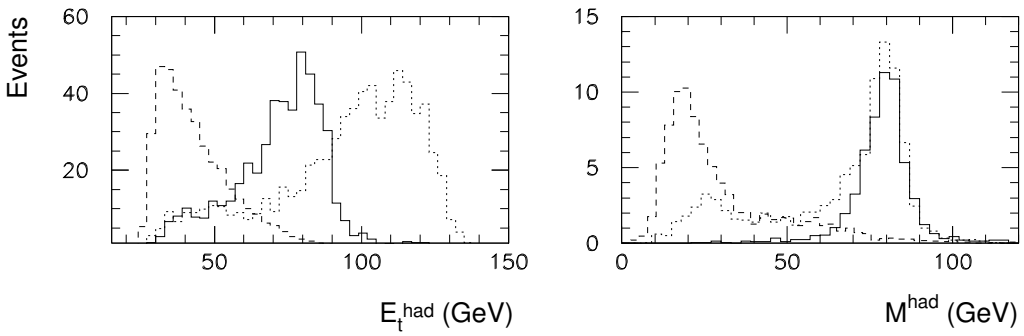

Figure 65: The distribution of (a) the hadronic transverse energy (E_t^{had}) after cuts on P_t^{miss} and $E - P_z$, for 125 GeV (solid line), 225 GeV (dotted line) $e^* \to \nu W \to \nu q\bar{q}'$, and CC DIS (dashed line) and (b) the hadronic mass (M^{had}) after cuts on P_t^{miss} and $E - P_z$, and requiring $E_t^{had} > 50$ GeV, for 125 GeV (solid line) and 225 GeV (dotted line) $e^* \to \nu W \to \nu q\bar{q}'$, and CC DIS (dashed line) Monte Carlo.

[24]Like the $eq\bar{q}$ channel, the tail toward lower hadronic mass at higher e^* masses is due to the loss of the hadrons from the decay of the W boson in the very forward region.

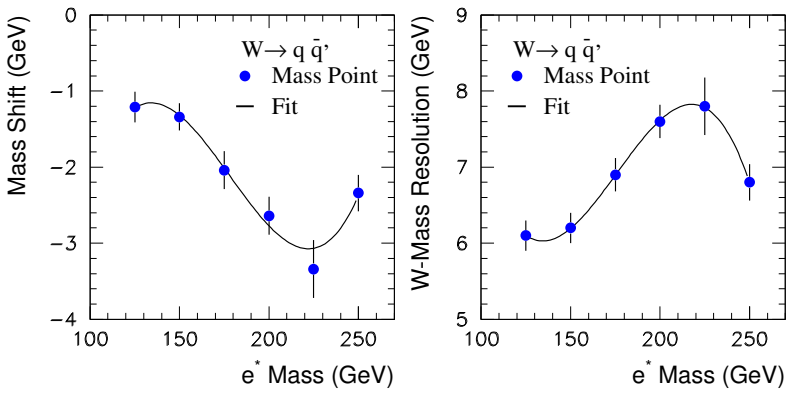

Figure 66: The reconstructed W mass resolution and the mass shift from the nominal W mass as a function of e^* mass. The smooth curves are polynomial fits to the points.

Events are accepted if either $E_t^{had} > 50$ GeV and $M_{had} > 60$ GeV or $E_t^{had} > 80$ GeV and $M_{had} > 40$ GeV. The latter cut provides good efficiency for high mass e^* events in which some of the hadrons from the decay of the W boson are lost in the very forward region, Figure 67.

Figure 68 shows the distribution after all cuts for data and Monte Carlo. These selections accept 10 events with an expected background of 10.6 ± 0.4 events. The estimation for the background from CC DIS is 8.9 events and the estimation from photoproduction is 1.7 events. The effect of the various cuts are listed in Table 14. The overall efficiency for $e^* \to \nu W \to \nu q' \bar{q}$ for masses above 150 GeV is greater than 46%.

To determine the νW invariant mass, Eq. (26) is used and the Gaussian mass resolution for the e^* Monte Carlo events ranges from 6 GeV to 8 GeV for e^* mass range 125 to 250 GeV, Figure 69(b).

Figure 70 shows the invariant mass spectrum of the 10 selected events compared with the Monte Carlo background prediction. The expected lineshape for an example signal is also shown. No significant excess of events is observed. Figure 71 shows the highest mass (211 GeV) candidate for the $\nu q \bar{q}'$ search.

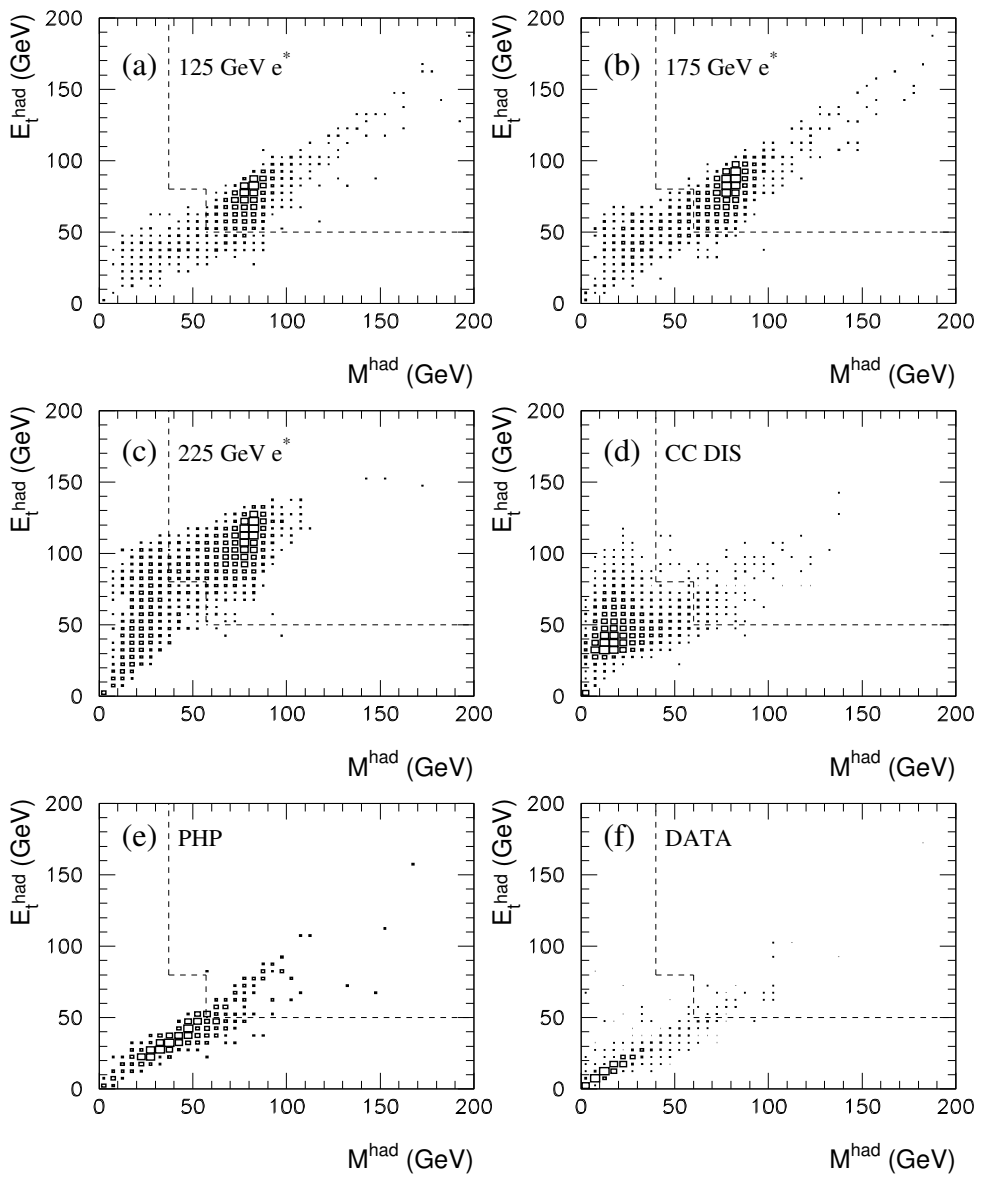

Figure 67: The distribution of the hadronic mass (M^{had}) versus the transverse hadronic energy (E_t^{had}) for (a) 125 GeV, (b) 175 GeV, (c) 225 GeV $e^* \to \nu W \to \nu q\bar{q}'$ signal Monte Carlo, (d) CC DIS, (e) Photoproduction, and (f) data. The dashed lines show the cut; the accepted region is to the upper right.

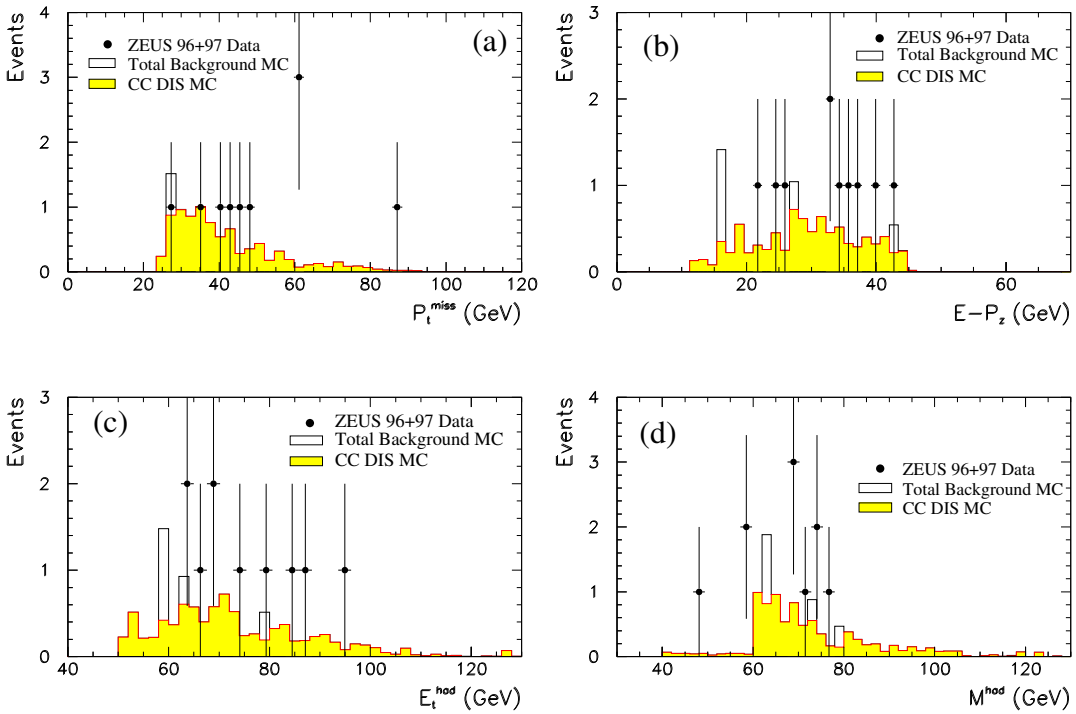

Figure 68: Comparison of data and background Monte Carlo (CC DIS + Photoproduction + NC DIS) after the all cuts in $\nu q\bar{q}'$. Distribution of (a) the missing transverse momentum, (b) the longitudinal energy $E - P_z$, (c) the hadronic transverse energy, (d) the hadronic mass.

Table 14: (a) Efficiency for $e^* \to \nu W \to \nu q\bar{q}'$ signal Monte Carlo analysis (fraction of accepted events). (b) The comparison between data and background Monte Carlo expectation. The table entries are the number of accepted events after each cut. The last line in the table shows the final sample,

(a)

Cuts \ e^* Mass (GeV)	**125**	**150**	**175**	**200**	**225**	**250**
e^* Event Sample	64.0%	72.0%	76.9%	71.8%	72.7%	69.8%
$p_t^{miss}(\theta > 10^o) > 25$ GeV	50.0%	60.0%	73.4%	56.6%	56.0%	53.3%
$10 < E - P_z < 45$ GeV	41.9%	53.6%	66.7%	52.1%	52.2%	47.6%
Hadronic Cut†	41.9%	53.6%	52.4%	51.9%	51.5%	46.8%
Efficiency	**41.9%**	**53.6%**	**52.4%**	**51.9%**	**51.5%**	**46.8%**

(b)

Cuts	CC DIS	PHP	NC DIS	**Total BG**	**DATA**
e^* Event Sample	108.7	9.5	3.0	**121.2**	**122**
$p_t^{miss}(\theta > 10^o) > 25$ GeV	104.3	1.7	< 0.04	**106.0**	**0.6**
$10 < E - P_z < 45$ GeV	91.0	1.7	< 0.01	**92.7**	**84**
Hadronic Cut†	8.9	1.7	< 0.01	**10.6**	**10**

† Hadronic cut is defined as: either $E_t^{had} > 50$ GeV and $M^{had} > 60$ GeV or $E_t^{had} > 80$ GeV and $M^{had} > 40$ GeV.

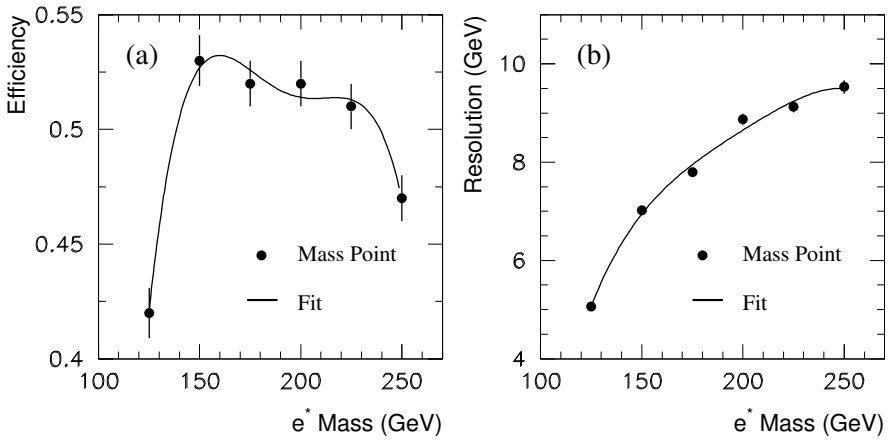

Figure 69: (a) Efficiency and (b) width of the reconstructed mass (mass resolution) for Monte Carlo $e^* \to \nu W \to \nu q\bar{q}$ as a function of the mass of the excited electron.

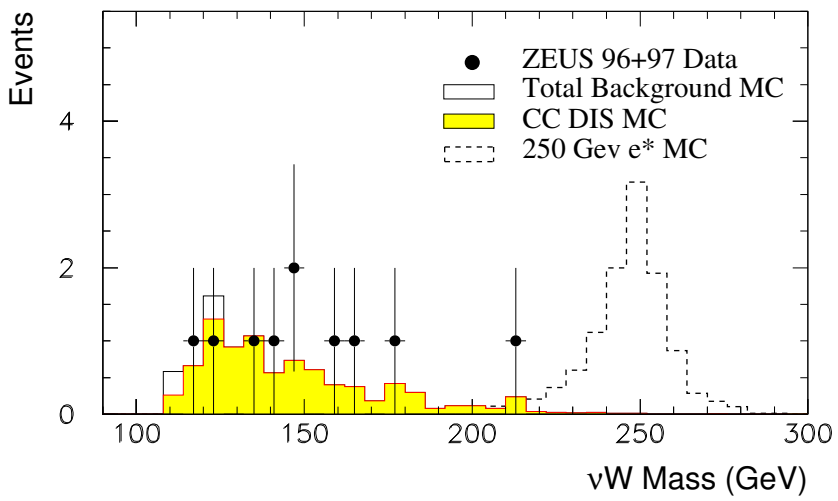

Figure 70: Invariant mass distribution of the νW system for $e^* \to \nu W \to \nu q\bar{q}'$ after all cuts. The solid points show the 96+97 ZEUS data and the open histogram represents the expected total background and the shaded histogram denotes the CC DIS Monte Carlo simulation. An example of a signal from e^* with a mass of 250 GeV is also shown as the dashed histogram.

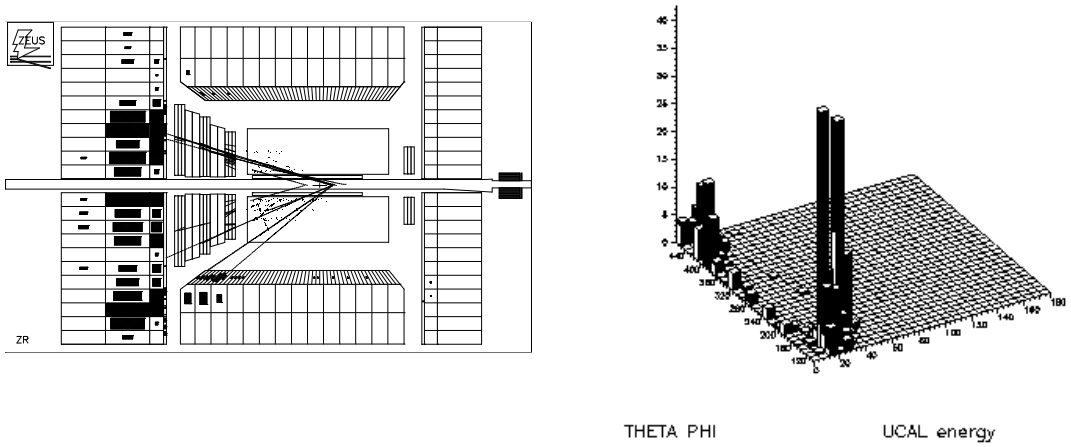

Figure 71: The highest mass candidate event for the $\nu q\bar{q}'$ search. The νW invariant mass is 211 GeV. The left part of the event display shows a vertical cut through the ZEUS detector. The jets are boosted in the forward direction. The right lego plot shows the distribution of transverse energy as a function of azimuth and polar angle.

Chapter 11

Search for Excited Neutrino

After the 1997/1998 break, HERA was operated with 920 GeV protons and 27.5 GeV electrons corresponding to a center-of-mass energy of 318 GeV. This new e^-p data collected in 1998 and 1999 gives higher sensitivity for the ν^* searches compared to the e^+p data set, see Section 2.2. Therefore, it is natural to extend the main e^* analysis to include the ν^* search with new data.

The excited neutrinos are searched for in the channel $\nu^* \rightarrow \nu\gamma$, because the clean and relatively background-free signature offers a good discovery potential. The data sample used for this analysis has an integrated luminosity of 16.7 pb^{-1} corresponding to a 30-fold increase in statistics over the previously published study with e^-p data from ZEUS [13].

The main signature for $\nu^* \rightarrow \nu\gamma$ is an isolated photon in events with high missing P_t. Due to the W boson exchange some hadronic activity is expected from the breakup of the proton. The main background is CC DIS with isolated π^0 decays, Figure 72.

To separate the signal from the background, the same sequence of cuts described in Chapter 7 is applied to the 1998-99 data sample. Furthermore, by applying the requirements of Section 8.1, without requiring a track associated with the electromagnetic cluster, we establish a ν^* event sample with at least one

electromagnetic cluster in the final state.

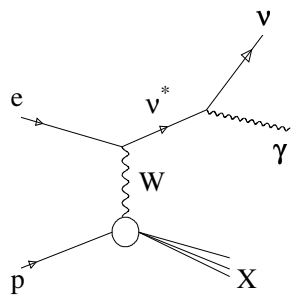

Figure 72: Diagram for the production and decay of excited neutrino $\nu^* \to \nu\gamma$ in ep collisions.

For this channel, the sum of the calorimeter energy, within an $\eta - \phi$ cone of radius 0.8 which is centered on the cluster and not associated with the electromagnetic cluster, should be less than 5 GeV, Figure 73, a smaller energy cut than used in the other searches. The discrepancy between data and Monte Carlo is due to CC events with an energetic π^0 in the forward direction which is misidentified as an electromagnetic cluster.

At this stage the number of remaining events in the ν^* event sample sample is 26797 for an estimated Monte Carlo background of 27479.5 events. The estimation for the background from NC DIS is 27465.9 events and the estimation from CC DIS is 13.6 events. The efficiency for the $\nu^* \to \nu\gamma$ signal Monte Carlo events for all masses is above 70%.

Figure 74 shows the distributions of the background Monte Carlo and data with an electromagnetic cluster in the final state after the ν^* event sample cuts (the background Monte Carlo is normalized to the total 98+99 integrated luminosity of 16.7 pb^{-1}).

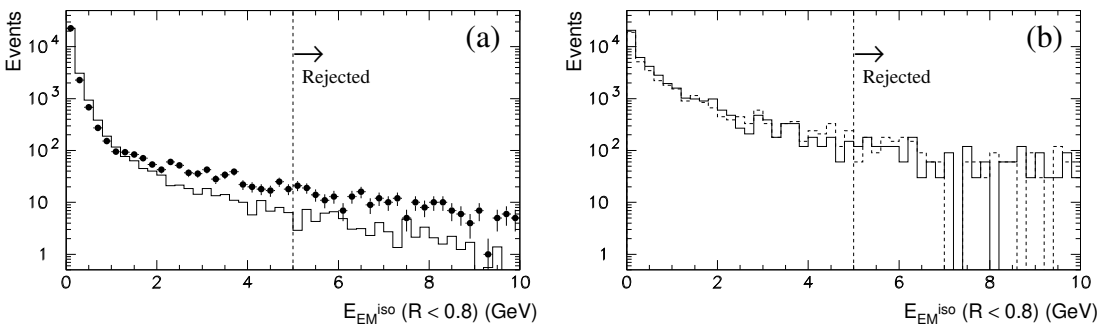

Figure 73: The distribution of the energy in an $\eta - \phi$ cone of radius 0.8 that is not assigned to the electromagnetic cluster candidate, $E_{EM}^{iso}(R < 0.8)$, for (a) data (solid black pont) and total background (open histogram) Monte Carlo, and for (b) 125 GeV (solid line) and 225 GeV (dashed line) $\nu^* \to \nu\gamma$. The rejected events are to the right of the dashed vertical lines.

11.1 ν^* Mass Reconstruction

The mass of the excited neutrino can be determined from the invariant mass of the photon and the neutrino,

$$M_{\nu\gamma}^2 = (E_\nu + E_\gamma)^2 - (P_{\nu x} + P_{\gamma x})^2 - (P_{\nu y} + P_{\gamma y})^2 - (P_{\nu z} + P_{\gamma z})^2 \,. \qquad (28)$$

The transverse momentum components of the neutrino ($P_{\nu x}$, $P_{\nu y}$) are obtained from the P_t vector measured by the calorimeter

$$P_{\nu x} = -P_x \quad \text{and} \quad P_{\nu y} = -P_y,$$

and the longitudinal component ($P_{\nu z}$) and neutrino energy (E_ν) are calculated assuming that $E - P_z = 2E_e^b$ for the event (see Appendix B.4),

$$E_\nu = \frac{1}{2}\left[\frac{P_t^{miss}}{2\,E_e^b - (E - P_z)} + 2\,E_e^b - (E - P_z)\right],$$

and

$$P_{z\nu} = \frac{1}{2}\left[\frac{P_t^{miss}}{2\,E_e^b - (E - P_z)} - 2\,E_e^b + (E - P_z)\right].$$

11.2 Final $\nu\gamma$ Sample

To separate the signal from the background we apply the following cuts:

- We raise the minimum requirement of transverse energy (E_t^{EM}) of the electromagnetic cluster to greater than 20 GeV. Furthermore, if its polar angle is less than 0.3 rad, the threshold is raised to $E_t^{EM} > 30$ GeV, Figure 5.
- A polar angle of less than 2 rad is required for the electromagnetic cluster, Figure 6.
- The presence of a neutrino is inferred by requiring a missing transverse momentum $P_t^{miss} > 25$ GeV, Figure 7.
- NC DIS events are suppressed by requiring $E - P_z < 45$ GeV.
- A total transverse energy greater than 50 GeV is required.
- The absence of a CTD track pointing to the EM cluster was demanded.

The effects of the various cuts are listed in Table 15. The mass resolution is approximately 5 GeV and the signal efficiency ranges from 56% for $M_{\nu^*} = 100$ GeV up to 68.5% for $M_{\nu^*} = 250$ GeV, Figure 75.

Only two events survive the selection cuts compared to a Standard Model expectation of 1.8 ± 0.2 events, with approximately half above 100 GeV. The invariant masses calculated for the two candidates are 101 GeV and 118 GeV. Figure 76 shows the invariant mass spectrum of the two selected events compared with

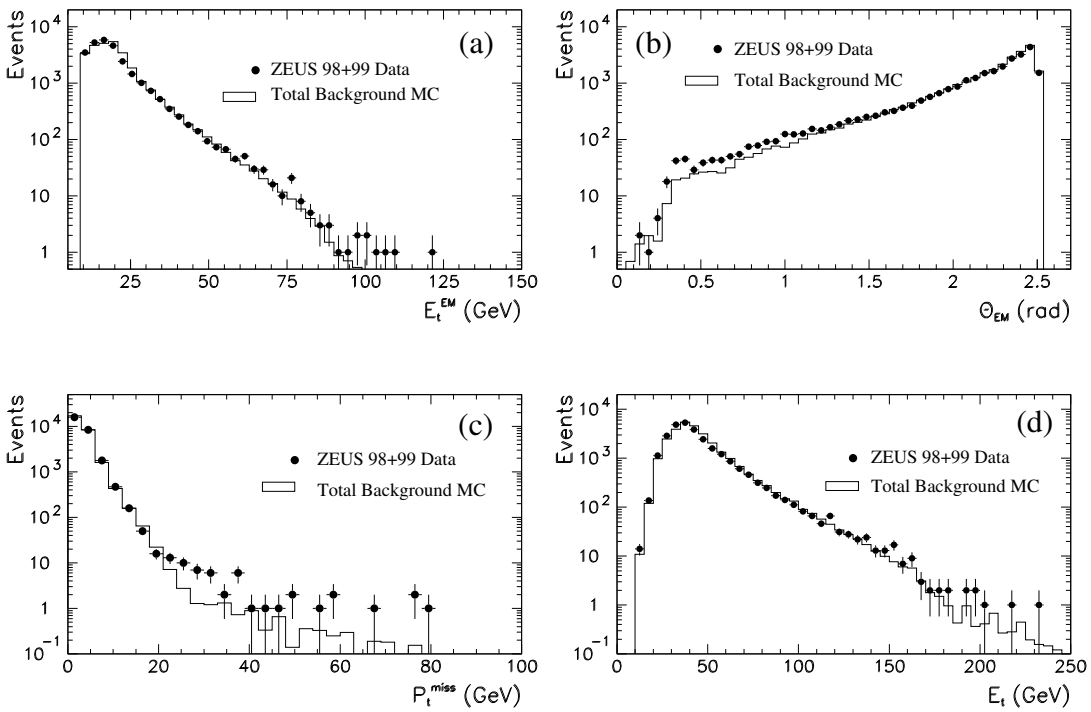

Figure 74: Comparison of data and total background Monte Carlo with an electromagnetic cluster in the final state after the ν^* event sample cuts. Distribution of (a) the transverse energy of the electromagnetic cluster (E_t^{EM}), (b) the polar angle of the electromagnetic shower (θ_{EM}), (c) the transverse missing momentum P_t^{miss}, and (d) the total transverse energy in the calorimeter (E_t). The solid points show the 98+99 ZEUS data and the open histogram represents the expected total background from NC DIS and CC DIS Monte Carlo events.

the Monte Carlo background prediction. The expected lineshape for an example signal is also shown. No significant excess of events is observed. Figure 77 shows the highest mass candidate for the $\nu\gamma$ search.

Table 15: (a) Efficiency for $\nu^* \to \nu\gamma$ signal Monte Carlo analysis (fraction of accepted events). The last line in the table shows the overall total efficiency. (b) The comparison between data and background Monte Carlo expectation. The table entries are the number of accepted events after each cut.

(a)

Cuts \ ν^* Mass (GeV)	**100**	**125**	**150**	**200**	**225**	**250**
ν^* Event Sample	72.1%	73.0%	72.5%	71.5%	70.7%	72.5%
$E_t^{EM} > 20$ GeV†	71.9%	73.0%	72.5%	71.5%	70.7%	72.5%
$\theta_{EM} < 2$ rad	71.9%	72.7%	72.5%	71.5%	70.7%	72.5%
$P_t^{miss} > 25$ GeV	60.4%	67.3%	68.9%	71.0%	69.4%	72.4%
$E - P_z < 45$ GeV	56.8%	62.1%	64.1%	67.0%	66.3%	69.1%
$E_t > 50$ GeV	56.4%	61.5%	63.6%	66.6%	65.9%	68.5%
EM with no Track	56.4%	61.5%	63.6%	66.7%	65.9%	68.5%
Efficiency	**56.4%**	**61.5%**	**63.6%**	**66.7%**	**65.9%**	**68.5%**

(b)

Cuts	CC DIS	NC DIS	**Total BG**	**DATA**
ν^* Event Sample	13.6	27465.9	**27479.5**	**26797**
$E_t^{EM} > 20$ GeV†	6.3	10709.5	**10715.8**	**8830**
$\theta_{EM} < 2$ rad	6.1	3832.0	**3838.1**	**3818**
$P_t^{miss} > 25$ GeV	5.3	2.1	**7.4**	**9**
$E - P_z < 45$ GeV	4.9	0.5	**5.4**	**7**
$E_t > 50$ GeV	2.7	0.4	**2.7**	**4**
EM with no Track	1.8	< 0.01	**1.8**	**2**

† Including the isolation requirement for the electromagnetic cluster.

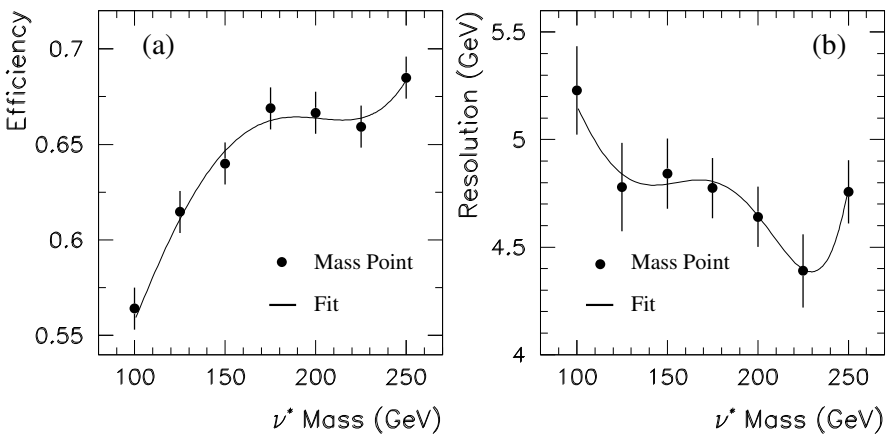

Figure 75: (a) Efficiency and (b) width of the reconstructed mass (mass resolution) for Monte Carlo ν^* events decaying into $\nu\gamma$ as a function of the mass of the excited electron.

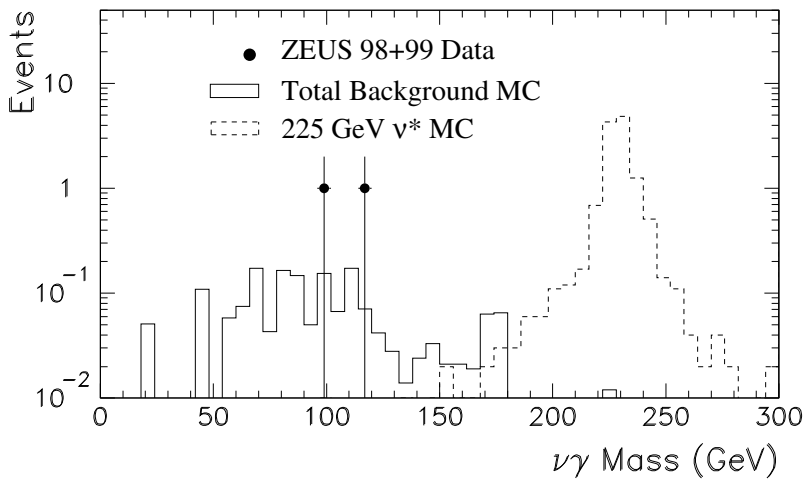

Figure 76: Invariant mass distribution of the $\nu\gamma$ system for $\nu^* \to \nu\gamma$ after all cuts. The solid points show the 98+99 ZEUS data and the open histogram represents the expected total background from CC DIS and NC DIS Monte Carlo events. An example of a signal from ν^* with a mass of 225 GeV is also shown as the dashed histogram.

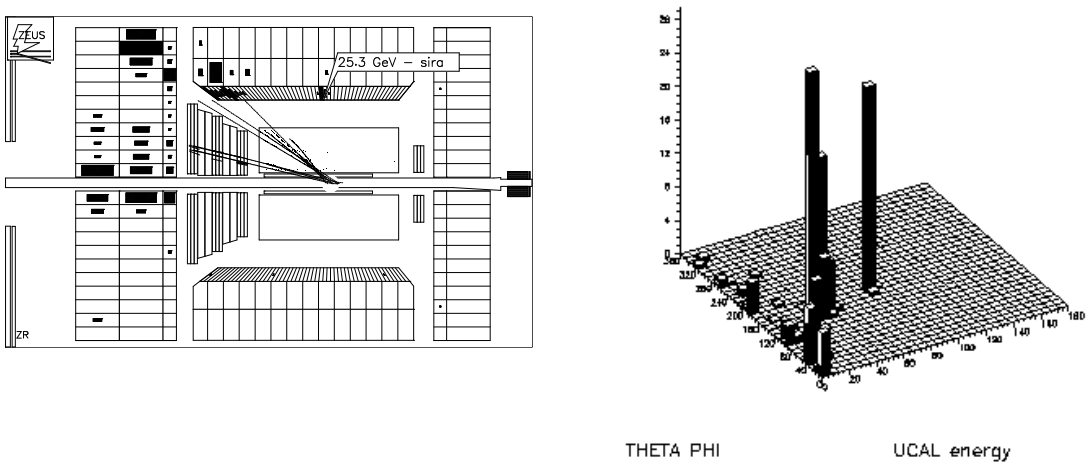

Figure 77: The highest mass candidate event for the $\nu\gamma$ search. The $\nu\gamma$ invariant mass for this event is 118 GeV. The left part of the event display shows a vertical cut through the ZEUS detector. The final state photon is in the BCAL and the jet in the forward direction. The right lego plot shows the distribution of transverse energy as a function of azimuth and polar angle.

Chapter 12

Systematic Uncertainties

The systematic uncertainty in the derivation of the upper limits for excited electron and neutrino production has been estimated as 18% and 14.4%, respectively. The contributions of the experimental uncertainties are 10.9% and 15.4% for ν^* and e^*, respectively, and that of the theoretical uncertainties is 9.4%. However, to estimate the total systematic uncertainty, we add them in quadrature.

Our evaluation of the systematic uncertainties is discussed in more detail in the following sections.

12.1 Experimental Uncertainties

Any experimental measurement is subject to systematic uncertainties. Our discussion in this section will be concerned with this topic.

- **Luminosity:** The systematic uncertainty on the measured luminosity depends on the efficiency of the luminosity detector and how much background from electron-gas interaction reaches the luminosity detectors. The systematic uncertainty of the combined 1996 and 1997 e^+p data sample is estimated to be less than 1.6% and that of the combined 1998 and 1999 is 2.5%. These numbers come from the ZEUS luminosity group.

- **Electromagnetic cluster identification:** The variation in efficiency between the two electron finders EM and SINISTRA is an estimate of the uncertainty on electromagnetic cluster identification and this variation is found to be less than 5% [42].

- **Energy Scale of the Calorimeter:** The energy scale of the calorimeter is uncertain at the 3% level, according to thorough studies made in [43, 49]. This leads to variations in the excited fermion efficiency ($\Delta\epsilon$) of 2.7% or less, Table 16.

Table 16: The sensitivity of event selection to the energy scale of the calorimeter for e^* and ν^* decay channels.

F^* **Mass(GeV)**	**125**	**150**	**175**	**200**	**225**	**250**
$e^* \to e\gamma$						
Max $\Delta\epsilon$	$\sim$ 1%	$\sim$ 1%	$\sim$ 1%	$\sim$ 1%	1.1%	1.0%
$e^* \to eZ \to eq\bar{q}$						
Max $\Delta\epsilon$	2.6%	2.7%	2.6%	1.6%	1.0%	1.0%
$e^* \to eZ \to e\nu\bar{\nu}$						
Max $\Delta\epsilon$	1.8%	$\sim$ 1%	$\sim$ 1%	$\sim$ 1%	$\sim$ 1%	$\sim$ 1%
$e^* \to \nu W \to \nu q\bar{q}'$						
Max $\Delta\epsilon$	2.4%	1.6%	1.2%	1.0%	1.0%	1.0%
$\nu^* \to \nu\gamma$						
Max $\Delta\epsilon$	1.8%	1.4%	1.4%	1.0%	1.4%	1.1%
Max $\Delta\epsilon = 2.7\%$						

- **Fitting Procedure:** There is a possibility of a systematic error introduced by the interpolation between generated Monte Carlo F^* mass points. The major effect is due to the calculation of the upper limit curves, which requires

a smooth parameterization of the F^* efficiency and resolution. This error was estimated to be 5%.

- **Background Estimation:** The overall uncertainty on the number of events expected from Monte Carlo is estimated to be 45% (10%) in the e^* (ν^*) search by using the MEPS and Ariadne programs. This is translated into a 12.5% (6%) variation in the obtained e^* (ν^*) upper limit.

- **Vertex Reconstruction:** Through variation of the cut on the vertex along z (nominally $\pm$50 cm) from $\pm$35 cm to $\pm$65 cm, an evaluation of the sensitivity of the event selection to the vertex reconstruction and underlying vertex distribution has been made [12]. This variation leads to less than a 3% change in the efficiency ($\Delta\epsilon$). Table 17 shows the sensitivity of event selection to vertex position cuts for different F^* decay channels.

Table 17: The sensitivity of event selection to vertex position cuts for excited electron and neutrino decay channels.

F^* Mass (GeV)	**125**	**150**	**175**	**200**	**225**	**250**
$e^* \to e\gamma$						
$\Delta\epsilon(\pm 35$ cm)	1.0%	2.8%	2.2%	1.6%	1.6%	1.6%
$\Delta\epsilon(\pm 65$ cm)	2.8%	1.1%	1.1%	1.7%	1.4%	2%
$e^* \to eZ \to eq\bar{q}$						
$\Delta\epsilon(\pm 35$ cm)	1.0%	1.1%	2%	1.7%	1.7%	1.9%
$\Delta\epsilon(\pm 65$ cm)	1.0%	1.8%	1.4%	1.4%	1.4%	1.4%
$e^* \to eZ \to e\nu\bar{\nu}$						
$\Delta\epsilon(\pm 35$ cm)	2.1%	2.8%	2.3%	2.5%	2.2%	3.0%
$\Delta\epsilon(\pm 65$ cm)	1.1%	2%	1.9%	2.0%	1.6%	1.7%
$e^* \to \nu W \to \nu q\bar{q}'$						
$\Delta\epsilon(\pm 35$ cm)	1.0%	1.4%	1.6%	2.0%	1.0%	1.0%
$\Delta\epsilon(\pm 65$ cm)	1.9%	1.5%	1.7%	2.0%	1.8%	2.2%
$e^* \to \nu W \to \nu\bar{\nu}e$						
$\Delta\epsilon(\pm 35$ cm)	2.3%	2.0%	2.0%	1.9%	1.7%	1.6%
$\Delta\epsilon(\pm 65$ cm)	1.7%	1.5%	1.2%	1.5%	1.2%	1.3%
$\nu^* \to \nu\gamma$						
$\Delta\epsilon(\pm 35$ cm)	2.1%	2.8%	2.9%	2.2%	3.0%	2.1%
$\Delta\epsilon(\pm 65$ cm)	1.8%	1.5%	2.0%	2.2%	1.7%	1.6%

- The main contribution is due to energy-momentum threshold cuts of the E_t^e, $E - P_z$, E_t^{had}, M^{had}, and P_t^{miss} variables. The level of these cuts is uncertain at the level of the energy scale uncertainty, 3% [43, 49]. Table 18 shows the effects of varying the selection cuts by 3% on the signal Monte Carlo. The effects are found to be at most 3%.

Table 18: The effects of varying the selection cuts on efficiency ($\Delta\epsilon$) for e^* and ν^* decay channels.

F^* Mass (GeV)	**125**	**150**	**175**	**200**	**225**	**250**
$e^* \to e\gamma$						
$\Delta\epsilon$	1.2%	1.1%	$< 1\%$	$< 1\%$	1.1%	1.0%
$e^* \to eZ \to eq\bar{q}$						
$\Delta\epsilon$	3.0%	2.7%	2.6%	1.6%	1.1%	1.1%
$e^* \to eZ \to e\nu\bar{\nu}$						
$\Delta\epsilon$	1.8%	1.0%	$< 1\%$	$< 1\%$	$< 1\%$	$< 1\%$
$e^* \to \nu W \to \nu q\bar{q}'$						
$\Delta\epsilon$	2.7%	1.6%	1.2%	$< 1\%$	1.0%	$< 1\%$
$\nu^* \to \nu\gamma$						
$\Delta\epsilon$	1.8%	1.4%	1.4%	1.0%	1.4%	1.1%

Assuming that the various systematic uncertainties are uncorrelated, we add them in quadrature, giving an overall experimental systematic uncertainty of 10.9% and 15.4% for ν^* and e^*, respectively. Table 19 summarizes the contributions of main sources to the experimental uncertainties.

Table 19: Contribution to the overall experimental uncertainties. The values in paretheses are the experimental uncertainties for e^*.

Source	**Uncertainty (%)**
Luminosity Measurement	2.5 (1.6)
Electromagnetic Cluster Identification	5 (5)
Energy Scale of the Calorimeter	2.7 (2.7)
Fitting Procedure	5 (5)
Vertex Reconstruction	3 (3)
Selection Cuts	3 (3)
Background Estimation	6 (12.5)
Overall Experimental Uncertainty	**10.9 (15.4)**

12.2 Theoretical Uncertainties

The theoretical uncertainties evaluated in the earlier excited fermion search by ZEUS [13] based on the 1993 data are used in this analysis. These are:

- **Radiative Corrections and Parton Density**: The initial state radiation gives a tail in the mass peak and leads to a systematic uncertainty in the production mechanism of the excited electron. The contribution due to radiative corrections to the excited fermion production model, as well as the uncertainty associated with the parton density distributions that are used to model the proton, has an 8% uncertainty.

- **Angular decay distribution**: Through comparison of the efficiency between isotropic decays and those with a $1 + \cos\theta$ (θ is the polar angle between the incoming and outgoing leptons) dependence for the decay boson, the model dependence of the excited fermion angular decay distribution is estimated to be less than 5%.

Therefore, the overall theoretical systematic uncertainty is estimated to be 9.4%.

Chapter 13

Limit Setting Procedure

In the absence of any observed signal for excited electrons and neutrinos in any of the studied searches described in Chapters 10 and 11, the data are used to set an upper limit (U.L.) as a function of the excited electron or neutrino mass, M_F^*, on the production cross-section times branching ratio

$$(\sigma \times BR)_{\text{U.L.}} = \frac{N_{\text{U.L.}}(M_F^*)}{\epsilon(M_F^*).\mathcal{L}}. \tag{29}$$

$\mathcal{L}$ is the integrated luminosity, and $\epsilon(M_F^*)$ is the parameterized efficiency for the excited electron/neutrino decay as a function of the e^*/ν^* mass, including, when appropriate, the branching fraction of the Z or W decay. The upper limit on the number of signal events, $N_{\text{U.L.}}$ is calculated at the 95% confidence level as a function of mass according to an unbinned likelihood technique after accounting for systematic errors [12, 13].

In each channel, $N_{\text{U.L.}}$ is determined using Poisson statistics from the number of events observed, and the expected number of background events. The Poisson likelihood of observing n events is given by the following expression:

$$\sum_{j=0}^{n} \left(\frac{\mu_s^j \, e^{-\mu_s}}{j!} \right) \left(\frac{\mu_b^{n-j} \, e^{-\mu_b}}{(n-j)!} \right) = \frac{1}{n!} \, e^{-(\mu_s+\mu_b)} \, (\mu_s + \mu_b)^n \, , \tag{30}$$

where μ_s is the average number of signal events and μ_b is the average number of background events. A systematic error from uncertainties in the efficiency,

luminosity, and background can be included by convoluting a Gaussian with the Poisson likelihood:

$$\mathcal{P}(\mu_s;\, n, \mu_b) \;=\; \int \frac{d\gamma}{\sqrt{2\pi}\delta} \exp\left[-\frac{(\gamma-1)^2}{2\delta^2}\right] \;\frac{1}{n!}\, e^{-\gamma(\mu_s+\mu_b)}\, (\gamma\mu_s + \gamma\mu_b)^n\,, \qquad (31)$$

where δ is the fractional systematic uncertainty.

The upper limit on μ_s at the 95% confidence level, $N_{\text{U.L.}}$, is then obtained by solving the equation:

$$\int_0^{N_{\text{U.L.}}} \mathcal{P}(\mu_s;\, n, \mu_b)\, d\mu_s \;=\; 0.95 \int_0^{\infty} \mathcal{P}(\mu_s;\, n, \mu_b)\, d\mu_s \qquad (32)$$

which reduces to the convention used by the Particle Data Group [50] for setting upper limits on Poisson processes with background. The maximum of this likelihood function with respect to variations in γ can be found analytically in terms of μ_s, and this expression for γ is then substituted in the expression for the likelihood and the solution of the integral equation (32) leads to the upper limit.

With this procedure, there will be statistical error dominance when there are few or no observed events, but systematic error dominance when there are many events. For example, the solution to Eq. (32) using this likelihood for no observed events and no background is $N_{\text{U.L}} = 3.3$ for $\delta = 0.18$, whereas $N_{\text{U.L.}} = 3.0$ when no systematic error is introduced. In this example there will be a 10% increase on the upper limit for the signal induced by a 18% systematic uncertainty, Figure 78.

To account for the mass dependence of μ_s and μ_b, the mass spectrum is divided into m bins. The bins are later reduced to zero width in the unbinned limit. The likelihood function corresponding to a signal with mass M_{F^*} can be expressed as the product of the likelihoods from each mass bin:

$$\mathcal{P}(M_{F^*}) \;=\; \prod_{i=0}^{m} \mathcal{P}(\mu_{s,i}(M_{F^*});\, n_i, \mu_{b,i}) \qquad (33)$$

where n_i is the number of events observed in bin i, and $\mu_{b,i}$ and $\mu_{s,i}(M_{F^*})$ are the average number of background and signal events respectively in bin i. To obtain the upper limit curve the procedure is repeated for different F^* masses.

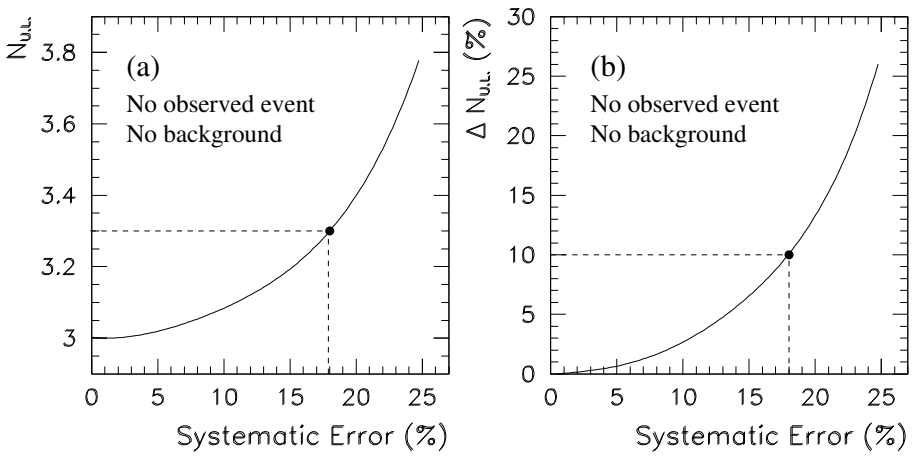

Figure 78: (a) The upper limit on the number of signal events, $N_{\mathrm{U.L.}}$, and (b) variation of the upper limit for the signal, $\Delta N_{\mathrm{U.L.}}$, as a function of systematic uncertainty with no observed events and no background.

Increasing the number of bins in such a way that each bin has either 0 or 1 event, leads to:

$$\mathcal{P}(M_{F^*}) = \int \frac{d\gamma}{\sqrt{2\pi}\delta} \exp\left[-\frac{(\gamma-1)^2}{2\delta^2}\right] \cdot \prod_{i=0}^{m} \exp[-\gamma\,(\mu_{s,i}(M_{F^*}) + \mu_{b,i})] \prod_{j \in \text{filled bins}} \gamma\,(\mu_{s,j}(M_{F^*}) + \mu_{b,j}) \qquad (34)$$

or

$$\mathcal{P}(M_{F^*}) = \int \frac{d\gamma}{\sqrt{2\pi}\delta} \exp\left[-\frac{(\gamma-1)^2}{2\delta^2}\right] \cdot \exp[-\gamma\,(\mu_s(M_{F^*}) + \mu_b)] \prod_{j \in \text{events}}^{n} \gamma\,(\mu_{s,j}(M_{F^*}) + \mu_{b,j}) \qquad (35)$$

where $\mu_s(M_{F^*}) = \sum_j \mu_{s,j}(M_{F^*})$ is the total number of signal events across the mass spectrum and $\mu_b = \sum_j \mu_{b,j}$ is the total number of background events. The signal and background populations in each bin are given by:

$$\mu_{s,j}(M_{F^*}) = \left.\frac{d\mu_s}{dM}\right|_{M=M_j} dM \qquad (36)$$

$$\mu_{b,j} \;=\; \left.\frac{d\mu_b}{dM}\right|_{M=M_j} dM\,, \tag{37}$$

where dM is the bin size and M_j is the mass corresponding to bin j. To determine the 95% confidence limit on the number of events, $N_{\rm U.L.}$, using Eq. (32), the bin size cancels on both sides of the equation, leading to an unbinned likelihood.

The differential background contribution $d\mu_b/dM$ is determined from a fit to the Monte Carlo background distribution. The differential signal contribution is assumed to have a Gaussian lineshape:

$$\frac{d\mu_s}{dM} \;=\; \mu_s(M_{F^*})\frac{\exp[-(M-M_{F^*})^2/2\sigma_M(M_{F^*})^2]}{\sqrt{2\pi}\sigma_M(M_{F^*})}\,, \tag{38}$$

where $\sigma_M(M_{F^*})$ is the experimental mass resolution of the excited lepton with mass M_{F^*}. To obtain the mass resolution, Monte Carlo data samples were generated for each of the excited electron and neutrino decay modes for several masses (Section 5.1).

$\sigma_M(M_{F^*})$ is obtained from a Gaussian fit to the Monte Carlo mass distribution, where the fit extends to $\pm 3\sigma$ from the peak and may cut a non-Gaussian tail. The narrow width approximation is used to derive the differential signal contribution. In other words, it is assumed that the intrinsic lineshape is very small (delta-function) and the dominant contribution to the lineshape is experimental resolution. To evaluate the likelihood of Eq. (34), a search window is defined in the invariant mass corresponding to $\pm 4\sigma_M$ of Gaussian resolution centered at the expected signal mass M_{F^*}.[25]

For the two gauge boson decay modes

$$e^* \to e\,Z \to e\,q\,\overline{q} \quad \text{and} \quad e^* \to e\,Z \to e\,\nu\,\overline{\nu},$$

[25]The variation of the mass window from $\pm 3\,\sigma_M$ to $\pm 5\,\sigma_M$ has no significant effect on the limits.

the likelihood for the excited electron decay is the product of the likelihoods from each decay chain separately:

$$\mathcal{P}(M_{e^*}) \;=\; \mathcal{P}_1(M_{e^*})\,\mathcal{P}_2(M_{e^*}) \;=\; \int \frac{d\gamma}{\sqrt{2\pi}\delta}\,\exp\left[-\frac{(\gamma-1)^2}{2\delta^2}\right] \tag{39}$$
$$.\exp[-\gamma\,(\mu_s(M_{e^*})+\mu_b^{(1)}+\mu_b^{(2)})]\prod_{i\in\text{events}}^{n_1}\gamma\,(\mu_{s,i}^{(1)}+\mu_{b,i}^{(1)})\prod_{j\in\text{events}}^{n_2}\gamma\,(\mu_{s,j}^{(2)}+\mu_{b,j}^{(2)})\,,$$

where $\mu_s(M_{e^*}) = \mu_s^{(1)} + \mu_s^{(2)}$ is the total signal contribution from the two decay modes of the excited electron with mass e^*. It should be noted that due to the fact that $e^* \to eZ$ is common to the two decay chains, there will be identical production cross-sections. Therefore, $\mu_s^{(1)}/\mu_s^{(2)} = \epsilon_1/\epsilon_2$, where ϵ_i is the efficiency of the ith decay mode. The likelihood then can be rewritten as:

$$\mathcal{P}(M_{e^*}) \;=\; \int \frac{d\gamma}{\sqrt{2\pi}\delta}\,\exp\left[-\frac{(\gamma-1)^2}{2\delta^2}\right] \tag{40}$$
$$.\exp[-\gamma\,(\mu_s(M_{e^*})+\mu_b^{(1)}+\mu_b^{(2)})]$$
$$\cdot\prod_{i\in\text{events}}^{n_1}\gamma\left[\Big(\frac{\epsilon_1}{\epsilon_1+\epsilon_2}\Big)\mu_{s,i}(M_{e^*})+\mu_{b,i}^{(1)}\right]\prod_{j\in\text{events}}^{n_2}\gamma\left[\Big(\frac{\epsilon_2}{\epsilon_1+\epsilon_2}\Big)\mu_{s,j}(M_{e^*})+\mu_{b,j}^{(2)}\right].$$

The upper limit on the signal cross-section in obtained by dividing $N_{\text{U.L.}}$ by the total efficiency $\epsilon_1 + \epsilon_2$, and the integrated luminosity.

Chapter 14

Results

By using 38.4 pb^{-1} of e^+p data at a center-of-mass energy of 300 GeV taken by the ZEUS detector at HERA in 1996 and 1997, a search for heavy excited electrons which decay into $e\gamma$, eZ, and νW has been performed. An analogous search has been made with the 1998/99 e^-p data at 318 GeV center-of-mass energy corresponding to an integrated luminosity of 16.7 pb^{-1} for heavy neutrino production in the $\nu\gamma$ decay channel. It should be noted that the excellence of the ZEUS detector in terms of efficiency as well as in reconstructing the mass of the excited electron and neutrino allows us to search for these heavy particles.

There has been agreement between the estimated background and the number of signal events remaining after our analysis in all the decay modes of our studies. Table 20 summarizes the results from this search and lists efficiency, mass resolution, number of observed events, and number of expected background events in each channel.

In the absence of an observed signal in any of the search channels, upper limits on the production cross-section times the branching ratio and limits on the characteristic coupling are derived. The limit-setting procedure is an unbinned likelihood method described in the previous chapter, which uses the mass distributions of the observed and the expected background events, the efficiency and mass resolution

for the signal, and the total luminosity. A systematic error of 18% (for e^*) and 14.4% (for ν^*) are included in the calculation as outlined in Chapter 12.

Table 20: Efficiency (ϵ), number of observed events ($N_{\rm Obs}$), and number of expected background events ($N_{\rm Exp}$) for the channels studied in this analysis.

Decay Channel	$N_{\rm Obs}$	$N_{\rm Exp}$	ϵ (%)	**Mass Resolution**
$e^* \to e\gamma$	49	63 ± 2	59.5 - 77.5	0.78 - 2.19 GeV
$e^* \to eZ \to eq\bar{q}$	29	26.5 ± 0.9	26.7 - 56.5	< 7 GeV
$e^* \to eZ \to e\nu\bar{\nu}$	1	3.3 ± 0.5	60.9 - 81.1	3.3 - 9 GeV
$e^* \to \nu W \to \nu q\bar{q'}$	11	10.6 ± 0.4	41.9 - 53.6	6 - 8 GeV
$\nu^* \to \nu\gamma$	2	1.8 ± 0.2	56.0 - 68.5	≈ 5 GeV

The resulting upper limit curves for the product of cross-section and branching ratio are shown in Figure 79. The previously published ZEUS limits [12] from 1994+95 data are shown in Figure 79 as well. A considerable improvement over the previously published results is evident.

For the excited electron decay channels $e^* \to e\,Z \to e\,q\,\overline{q}$ and $e^* \to e\,Z \to e\,\nu\,\overline{\nu}$, the upper limit is shown for each decay chain separately. Moreover, the upper limit is combined by multiplying the likelihood functions. The combined limit for $e^* \to eZ$ is presented in Figure 80.

The 95% confidence level upper limit on $\sigma \times BR$ for the final states with a photon is 0.11 pb at $M_e^* = 250$ GeV, which is approximately four times smaller than the previous ZEUS publication based on 9.4 pb^{-1} [12]. The double angle mass formula, Eq. (24), is a good way of measuring the $e^* \to e\,\gamma$ channel, because it helps in the improvement of the sensitivity at low mass where there are many events.

Despite the fact that the W decay of the excited electron dominates at higher masses [14, 15], the sensitivity to $e^* \to \nu W$ and $e^* \to eZ$ channels is weaker than that for $e^* \to e\gamma$ due to the lower efficiency, resolution, and higher number of candidate events. The 95% confidence level upper limits on $\sigma \times BR$ for the νW and eZ decay channels are 0.26 pb and 0.2 pb (combined limit for $eZ \to eq\bar{q},\ e\nu\bar{\nu}$) at $M_e^* = 250$ GeV, respectively.

Upper limits on the production cross-section times the branching ratio at 95% confidence level as a function of the ν^* mass for $\nu^* \to \nu\gamma$ are shown in Figure 81. The upper limit on $\sigma \times BR$ is 0.28 pb at $M_\nu^* = 250$ GeV. The limits from previous ZEUS publications [12, 13] are also shown.

The specific phenomenological model [14, 15] mentioned in Section 2.1 is used to calculate upper limits on the coupling. Assuming the relation between the two couplings of the model, f and f' for $SU(2)$ and $U(1)$ gauge fields, respectively, the branching ratios depend only on f/Λ where Λ is the compositeness scale. For the excited electron search the conventional relation $f = f'$ is assumed, whereas $f = -f'$ was adopted for excited neutrino search. Limits on f/Λ has been obtained from each of $e^* \to e\gamma$, eZ, and νW analyses respectively, and finally combining all the channels. We also set a limit on f/Λ for the $\nu^* \to \nu\gamma$ decay mode.

We calculate the upper limit on this quantity using the relation:

$$\left(\frac{f}{\Lambda}\right)_{\text{U.L.}} = \sqrt{\frac{(\sigma \cdot BR)_{\text{U.L.}}}{\sigma_{\text{MC}} \cdot BR}} \left(\frac{f}{\Lambda}\right)_{\text{MC}}, \tag{41}$$

where the Monte Carlo is used to calculate the theoretical cross-section, σ_{MC}, using the coupling $(f/\Lambda)_{\text{MC}}$.

Figure 82 presents the upper limit on f/Λ as a function of mass for excited electrons. Under the condition $f = f'$ the 95% confidence level upper limit on f/Λ for $e^* \to e\gamma$ varies from 5.8×10^{-4} GeV^{-1} to 1.25×10^{-2} GeV^{-1}, for e^* masses between 100 to 250 GeV.

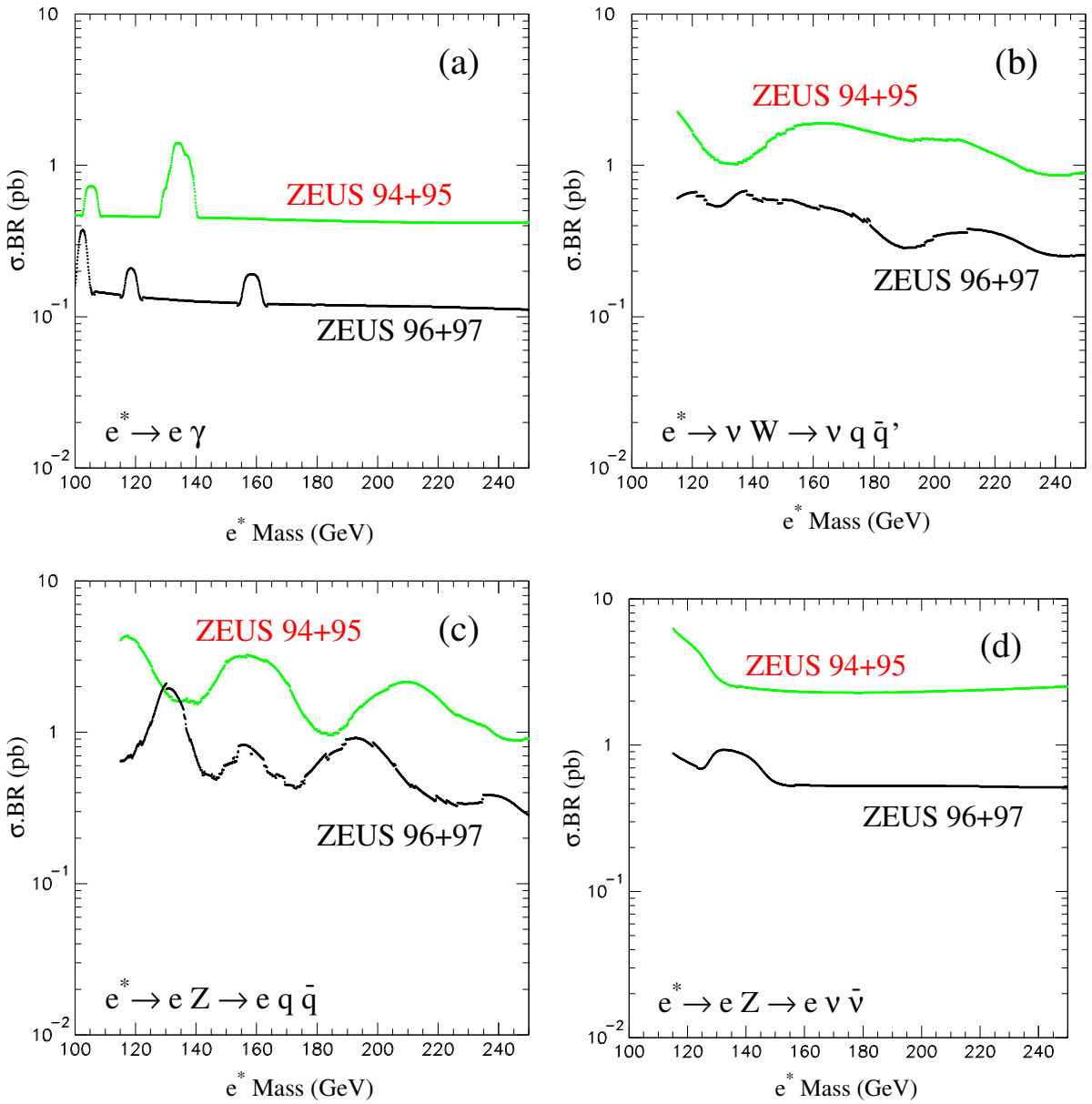

Figure 79: Upper limits on the production cross-section times the branching ratio at 95% confidence level as a function of e^* mass for: (a) $\sigma(ep \to e^*X) \times BR\,(e^* \to e\gamma)$, (b) $\sigma(ep \to e^*X) \times BR\,(e^* \to \nu W \to \nu q\bar{q}')$, (c) $\sigma(ep \to e^*X) \times BR\,(e^* \to eZ \to eq\bar{q})$, (d) $\sigma(ep \to e^*X) \times BR\,(e^* \to eZ \to e\nu\bar{\nu})$. The thick lines show the limits from the 96-97 ZEUS results. The thin lines and the dashed line represent the limits from previous ZEUS publication [12].

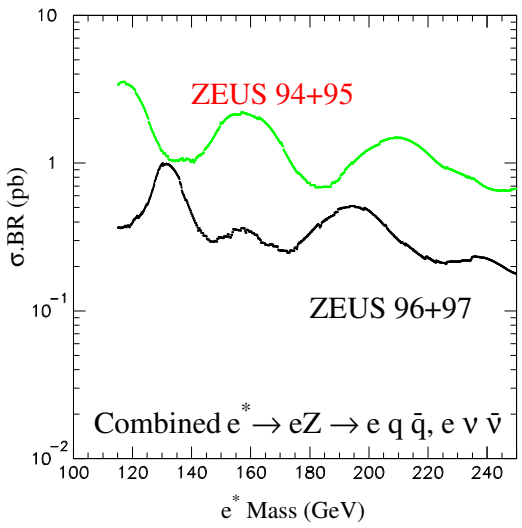

Figure 80: Upper limits on the combined production cross-section times the branching ratio at 95% confidence level as a function of e^* for $\sigma(e^+p \to e^*X) \times BR\,(e^* \to eZ \to eq\bar{q})$ and $\sigma(e^+p \to e^*X) \times BR\,(e^* \to eZ \to e\nu\bar{\nu})$.

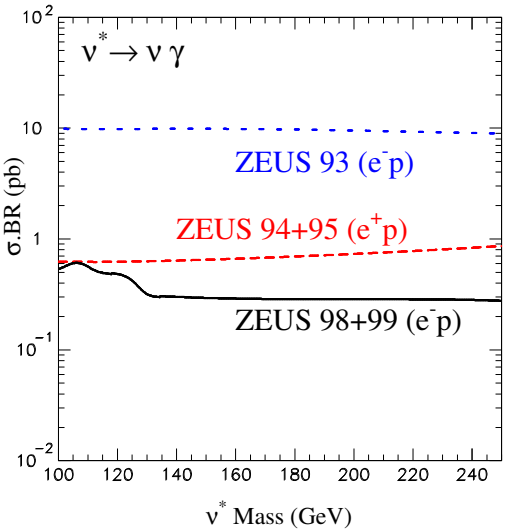

Figure 81: Upper limits on the production cross-section times the branching ratio at 95% confidence level as a function of ν^* mass for $\sigma(ep \to \nu^*X) \times BR\,(\nu^* \to \nu\gamma)$. The solid line shows the limits from the 98-99 ZEUS results. The dashed and dotted lines represent the limits from previous ZEUS publications [12, 13].

The 95% confidence level upper limits on f/Λ for $e^* \to \nu W$, $e^* \to eZ \to eq\bar{q}$ and $e^* \to eZ \to e\nu\bar{\nu}$ vary from 1.7 $\times$ 10^{-3} GeV^{-1} to 1.4 $\times$ 10^{-2} GeV^{-1}, from 6.7 $\times$ 10^{-3} GeV^{-1} to 3.5 $\times 10^{-2}$ GeV^{-1}, and from 7.7 $\times$ 10^{-3} GeV^{-1} to 4.8 $\times 10^{-2}$ GeV^{-1}, for e^* masses between 110 to 250 GeV, respectively.

The combined limit from $e^* \to eZ \to eq\bar{q}$ and $e^* \to eZ \to e\nu\bar{\nu}$ extends from 5.2 $\times$ 10^{-3} GeV^{-1} to 2.9 $\times$ 10^{-2} GeV^{-1} for an e^* mass interval of 110 to 250 GeV.

The combined upper limit for all channels at the 95% confidence level on f/Λ is 5.7 $\times$ 10^{-4} GeV^{-1} for M_{e^*} = 100 GeV and 9.5 $\times$ 10^{-3} GeV^{-1} for M_{e^*} = 250 GeV, which is approximately two times better than the previous ZEUS result [12].

By assuming that $f/\Lambda = 1/M_{e^*}$, one can extract single mass limits on excited electrons from the limit curves on f/Λ as a function of e^* mass. By using the combined limit from all three decay modes excited electrons can be ruled out in this model at the 95% confidence level in the mass interval 100 to 229 GeV. The upper mass limit is 222 GeV using only the limit from the $e^* \to e\,\gamma$ search.

For the $\nu\gamma$ channel, under the relation $f = -f'$, the 95% confidence level upper limit on f/Λ extends from 3.4×10^{-3} to 1.85×10^{-2} for M_{ν^*} between 100 and 220 GeV, and the assumption $f/\Lambda = 1/M_{\nu^*}$ rules out excited neutrinos in the mass range 100 to 161 GeV. This represents a considerable improvement over our previously published results [12], Figure 83.

It is notable to mention that the detector resolution is the dominant contribution to the lineshape for low mass excited electrons and neutrinos. However, at higher masses, there will be an increase of width along with the weakening of the coupling limit and the narrow width approximation is not valid any more. In other words, the highest mass reached by the limit curve in all cases corresponds to the point where the total decay width of the excited electron or neutrino, based on the upper limit for f/Λ, exceeds the experimental mass resolution. Also the candidate events contribute to the limit over a wider mass along with the widening of

the lineshape. However, this contribution is not significant. For these reasons the limits are calculated up to 250 GeV for excited electron and 220 GeV for excited neutrino.

14.1 Present Constraints

An analysis has been done for the excited fermion search by the H1 experiment based on their 94-97 e^+p data for an integrated luminosity of 38.4 pb^{-1} [51]. Their exclusion region for e^* masses between 60 and 230 GeV correspond to values of f/Λ above 0.6×10^{-3} to 6×10^{-3} GeV^{-1}. In the same way, the exclusion region of f/Λ is above values between 0.3×10^{-2} to 9×10^{-2} GeV^{-1} for a ν^* mass interval of 60 to 185 GeV.

Excited leptons can also be produced in e^+e^- collisions through

$$e^+e^- \rightarrow l^*l^*$$

or

$$e^+e^- \rightarrow l^*l$$

channels where $l = e, \nu, \mu$. Currently the most stringent limits on the masses and coupling of excited leptons comes from LEP2 experiments. Searches at L3 [52] with center-of-mass energy $\sqrt{s} = 189$ GeV ruled out any pair produced excited electron (neutrino), assuming $f = f'$ ($f = -f'$) at masses below 94.2 (94.1) GeV at the 95% confidence level.[26]

A recent search on single produced excited leptons analogous to the search at HERA, by DELPHI [53] in the center-of-mass range $\sqrt{s} = 192$ - 202 GeV excludes values of f/Λ above 1.8 $\times 10^{-4}$ GeV^{-1}, for an e^* mass equal to 120 GeV, and to

[26] Note that since the excited fermions are pair produced, these limits depend only on the gauge couplings of the excited fermion and thus are independent of the transition coupling parameter c_{VF^*F}.

5×10^{-4} GeV^{-1}, for an e^* mass equal to 200 GeV, assuming $f = f'$. Their limit for ν^* under the condition $f = -f'$ extends from 2×10^{-3} GeV^{-1} to 3.5×10^{-2} GeV^{-1} for a ν^* mass interval of 120 to 196 GeV.

The e^* limits derived from QED processes can go beyond the kinematic limit for excited fermion production in the direct mode where the decay products of the excited fermion are observed directly. One of the most commonly used methods is looking for deviations of the angular distribution from QED predictions (this effect depends on the excited electron mass and the $e^*e\gamma$ coupling) in the process

$$e^+e^- \rightarrow \gamma\gamma\,,$$

where a virtual e^* is exchanged in the t-channel [54]. Limits derived with this method are weaker and only exclude the region for f/Λ above 10^{-3} GeV^{-1}, but the mass range of the excited electron can be extended up to 400 GeV. The DELPHI experiment, for example, used this process and set an upper limit

$$f/\Lambda \leq 3 \times 10^{-3}\text{GeV}^{-1}$$

at 95% confidence level for excited electrons with masses above the LEP2 kinematic limit of 192 - 202 GeV [53]. Figures 82 and 83 show our limits on f/Λ as a function of the e^* and ν^* together with the best recent limits from DELPHI experiment.

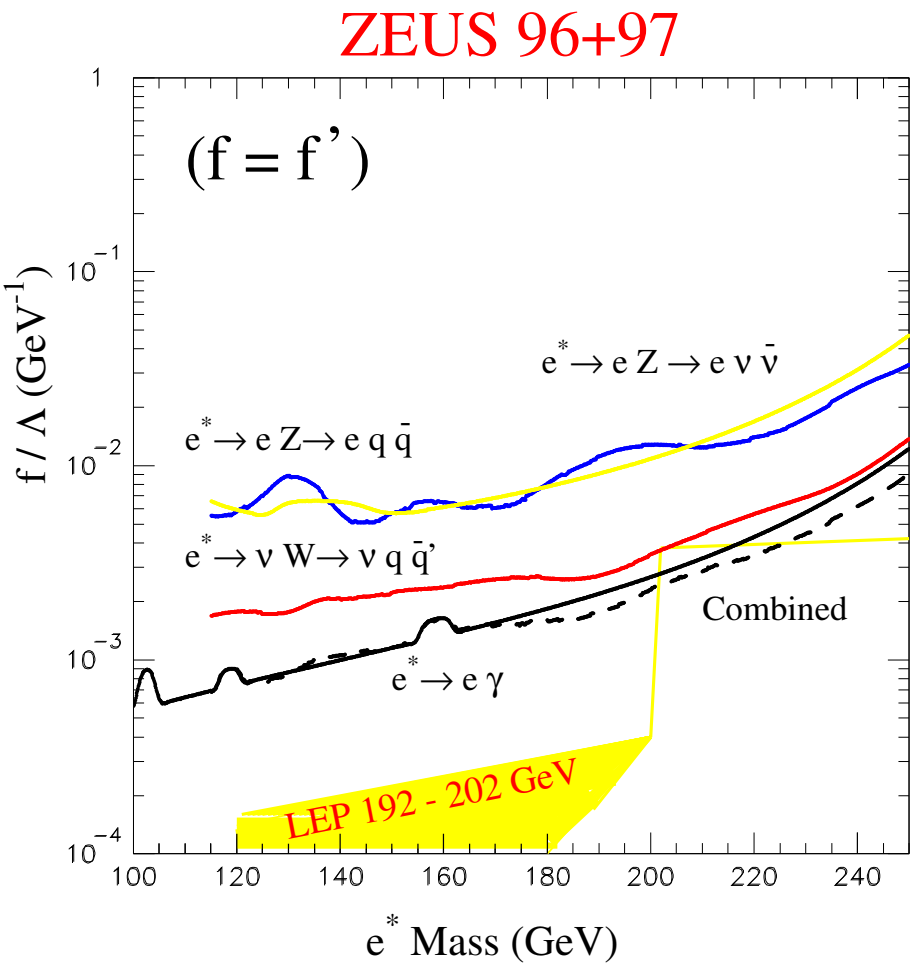

Figure 82: The upper limit at 95% confidence level on the coupling f/Λ as a function of the e^* mass assuming $f = f'$. Four solid lines are limits for $e^* \to e\,\gamma$, $e^* \to \nu\,W \to \nu\,q\,\bar{q}'$, $e^* \to e\,Z \to e\,q\,\bar{q}$, and $e^* \to e\,Z \to e\,\nu\,\bar{\nu}$ respectively, and the dashed curve represents the combined limit from four channels. The shaded line is the limit from the DELPHI experiment [53], where the limit variations are approximated by the line width. In all cases the areas above the lines are excluded.

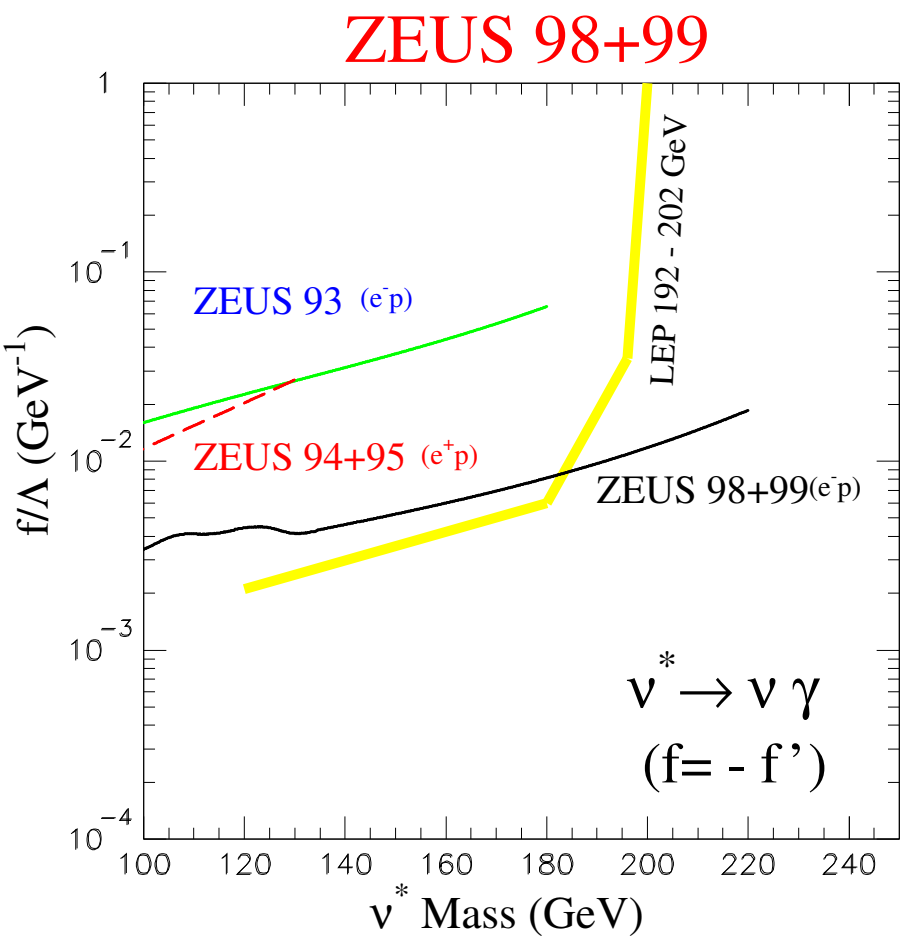

Figure 83: Upper limit at 95% confidence level on the coupling f/Λ as a function of the ν^* mass assuming $f = -f'$. Also limits from previous ZEUS results from e^-p data (thin curve) [13], and e^+p data (dashed curve) [12] are shown. The shaded line is the limit from the DELPHI experiment [53], where the limit variations are approximated by the line width. In all cases the areas above the lines are excluded.

Chapter 15

Conclusions

A search for heavy excited electrons which decay into $e\gamma$, eZ, νW has been performed using 38.4 pb^{-1} of e^+p data at a center-of-mass energy of 300 GeV taken by the ZEUS detector at HERA in 1996 and 1997. No evidence is observed for a resonance decaying to any of the considered final states, so upper limits for the production cross-sections times branching ratio for masses from 100 GeV to 250 GeV are derived.

Under the condition $f = f'$ the 95% confidence level upper limit on f/Λ varies from 5.7×10^{-4} to 9.5×10^{-3} for e^* masses between 100 to 250 GeV. Assuming $f/\Lambda = 1/M_{e^*}$, excited electrons between 100 GeV and 229 GeV are excluded at the 95% confidence level.

Also a search has been performed with 16.7 pb^{-1} of 1998/99 e^-p data at 318 GeV center-of-mass energy for excited neutrino production followed by $\nu\,\gamma$ decay. No evidence is found for such states and limits on the characteristic couplings are derived. For this channel, under the relation $f = -f'$, the 95% confidence level upper limit on f/Λ ranges from 3.4×10^{-3} to 1.85×10^{-2} for ν^* masses between 100 to 220 GeV. This represents a considerable improvement over our previously published results [12, 13]. Assuming $f/\Lambda = 1/M_{\nu^*}$, excited neutrinos between 100 GeV and 161 GeV are excluded at 95% confidence level.

Our good ability to set limits on the production of excited electrons and neutrinos at high masses is basically due to our high center-of-mass energy and our good efficiency for excited leptons heavier than the Z boson mass.

If there is no signal observed in future ZEUS data, the upper limit on the production cross-section as well as the coupling constants will scale down along with the increase of luminosity ($\mathcal{L}$). In the absence of any background the upper limit on the cross-section and f/Λ scale with $1/\mathcal{L}$ and $1/\sqrt{\mathcal{L}}$ respectively, but a major increase in the amount of the background along with the increase of luminosity[27] is expected which degrades the scale dependency of the limit to a smaller power of $\mathcal{L}$.

HERA will continue to be a good machine for searching for high mass excited electrons and neutrinos after the luminosity upgrade by a factor of 5 in 2001!

[27]The reaction rate R, is given by

$$R = \sigma \mathcal{L},$$

where σ is the interaction cross-section.

Appendix A

Definition of DST Bits

In the following we summarise the definition of the DST selection bits used in this analysis (Section 7.1.1). Any subscript denoted by "SLT" or "TLT" correspond to variables calculated at SLT or TLT stage.

Bit 33 (Neutral Current DIS):

It requires any of the following requirements:

- Event's pattern regoginzed by MUTRIG muon finder should not consistent with the cosmic muon and muon halo,
- High E_t NC events: a good TLT vertex and no CTD beam-gas and

$$\left(\begin{array}{c} E_t\,[-2\,\mathrm{ir}]\Big|_{\mathrm{SLT}} > 16\ \mathrm{GeV}\ .\mathrm{and.}\ E - P_z\Big|_{\mathrm{SLT}} > 34\ \mathrm{GeV} \\ .\mathrm{and.} \\ \text{up-down CAL timing} \end{array} \right)$$

  where $E_t\,[\,-2\,ir\,]$ is the total transverse energy in the calorimeter excluding the two first inner ring of the FCAL. A good TLT vertex is defined as a vertex measured by the CTD within 60 cm of the nominal collision point along the beam axis and a radial vertex

distribution less than 10 cm, and up-down CAL timing is the difference of the CAL time between the upper half and the lower half associated to the event which should be consistent with collisions from positron and proton.

- High E_t events with no backward energy:

$$\left(\begin{array}{c} E_t\,[-1\,\mathrm{ir}]\Big|_{\mathrm{TLT}} > 15\ \mathrm{GeV}\ \ .\mathrm{and.}\ \ E - P_z\,\Big|_{\mathrm{TLT}} > 32\ \mathrm{GeV} \\ .\mathrm{and.} \\ E\,[\theta > 150^o\,]\,\Big|_{\mathrm{TLT}} < 5\ \mathrm{GeV}\ \ .\mathrm{and.}\ \ \mathrm{up\text{-}down\ CAL\ timing} \\ .\mathrm{and.} \\ \left(\begin{array}{c} \#\ \mathrm{of\ TLT\ vertex\ tracks} > 0 \\ .\mathrm{or.} \\ \left.\frac{P_t\,[-1\,ir\,]^2}{E_t\,[-1\,\mathrm{ir}\,]}\right|_{\mathrm{TLT}} < 25\ \mathrm{GeV} \end{array} \right) \end{array} \right)$$

where $[\,-1\,ir\,]$ corresponds to excluding the first inner ring of the FCAL. A TLT vertex track is defined by a track with $P_t > 0.5$ GeV and DCA < 1.5 cm and $|ZCA| < 60$ cm. where $|ZCA|$ is the z of closest approach corresponding vertex. $E\,[\,\theta > 150^o\,]$ represents the total calorimeter energy deposited in the cone $\theta > 150^o$.

- High Q^2 NC events: No beam-gas vertex and

$$\left(\begin{array}{c} E - P_z\,\Big|_{\mathrm{TLT}} > 32\ \mathrm{GeV}\ .\mathrm{and.}\ E_e\,(\mathrm{electron})\,\Big|_{\mathrm{TLT}} > 10\ \mathrm{GeV} \\ .\mathrm{and.} \\ \max\,(\,Q^2_{\mathrm{da}},\,Q^2_{\mathrm{el}}\,) > 200\ \mathrm{GeV}^2 \end{array} \right)$$

and

$$\left(\begin{array}{c} \text{Not } x_e^2 + y_e^2 < 30^2\,, z_e < -120 \text{ cm} \\ \text{.and.} \\ \left(\quad \theta_e > 0.3 \text{ rad} \quad \text{.or.} \quad P_t(\text{electron}) > 2 \text{ GeV} \quad \right) \end{array} \right)$$

The beam-gas vertex is defined as a vertex with z < -80 cm and number of tracks $\geq$ 5 , $Q^2_{\rm el} = 2\,E^b_e\,E'_e\,(1+\cos\theta_e)$, and

$$Q^2_{\rm da} = (2E^b_e)^2 \frac{\sin\theta_e(1-\cos\theta_j)}{\sin\theta_j + \sin\theta_e - \sin(\theta_e+\theta_j)}$$

where θ_j is the polar angle of the jet.

During 1998/99 running period the last requirment on Q^2 was modified to $\max(\,Q^2_{\rm da},\,Q^2_{\rm el}\,) > 160$ GeV^2.

In addition the following conditions must be in fulfilled: it requires an electron (using either EM, Sira95, Eelec5, eExotic, or Local) and

$$\left(\quad E - P_z > 32 \text{ GeV} \quad \text{.and.} \quad E_t > 10 \text{ GeV} \quad \text{.and.} \quad E_e > 8 \text{ GeV} \quad \right)$$

Also the calorimeter timing associated to the event should be consistent with collisions from positron and proton. Two additional conditions

$$\left(\begin{array}{c} Q^2_{\rm da} > 160 \text{ GeV}^2 \quad \text{.or.} \quad Q^2_{\rm el} > 160 \text{ GeV}^2 \\ \text{.and.} \\ P_t \text{ (electron)} > 2 \text{ GeV} \end{array} \right)$$

were also added to definition of 1998/99 DST bits.

Bit 34 (Missing P_t):

It requires any of the following requirements:

- CC events:

$$\left(\begin{array}{c} \left| t_g\,(\mathrm{SLT}) \right| < 7 \text{ ns} \;\; .\mathrm{and.} \;\; \#\mathrm{PMT} > 1 \;\; .\mathrm{and.} \;\; \text{up-down CAL timing} \\ .\mathrm{and.} \\ P_t \,|_{\,\mathrm{SLT}} > 8 \text{ GeV} \;\; .\mathrm{and.} \;\; \text{not beam-gas vertex} \\ .\mathrm{and.} \\ \left(\; E_{\mathrm{FCAL}} \Big|_{\,\mathrm{TLT}} > 10 \text{ GeV} \;\; .\mathrm{or.} \;\; \mathrm{FLF}(49) \; \right) \\ .\mathrm{and.} \\ \left(\begin{array}{c} \text{Not too many beam-gas tracks} \\ .\mathrm{or.} \\ \text{two track \& good SLT vertex} \end{array} \right) \\ .\mathrm{and.} \\ \left(\; \#\text{ of CTD hits} < 2500 \;\; .\mathrm{or.} \;\; P_t\,[-1\,ir] \Big|_{\,\mathrm{SLT}} > 10 \text{ GeV} \; \right) \end{array} \right)$$

Too many beam-gas tracks means ≥ 5 beam-gas tracks and ≥ 25 tracks and two track & good vertex corresponds to a good vertex and two or greater number of vertex tracks. E_{FCAL} represents the total calorimeter energy deposited in the FCAL. FLF(49) is good FLT track.

In addition any of the following CC conditions at SLT level must be fulfilled:

$$\left(\; P_t > 6 \text{ GeV} \;\; .\mathrm{and.} \;\; E_t\,[-2\,ir] > 6 \text{ GeV} \;\; .\mathrm{and.} \;\; \mathrm{FLF}(49) \; \right)_{\mathrm{SLT}}$$

or

$$\left(\; P_t > 6 \text{ GeV} \;\; .\mathrm{and.} \;\; P_t\,[-1\,ir] > 8 \text{ GeV} \;\; .\mathrm{and.} \;\; E_{\mathrm{FCAL}} > 20 \text{ GeV} \; \right)_{\mathrm{SLT}}$$

or

$$\left(\; P_t \; > 9 \text{ GeV} \;\; \text{.and.} \;\; \frac{P_t}{\sqrt{E_t}} > 2.1 \text{ GeV}^{1/2} \;\; \text{.and.} \;\; E_{\text{FCAL}} > 80 \text{ GeV} \; \right)_{\text{SLT}}$$

In 1998/99 the first condition was modified as following

$$\left(\begin{array}{c} \left| t_g \, (\text{SLT}) \right| < 7 \text{ ns} \;\; \text{.and.} \;\; \#\text{PMT} > 1 \\ \text{.or.} \\ \#\text{ of SLT tracks} \geq 1 \;\; \text{.and. Not CTD beam-gas} \end{array} \right)$$

and the following additional conditions were added

$$\left(\begin{array}{c} P_t \; > \; 15 \, \text{GeV} \;\; \text{.or.} \;\; P_t \, [-1 \, ir \,] \; > \; 6 \text{ GeV} \\ \text{.or.} \\ P_t \; > \; 0.06 \, P_z \;\; \text{.or.} \;\; \left| P_y \,) \right| > \; 3 \, \text{GeV} \end{array} \right)_{\text{SLT}}$$

at SLT level and not

$$\left(\begin{array}{c} P_t \, [-1 \, ir \,] \; < \; 10 \, \text{GeV} \;\; \text{.and.} \;\; P_t \; < \; 25 \, \text{GeV} \;\; \text{.and.} \;\; P_t \; < \; 0.7 \, E_t \\ \text{.and.} \\ P_t \; < \; 0.8 \, P_z \;\; \text{.and.} \;\; E - P_z \; < 10 \, \text{GeV} \;\; \text{.and.} \;\; \left| P_y \right| \; < \; 4 \, \text{GeV} \end{array} \right)_{\text{TLT}}$$

were calculations are done at TLT level and the last three SLT-CC conditions were changed as following

$$\left(\begin{array}{c} \left(\; P_t \; > 6 \text{ GeV} \;\; \text{.and.} \;\; E_t \, [-2 \, ir \,] > 6 \text{ GeV} \; \right) \\ \text{.and.} \\ \left(\;\; \text{FLF(49)} \;\; \text{.or.} \;\; \#\text{ of SLT tracks} \geq 1 \;\; \right) \end{array} \right)_{\text{SLT}}$$

or

$$\left(P_t > 6\,\text{GeV} \text{ .and. } P_t[-1\,ir] > 8\,\text{GeV} \text{ .and. } E_{\text{FCAL}} > 20\,\text{GeV} \right)_{\text{SLT}}$$

or

$$\left(P_t > 9\,\text{GeV} \text{ .and. } P_t^2 > 2.31\,E_t\ \text{GeV} \text{ .and. } E_{\text{FCAL}} > 80\,\text{GeV} \right)_{\text{SLT}}$$

or

$$\left(E - P_z > 6\,\text{GeV} \text{ .and. } P_t^2 > 2.25\,E_t\ \text{GeV} \text{ .and. good track} \right)_{\text{SLT}}$$

- CC good track events:

$$\left(\begin{array}{c} \left(P_t > 6\ \text{GeV} \text{ .and. a good vertex} \right) \\ \text{.and.} \\ \text{up-down CAL timing} \end{array} \right)_{\text{TLT}}$$

  with a least a track with $P_t > 0.5$ GeV (0.2 GeV for 1998/99 definition) and DCA < 1.5 cm and $|ZCA| < 60$ cm.

- $P_t\,[-1\,ir]\,\big|_{\text{TLT}} > 7$ GeV (the threshold wasreduced to 6 GeV in 1998/99).

Additional condition $P_t > 7$ GeV was required in 1998/99.

Bit 36 (High E_t):

It requires any of the following requirements:

- High E_t events:

$$\left(\begin{array}{c} E_t\,[\,-2\,ir\,]\,\big|_{\rm SLT} > 35\ {\rm GeV} \\ {\rm .and.} \\ \left(\begin{array}{c} {\rm a\ good\ TLT} \\ {\rm .or.} \\ E_t\,[\,-2\,ir\,]\,\big|_{\rm TLT} > 50\ {\rm GeV} \end{array} \right) \\ {\rm .and.} \\ {\rm up\text{-}down\ CAL\ timing} \end{array} \right)$$

- $E_t\,[\,-1\,ir\,] > 35$ GeV
- $E_t\,[\,-1\,ir\,] > 30$ GeV .and. $E - P_z > 10$ GeV.

It also requires to have a vertex between -120 cm to 60 cm of the nominal collision point along the beam axis.

The 98/99 dfinition of this bit is modified as either the condition metioned before or $Et\,[\,-1\,ir\,] > 50$ GeV.

Bit 37 (Good Vertex):

It requires either a reconstructed offline or TLT vertex with

$$-60\ \ {\rm cm}\ \ <\ z_{vtx}\ <\ \ 120\ \ {\rm cm}\,,$$

where z_{vtx} is the vertex distribution along the beam axis.

Appendix B

Derivation of Mass Formulae

In this appendix, we describe in some detail the derivation of the invariant mass formulae presented in Chapters 9 and 11.

B.1 Derivation of Eq. (24)

Imagine the proton radiates a photon which interacts directly with electron and produce an excited electron which decays into a photon and an electron. Such a photon is emitted almost parallel to the initial proton direction and carries a fraction $\xi.E_p^b$ $(0 \leq \xi \leq 1)$ of the incoming proton's energy.[28]

Assuming that the proton remnant disappears in the forward beam hole[29] and neglecting the transverse momentum of the recoiling hadronic system, energy and momentum conservation reads

$$\xi.E_p^b + E_e^b = E_e + E_\gamma \,, \tag{42}$$

$$\xi.E_p^b - E_e^b = E_e \cos\theta_e + E_\gamma \cos\theta_\gamma \,, \tag{43}$$

$$0 = E_e \sin\theta_e + E_\gamma \sin\theta_\gamma \,. \tag{44}$$

[28] At high energies $E >> m$, so that $E \approx P$, where E, P, and m the energy, momentum and mass of the particle respectively.

[29] That means $E^{\text{remn.}} \approx P_z^{\text{remn.}}$ and $P_x^{\text{remn.}} = P_y^{\text{remn.}} = 0$ where $E^{\text{remn.}}$ is the energy and $(P_x^{\text{remn.}}, P_y^{\text{remn.}}, P_z^{\text{remn.}})$ is the momentum of the proton remnant.

where E_e, E_γ, θ_e, and θ_γ are the energies and polar angles of the final decayed electron and photon, respecticely.

Eqs. (42) and (43) leads to

$$2\,E_e^b = E_e\,(1-\cos\theta_e)\;+\;E_\gamma(1-\cos\theta_\gamma)\;. \tag{45}$$

From Eqs. (44) and (45) we can see

$$E_e \;=\; \frac{2\,E_e^b\,\sin\theta_e}{(1-\cos\theta_e)\;+\;E_\gamma(1-\cos\theta_\gamma)}\;, \tag{46}$$

$$E_\gamma \;=\; \frac{2\,E_e^b\,\sin\theta_\gamma}{(1-\cos\theta_e)\;+\;E_\gamma(1-\cos\theta_\gamma)}\;. \tag{47}$$

According to Eq. (23) the $e\gamma$ invariant mass, $M_{e\gamma}$ can be written as

$$M_{e\gamma}^2 \;=\; 2\,E_e\,E_\gamma\left[\,1\;+\;\cos(\theta_e\;+\;\cos\theta_\gamma\,)\right]. \tag{48}$$

Finally, combining Eqs. (46)-(48), one obtains the $e\gamma$ invariant mass Eq. (24).

B.2 Derivation of Eq. (25)

Consider the production and decay of an excited electron into an ordinary electron and a Z boson with four-momenta $p_e = (E_e, P_{e\,x}, P_{e\,y}, P_{e\,z})$ and $p_Z = (E_Z, P_{Z\,x}, P_{Z\,y}, P_{Z\,z})$ respectively. According to Eq. (23)

$$M_{eZ}^2 \;=\; (E_e+E_Z)^2-(P_{e\,x}+P_{Z\,x})^2-(P_{e\,y}+P_{Z\,y})^2-(P_{e\,z}+P_{Z\,z})^2\,. \tag{49}$$

Asssuming that the proton remnant disappears in the forward beam hole and neglecting the transverse momentum of the recoiling hadronic system,

$$P_t = \sqrt{(P_{e\,x}+P_{Z\,x})^2+(P_{e\,y}+P_{Z\,y})^2}\;\approx\;0\,.$$

or

$$(P_{e\,x}+P_{Z\,x})^2\;\approx\;(P_{e\,y}+P_{Z\,y})^2 \tag{50}$$

Conservation of energy and longitudinal momentum

$$\begin{aligned} E_e^b \, + \, E_p^b \;\; &= \;\; E_e \, + \, E_Z \, , \\ -E_e^b \, + \, E_p^b \;\; &= \;\; P_{e\,z} \, + \, P_{Z\,z} \, , \end{aligned}$$

leads to

$$2\, E_e^b \;=\; (E_e + E_Z) - (P_{e\,z} + P_{Z\,z}). \tag{51}$$

Eq. (49) can be written as

$$M_{eZ}^2 \;=\; \Big[\, (E_e + E_Z) - (P_{e\,z} + P_{Z\,z}) \Big] \, . \, \Big[\, (E_e + E_Z) + (P_{e\,z} + P_{Z\,z}) \Big] \, ,$$

or

$$M_{eZ}^2 \;=\; 2\, E_e^b \, (E_e + P_{e\,z} + E_Z + P_{Z\,z}) \, . \tag{52}$$

From Z mass constraint $M_Z^2 = E_Z^2 - P_{Z\,x}^2 - P_{Z\,y}^2 - P_{Z\,z}^2$ and Eqs. (50) and (51) we can see

$$E_Z + P_{Z\,z} \;=\; \frac{(P_{e\,x}^2 + P_{e\,y}^2) + M_Z^2}{2\, E_e^b \, - \, (\, E_e - P_{e\,z}\,)} \, . \tag{53}$$

Eqs. (52) and (53) yield

$$M_{eZ}^2 \;=\; 2\, E_e^b \, \frac{2\, E_e^b \, (P_{e\,x}^2 + P_{e\,y}^2) + M_Z^2}{2\, E_e^b \, - \, (\, E_e - P_{e\,z}\,)} \, . \tag{54}$$

By means of the approximation $P_{e\,z} \;\approx\; E_e \, \cos\theta_e$, Eq. (54) reduces to Eq. (25).

B.3 Derivation of Eq. (26)

Now consider the production and decay of an excited electron into an ordinary neutrino and a W boson with four-momenta $p_\nu = (E_\nu, P_{\nu\,x}, P_{\nu\,y}, P_{\nu\,z})$ and $p_W = (E_W, P_{W\,x}, P_{W\,y}, P_{W\,z})$. According to Eq. (23)

$$M_{\nu W}^2 \;=\; (E_\nu + E_W)^2 - (P_{\nu\,x} + P_{W\,x})^2 - (P_{\nu\,y} + P_{W\,y})^2 - (P_{\nu\,z} + P_{W\,z})^2 \, . \tag{55}$$

Analogously to Eqs. (52) and (53)

$$M^2_{\nu W} \;=\; 2\,E^b_e\,(E_\nu + P_{\nu\,z} + E_W + P_{W\,z})\,. \tag{56}$$

and

$$E_W + P_{W\,z} \;=\; \frac{(P^2_{\nu\,x} + P^2_{\nu\,y})}{2\,E^b_e \;-\; (\,E_W - P_{W\,z}\,)}\,. \tag{57}$$

Eq. (56) can be written as

$$M^2_{\nu W} \;=\; 2\,E^b_e\,\frac{2\,E^b_e\,(E_W + P_{W\,z}) - M^2_W}{2\,E^b_e \;-\; (\,E_W - P_{W\,z}\,)}\,. \tag{58}$$

Here, only the W is visible and given $\delta \;=\; E_W - P_{W\,z}$. then, Eq. (58) reduces to

$$M^2_{\nu W} = \frac{4\,P^2_t\,(E^b_e)^2 \;+\; 2\,E^b_e\,M^2_W\,(2\,E^b_e \;-\; \delta)}{\delta\,(2\,E^b_e \;-\; \delta)}\,.$$

B.4 Derivation of Eq. (28)

Consider the production and decay of an excited neutrino into an ordinary neutrino and a photon with four-momenta $p_\nu \;=\; (E_\nu, P_{\nu\,x}, P_{\nu\,y}, P_{\nu\,z}\,)$ and $p_\gamma \;=\; (E_\gamma, P_{\gamma\,x}, P_{\gamma\,y}, P_{\gamma\,z}\,)$ respectively. According to Eq. (23)

$$M^2_{\nu\gamma} = (E_\nu + E_\gamma)^2 - (P_{\nu\,x} + P_{\gamma\,x})^2 - (P_{\nu\,y} + P_{\gamma\,y})^2 - (P_{\nu\,z} + P_{\gamma\,z})^2$$

Asssuming that the proton remnant disappears in the forward beam hole and neglecting the transverse momentum of the recoiling hadronic system $P_t \approx 0$,

$$P_{\nu\,x} \;=\; -\,(P_{\gamma\,x} + P_{\mathrm{had}\,x})\,, \tag{59}$$

$$P_{\nu\,y} \;=\; -\,(P_{\gamma\,y} + P_{\mathrm{had}\,y})\,, \tag{60}$$

with

$$P^{miss}_t = P^2_{\nu\,x} + P^2_{\nu\,y} = (P_{\gamma\,x} + P_{\mathrm{had}\,x})^2 + (P_{\gamma\,y} + P_{\mathrm{had}\,y})^2\,. \tag{61}$$

From conservation of energy and longitudinal momentum

$$\begin{aligned} E_e^b \,+\, E_p^b \;&=\; E_\nu \,+\, E_\gamma \,+\, E_{\rm had}\,, \\ -E_e^b \,+\, E_p^b \;&=\; P_{\nu\,z} \,+\, P_{\gamma\,z} \,+\, P_{{\rm had}\,z}\,, \end{aligned}$$

one obtains

$$2\,E_e^b \;=\; (E_\nu + E_\gamma + E_{\rm had}) - (P_{\nu\,z} + P_{\gamma\,z} + P_{{\rm had}\,z})\,, \tag{62}$$

where $p_{\rm had} = (\,E_{\rm had}, P_{{\rm had}\,x}, P_{{\rm had}\,y}, P_{{\rm had}\,z}\,)$ is the four-momentum of the final hadronic system.

ν mass constraint $M_\nu^2 = E_\nu^2 - P_{\nu\,x}^2 - P_{\nu\,y}^2 - P_{\nu\,z}^2 = 0$ can be written as

$$(E_\nu + P_{\nu\,z})\,.\,(E_\nu - P_{\nu\,z}) = P_{\nu\,x}^2 + P_{\nu\,y}^2 = P_t^{miss} \tag{63}$$

From Eqs. (63) and (64) one can derive

$$\begin{aligned} E_\nu = \frac{1}{2}\Bigg[\; & \frac{P_t^{miss}}{2\,E_e^b - (E_\gamma - P_{\gamma\,z} + E_{\rm had} - P_{{\rm had}\,z})} \\ & +2\,E_e^b - (E_\gamma - P_{\gamma\,z} + E_{\rm had} - P_{{\rm had}\,z})\Bigg]\,, \\ P_{z\nu} = \frac{1}{2}\Bigg[\; & \frac{P_t^{miss}}{2\,E_e^b - (E_\gamma - P_{\gamma\,z} + E_{\rm had} - P_{{\rm had}\,z})} \\ & -2\,E_e^b + (E_\gamma - P_{\gamma\,z} + E_{\rm had} - P_{{\rm had}\,z})\Bigg]\,. \end{aligned}$$

References

[1] S. L. Glashow, Nucl. Phys. **22** (1961) 579; S. Weinberg, Phys. Rev. Lett. **19** (1967) 1264; A. Salam, Elementary Particle Theory, eds. N. Svartholm, Stockholm, Almquist and Wiksell (1968) 367.

[2] R. B. Blumenthal, D. C. Ehn, W. L. Faissler, P. M. Joseph, L. J. Lanzerotti, F. M. Pipkin and D. G. Stairs, Phys. Rev. Lett. **14** (1965) 660.

[3] F. E. Low, Phys. Rev. Lett. **14** (1965) 238.

[4] E. R. Cohen and B. N. Taylor, Rev. Mod. Phys. **59** (1987) 1121.

[5] J. Brüger, Proceedings of the 1981 International Symposium on Lepton and Photon Interactions at High Energies, eds. W. Pfeil, Bonn (1981) 880.

[6] R. Hollebbek, Proceedings of the 1981 International Symposium on Lepton and Photon Interactions at High Energies, eds. W. Pfeil, Bonn (1981) 1.

[7] J. C. Pati, Phys. Lett. **B98** (1981) 40; J. C. Pati, A. Salam, and J. Strathdee, Nucl. Phys. **B185** (1981) 416; J. C. Pati, A. Salam, Phys. Rev. **D10** (1974) 275; J. C. Pati, A. Salam, and J. Strathdee, Phys. Lett. **B59** (1975) 265; K. Matumoto, Prog. Theor. Phys. **65** (1981) 390; **64** (1980) 1490; **52** (1974) 1973; O. W. Greenberg and J. Sucher, Phys. Lett. **B99** (1981) 339; Y. Ne'eman, Phys. Lett. **B82** (1979) 69; H. Fritzsch and G. Mandelbaum, Phys. Lett. **B102** (1981) 319; V. Visnjic-Triantafillou, Phys. Lett. **B95** (1980) 47; M. Veltman, Proceedings of the 1979 International Symposium on Lepton and Photon Interactions at High Energies, eds. by T. B. Kirk and H. D. I. Abarbarel, Fermilab (1979) 529; E. Derman, Phys. Lett. **B95** (1980) 169; Phys. Rev. **D23** (1981) 1623; H. Terazawa, Y. Chikashige, and K. Akama, Phys. Rev.

D15 (1977) 480; J. C. Taylor, Phys. Lett. **B88** (1979) 291; A. A. Ansel'm, JETP Lett. **31** (1980) 138.

[8] F. Mansouri, Phys. Lett. **B100** (1981) 25; M. Yasue, Phys. Lett. **B91** (1980) 85; Prog. Theor. Phys. **65** (1981) 1995; R. Casalbuon and R. Gatto, Phys. Lett. **B88** (1979) 306; B**90** (1980) 81.

[9] H. Harari, Phys. Lett. **B86** (1979) 83; M. A. Shupe, Phys. Lett. **B86** (1979) 87; E. J. Squires, Phys. Lett. **B94** (1980) 54; R. Ratio, Physica Scripta **22** (1980) 197; C. A. Nelson, Phys. Lett. **B93** (1980) 143; H. Harari and N. Seiberg, Phys. Lett. **B98** (1981) 269; **B100** (1981) 41; **B102** (1981) 263.

[10] E. J. Eichten, K. D. Lane, and M. E. Peskin, Phys. Rev. Lett. **50**, 811 (1983); M. E. Peskin, Proceedings of the 1981 International Symposium on Lepton and Photon Interactions at High Energies, eds. W. Pfeil, Bonn (1981) 880.

[11] F. M. Renard, Phys. Lett. **B126** (1983) 59; F. M. Renard, Phys. Lett. **B139** (1984) 449; N. Cabibbo, L. Maiani, Y. Srivastava, Phys. Lett. **B139** (1984) 459; A. De Rüjula, L. Maiani, R. Petronzio, Phys. Lett. **B140** (1984) 253; J. Kühn, H. D. Tholl and P. Zerwas, Phys. Lett. **B158** (1985) 270.

[12] ZEUS Collaboration, J. Breitweg *et. a.*, Z. Phys. **C76** (1997) 631; D. Acosta *et. a.*, A Search for Excited Fermions in e^+p Collisions, ZEUS-Note 96-110 (1996).

[13] ZEUS Collaboration, M. Derrick *et. al.*, Z. Phys. **C65** (1995) 627; S. Durkin *et al.*, A Search for Excited Fermions in Electron-Proton Collisions, ZEUS-Note 94-058 (1994).

[14] K. Hagiwara, S. Komamiya and D. Zeppenfeld, Z. Phys. **C29** (1985) 115.

[15] F. Boudjema, A. Djouadi, Phys. Lett. **B240** (1990) 485.

[16] U. Baur, M. Spira, and P. M. Zerwaz, Phys. Rev. **D42** (1990) 815.

[17] M. S. Chanowitz and S. D. Drell, Phys. Rev. Lett. **30** (1973) 807; S. J. Brodsky and S. D. Drell, Phys. Rev. **D22** (1980) 236.

[18] U. Bauer, J. A. M. Vermaseren, and D. Zeppenfeld, Nucl. Phys. **B375** (1992) 3.

[19] The ZEUS Detector, Status Report 1993, DESY 1993.

[20] M. Derrick *et al.*, Nucl. Inst. Methods **A309** (1991) 77; A. Andresen *et al.*, Nucl. Inst. Methods **A309** (1991) 110; A. Caldwell *et al.*, Nucl. Instrum. Methods **A321** (1992) 356; A. Bernstein *et al.*, Nucl. Inst. Methods **A336** (1994) 254.

[21] N. Harnew *et al.*, Nucl. Instrum. Methods **A279** (1989) 290; B. Foster *et al.*, Nucl. Phys. **B (Proc. Suppl.) 32** (1993) 181; B. Foster *et al.*, Nucl. Instrum. Methods **A338** (1994) 254.

[22] H. Brückmann *et al.*, Nucl. Instrum. Methods **A263** (1988) 136; R. Wigmans, Nucl. Instrum. Methods **A259** (1987) 389; M. G. Catanesi *et al.*, Nucl. Instrum. Methods **A260** (1987) 43; G. d'Agostini *et al.*, Nucl. Instrum. Methods **A274** (1989) 134; G. Drews *et al.*, Nucl. Instrum. Methods **A290** (1990) 335; U. Behrens *et al.*, Nucl. Instrum. Methods **A289** (1990) 115.

[23] J. Andruszkow *et al.*, DESY 92-066 (1992); ZEUS Collaboration, M. Derrick *et al.*, Z. Phys. **C63** (1994) 391.

[24] H. Bethe and W. Heitler, Proc, Roy. Soc. **A146** (1934) 83.

[25] W. Smith *et al.*, The ZEUS Trigger System, ZEUS 89-084.

[26] HEXF: H. J. Kim and S. Kartik, LSU Preprint LSUHE-145-1993.

[27] F. W. Brasse *et al.*, Nucl. Phys. **B39** (1972) 421.

[28] H. Plothow-Besch, CERN program library pool (W999), W5051 PDFLIB, version 7.08, 1997.

[29] Ch. Berger and W. Wagner, Phys. Rep. **146** (1987) 1.

[30] G. Ingelman, A. Edin and J. Rathsman, Comp. Phys. Commun. **101** (1997) 15.

[31] T. Sjöstrand, Comp. Phys. Commun. **39** (1986) 347; T. Söstrand and Bengtsson, Comp. Phys. Comm. **43** (1987) 367; T. Söstrand, Comp. Phys. Commun. **82** (1994) 74.

[32] K. Charchula, G. A. Schuler and H. Spiesberger, Comp. Phys. Commun. **81** (1994) 381; H. Spiesberger, DJANGO6 version 2.4 - A Monte Carlo Generator for Deep Inelastic Lepton Proton Scattering Including QED and QCD Radiative Effects, 1996, available on `WWW`: `http://www.desy.de/ hspiesb/django6.html`.

[33] L. Lonnblad, Comp. Phys. Comm. **71** (1992) 15.

[34] T. Carli *et al.*, Proceedings of the Workshop on Physics at HERA, Vol. 3, DESY (1991) 1468.

[35] G. Marchesini *et al.*, Comp. Phys. Comm. **67** (1992) 465.

[36] R. Brun *et al.*, GEANT 3.13, CERN DD/EE/84-1 (1987).

[37] G. Hartner and Y. Iga, Trigger Monte Carlo Program Status, ZEUS-Note 90-084 (1990).

[38] Andersen *et al.*, Nucl. Inst. Methods **A309** (1991) 101.

[39] G. F. Hartner, VCTRAK Briefing: Program and Math, ZEUS-Note 98-058 (1998).

[40] G. Briskin, Ph.D. thesis, Tel Aviv University, 1998.

[41] B. Straub and H. Zhang,
http://www-zeus.desy.de/~quadt/ZEUS_ONLY/em/em.html.

[42] A. López-Durán Viani and S. Schlenstedt, Electron finder efficiencies and impurities: A comparison between SINISTRA95, EM and EMNET , ZEUS-Note 99-077 (1999).

[43] ZEUS Collaboration, J. Breitweg *et al.* Euro. Phys. J. **C3** (1999) 427; Joanna Edmonds, Jörn Grosse-Knetter, and Arnulf Quadt, Neutral Current Cross Sections at High Q^2, ZEUS-Note 99-016 (1999).

[44] A. Caldwell, W. Liu, B. Mellado, and B. Straub, BCAL Electron Studies- Part I: MC and Test Beam Energy Studies, ZEUS-Note 98-002 (1998); A. Caldwell, W. Liu, and B. Straub, Electron Studies- Part II: Energy Scale Calibration, ZEUS-Note 98-018 (1998); H. J. Grabosch, A. Meyer, and S. Schlenstedt, X_0 Determination and Electron Energy Correction with the Presampler, ZEUS-Note 98-045 (1998).

[45] C. Catterall and F. Pelucchi, Comparison of CTD and Calorimeter Measurement of the DIS Positron Angle in High Q^2 Events, ZEUS-Note 97-056 (1997).

[46] N. Tuning, ZEUS Collaboration Meeting, 23^{rd} June 1998.

[47] J. Grosse-Knetter, Corrections for the Hadronic Final State, ZEUS-Note 98-031 (1998).

[48] A. Savin, Study of Calorimeter Noise in the 1996 data, ZEUS-Note 98-007 (1998).

[49] ZEUS Collaboration, J. Breitweg *et al.* Euro. Phys. J. **C3** (2000) 411.

[50] Particle Data Group, C. Caso, *et al.* Euro. Phys. J. **C3** (1998) 176.

[51] H1 Collaboration, Contributed paper **581** to ICHEP98, Vancouver, 23-29 July 1998.

[52] L3 Collaboration, Contributed paper **247** to EPS99, Tampere, 15-21 July 1999.

[53] DELPHI Collaboration, Contributed paper **354** to Moriond EW 2000, DELPHI 2000-35 CONF 354.

[54] M. Bardadin-Otwinowska, Z. Phys. **C55** (1992) 163; ALEPH Collaboration, D. Decamp *et al.*, Phys. Rep. **216** (1992) 253.